Numerical Modelling of Advanced Modulation Formats and WDM Transmission

RANJEET SINGH BHAMBER

Doctor of Philosophy

ASTON UNIVERSITY

November 2006

ASTON UNIVERSITY

Numerical Modelling of Advanced Modulation Formats and WDM Transmission

RANJEET SINGH BHAMBER

Doctor of Philosophy, 2006

Thesis Summary

This thesis presents a theoretical investigation of the application of advanced modelling formats in high-speed fibre lightwave systems.

The first part of this work focuses on numerical optimisation of dense wavelength division multiplexing (DWDM) system design. We employ advanced spectral domain filtering techniques and carrier pulse reshaping. We then apply these optimisation methods to investigate spectral and temporal domain characteristics of advanced modulation formats in fibre optic telecommunication systems.

Next we investigate numerical methods used in detecting and measuring the system performance of advanced modulation formats. We then numerically study the combination of return-to-zero differential phase-shift keying (RZ-DPSK) with advanced photonic devices.

Finally we analyse the dispersion management of Nx40 Gbit/s RZ-DPSK transmission applied to a commercial terrestrial lightwave system.

Keywords: Nonlinear Optics, Optical Communications Systems, Modulation Formats, RZ-OOK, CS-RZ, RZ-DPSK, Nonlinear Loop Mirror, Semi-conductor Optical Amplifiers.

To my parents and brother.

Acknowledgements

I would like to deeply thank various people who, during the period of my research provided me with useful and helpful assistance. Without their care and consideration, this investigation would likely not have matured within the rapid field of fibre optics communications.

First and foremost I would like to give my greatest humble gratitude to Professor Sergei K. Turitsyn for his inspirational mentoring, guidance, assistance and his wealth of knowledge, which helped guide my research in the forward and upward direction. For without his mastery in the cognition of theoretical physics with applied photonics, the production of this research would have been belated. This has been an amazing journey, but without his mentoring it would be deemed as a far gone near impossible conclusion.

Both the combination of numerical analysis and software engineering pushed the forefront of this cutting edge and innovation field. I would like to express my deepest appreciation to Dr. Vladimir Mezentsev, for his vast knowledge in this sector. His amazing transferable skills and his in depth understanding within modelling optics, I would always have the utmost respect for and will always be profoundly indebted to him.

I would like to express my greatest thanks to Dr. S. Boscolo, who I greatly enjoyed working with. I have come to respect and admire her broad comprehention of the field of mathematics and photonics.

I wish to express my sincere thanks to Mrs Elena G. Turitsyna, Dr. Wladek Forysiak and Dr. Jeroen H. B. Nijhof for co-authoring journal publication and their undivided assistance and attention.

I would like to thank my closest colleague and friend for the majority of research period at Aston, Dr. Cristos Braimiotis. His expertise in rational thinking and thought in contemplating, deducing and hypothesizing on any highly debated topic of current interest has been an inspiration to me. I will always remember our enthralling discussions regarding our ongoing research.

I would like to appreciate the network manager, systems administrator and close friend Mr. Supun Athukorale for his understanding contribution and exceptional abilities in provid-

ing a stable, secure and efficient computer environment to work under.

I would like to express my gratitude to Dr Shoichiro Oda from the department of Electronic, Information Systems and Engery Engineering, Graduate school of Engineering, Osaka University, Japan. His short but vital stay at the Photonics Research Group was a vital insider to the ongoing research in Japan. He is an inspirational to work with.

I would like to finalise my acknowledgements and appreciation to the members of the Photonics Research Group, Aston. In particular appreciation I would like to highlight Dr Juan D. Ania-Castan and Dr Stanislav Derevyanko who are members of the theoretical sector of the group. They helpfully contributed by discussing the finer technical aspects of the research.

Most importantly I would like to thank my father, Harbinder Singh Bhamber, mother, Joginder Kaur Bhamber and primarily my brother, Pritpal Singh Bhamber, to whom I own all my success to.

Contents

List of Figures

List of Tables

List of Acronyms

ASE..... Amplified Spontaneous Emission

ASK..... Amplitude Shift Keying

BER..... Bit Error Rate

CDR ..... Clock and Data Recovery

CS-RZ ..... Carrier-Suppressed Return-to-Zero

CS-RZ-DPSK . Carrier-Suppressed Return-to-Zero Differential Phase Shift Keying

CW..... Continuous Wave

DCF..... Dispersion Compensating Fiber

DCM..... Dispersion Compensation Module

DEMUX..... Demultiplexer

DML..... Directly Modulated Laser

DPSK..... Differential Phase Shift Keying

DSA..... Dual Stage Amplifier

DWDM..... Dense Wavelength Division Multiplexing

EDFA ..... Erbium Doped Fiber Amplifier

EE-SMF..... Enlarged Effective Area Single Mode Fibre

FEC..... Forward Error Correction

FFT ..... Finite-Fourier-Transform

FFTW ..... Fastest Fourier Transform in the West

FSK..... Frequency Shift Keying

FWHM..... Full Width at Half Maximum

GNLSE..... Generalised Nonlinear Schrödinger Equation

GVD ..... Group Velocity Dispersion

IFWM ..... Intrachannel Four-Wave Mixing

LSB ..... Lower Sideband

MUX ..... Multiplexer

MZDI ..... Mach-Zehnder Delay Interferometer

MZM ..... Mach-Zehnder Modulator

NLSE ..... Nonlinear Schrödinger Equation

NOLM ..... Nonlinear Optical Loop Mirror

NRZ ..... Non-Return-To-Zero

NRZ-OOK .... Non-Return-To-Zero On-Off Keying

OBPF ..... Optical Band Pass Filter

OOK ..... On-Off Keying

OSNR ..... Optical Signal-To-Noise Ratio

PCF ..... Photonic Crystal Fiber

PDE ..... Partial Differential Equation

PDM ..... Polarisation Division Multiplex

POL-SK ..... Polarisation Shift Keying

PSK ..... Phase Shift Keying

RA ..... Raman Amplifier

RA-NOLM .... Raman Amplifier Nonlinear Optical Loop Mirror

RMS ..... Root-Mean-Square

RTL ..... Reverse Teralight Fibre

RZ ..... Return-To-Zero

RZ-DPSK ..... Return-To-Zero Differential Phase Shift Keying

RZ-OOK ..... Return-To-Zero On-Off Keying

SCDCF ..... Slope Compensating Dispersion Compensation Fiber

SG ..... Super Gaussian

SMF ..... Single Mode Fiber

SOA..... Semiconductor Optical Amplifier

SPM..... Self-Phase Modulation

SSA..... Single Stage Amplifier

SSB..... Single Side Band

TL..... Teralight Fibre

USB..... Upper Sideband

VSB..... Vestigial Side Band

WDM..... Wavelength Division Multiplexing

XPM..... Cross-Phase Modulation

Chapter 1

Introduction

1.1 Historical Perspective

The demand for higher bit rates and lower system costs are driven by society's ever increasing reliance on high bandwidth application/services, such as high-speed internet access, mobile voice and data services, multimedia broadcasting system and high capacity data stores for grid computing and remote storage. This has lead to a greater demand for more higher spectral efficient telecommunication links. A cost efficient way to meet the need of higher data rates, is to upgrade exciting links form 10 Gbit/s to a higher capacity, 40Gbit/s. A number of key enabling technologies have emerged in order to facilitate this need. They are ultra-narrow optical filtering, wavelength division multiplexing (WDM), dense wavelength division multiplexing (DWDM) and advance modulation formats which have emerged as a spectral efficient way of enabling higher system performance.

In the early development of fibre optics, the greatest limiting factor prohibiting the use of optical fibre in telecommunication applications, was the extremely high losses (greater than 1000 dB/km) associated with these early fibres. This was overcome in the 1970s when the optical loss of silica fibre was reduced to below 20 dB/km [1]. By the end of the 1970 a significant amount of work had been done to to reduce this value down to 0.2 dB/km at $\lambda = 1.55\mu$m [2].

The 1980s saw the advent of optical solitions [3]. They were first proposed by Hasegawa

and Tappert [4]. They proposed to use the Kerr nonlinearity in compensating for fibre dispersion. The result was optical solitons which fueled new areas of research [5–10].

The next significant break through occurred in the 1990s with the development of optical fibre amplifiers and lasers. They were created by doping the optical fibre with rare-earth elements [11]. Erbium-doped fibre amplifiers (EDFAs) were quickly adopted as it operated near the $\lambda = 1.55\mu$m region. This lead to a revolution of fibre optic capacities and transmission distances [12, 13].

More recent developments have seen progress in photonic-crystal fibres (PCF) [14, 15] and advanced modulation formats. Which have enabled higher aggregated capacities [16–26].

1.2 Modulation Formats

Advanced optical modulation formats have emerged as a promising technology to enable higher data rates and a cost effective solution to upgrade existing fibre links.

In designing a successful system, a large number of factors have to be taken into account when choosing an appropriate modulation format. For example, in the application of ultra-long-haul high capacity links, spectral efficiency has become an important design constraint, in order to provide high data rates. Here, the performance of the nonlinear characteristics of the modulation format must be taken into account, while the relative cost of the system is less of a consideration. In contrast, when dealing with much shorter distances (e.g. terrestrial links), the relative costs becomes paramount.

In this section we will give a brief overview of the modulation formats investigated within this thesis.

1.2.1 ASK PSK FSK Pol-SK

In optical communications, modulation formats can be classified into the following schemes.

The first is amplitude shift keying (ASK). This is an intensity modulated format. Here, the amplitude of the of the signal is modulated. Its operation is depicted in figure 1.1. The

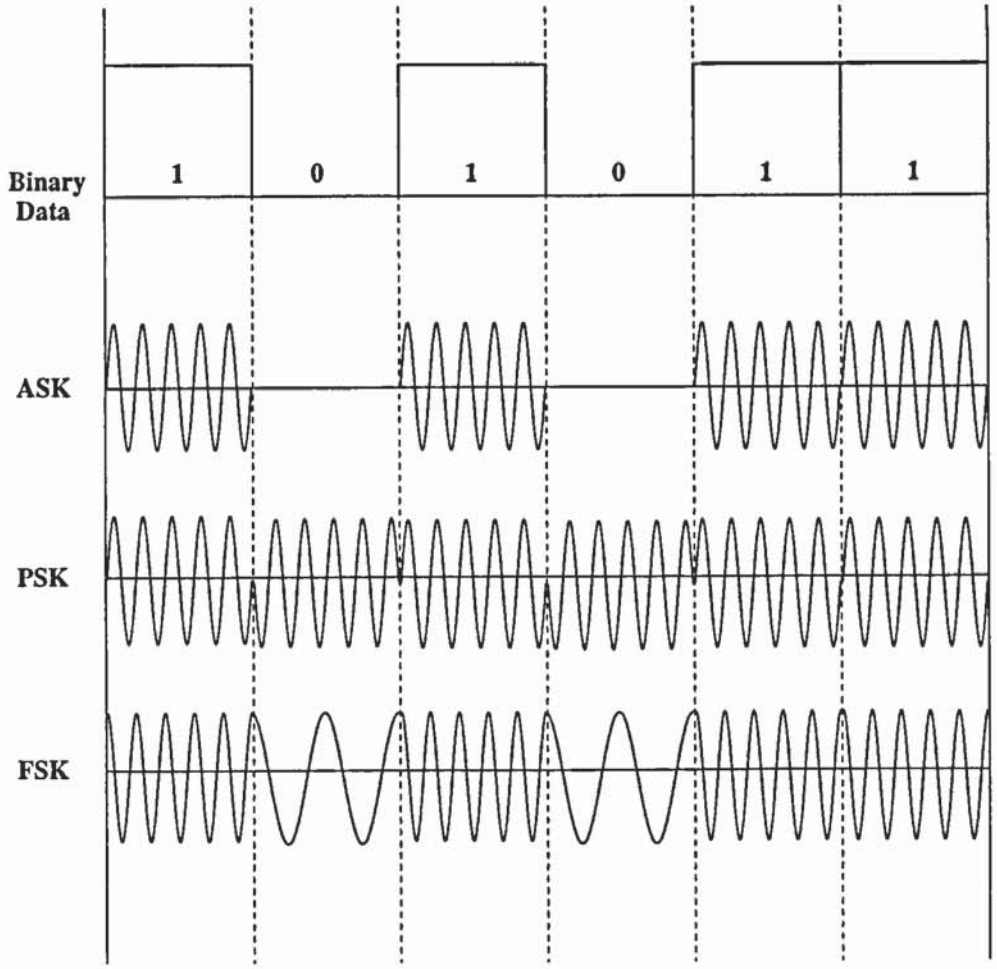

Figure 1.1: From top to bottom, digital binary data to be encoded, amplitude-shift keying (ASK), phase-shift keying (PSK) and frequency-shift keying (FSK).

data is represented in the form of a presence or absence of the pulse. In practice a digital 1 'mark', would signify an optical pulse and a 0, 'dash' would represent a zero amplitude. Due to this configuration, the ASK format is also known as on-off keying (OOK). Most digital lightwave systems utilise ASK, due to the simple implementation of optical transmitters and receivers.

Phase-shift keying (PSK), is the case where the binary data is represented by modulating the phase of the signal, as illustrated in figure 1.1. We can observe an interesting property of PSK, we note that a pulse is present in every bit slot, thus the power remains constant and appears to have a continuous wave (CW) form. In application, however, the PSK format, is rarely deployed in fibre optic communication systems, due to the requirement that the phase of the optical carrier must remain stable, so that the phase information can be decoded at the

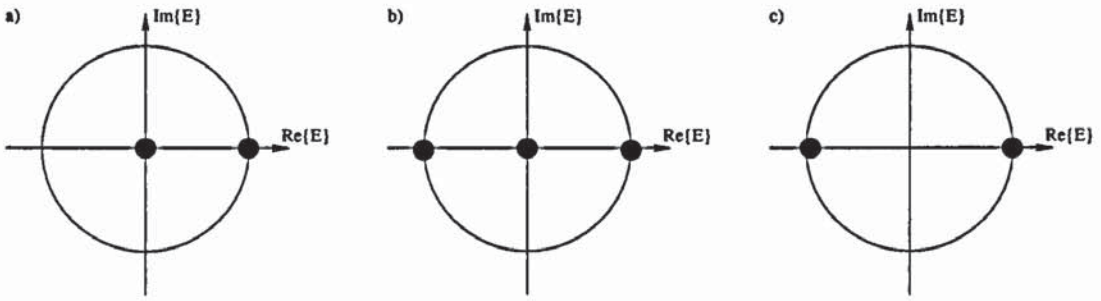

Figure 1.2: Symbol diagrams showing the complex optical field for a) RZ-OOK, b) CS-RZ and c) RZ-DPSK.

receiver without ambiguity.

The next is frequency-shift keying (FSK). The information, in this modulation format, is encoded into the optical carrier by altering the frequency of the pulse, as depicted in figure 1.1. As in the case of PSK, FSK also suffers from transmission and receiver design complications, which include a requirement of constant power in the modulated carrier.

Finally information can also be encoded onto the polarisation of light (Pol-SK), but research in this modulation format has received comparatively little attention. This is due to the requirement of active polarization management at the receiver. These complications make Pol-SK impractical for current lightwave systems as costly polarisation maintaining fibres are also required.

In this thesis we will be primarily concerned with intensity modulated and phase modulated formats.

1.2.2 RZ-OOK

The most widespread deployed format is OOK. Its two most common configurations are non-return-to-zero on-off keying (NRZ-OOK) and return-to-zero on-off keying (RZ-OOK). NRZ and RZ are both intensity modulated formats, however they differ fundamentally in the following way. NRZ pulses occupy the entire bit slot T_b of the signal (where $T_b = 1/B$ and B is the bit rate of the signal), where as RZ pulses are chosen to be shorter than T_b. The main advantage of NRZ over RZ, is that the bandwidth of an NRZ channel is smaller than that of RZ channel by a factor of approximately 2. Thus allowing a larger number of

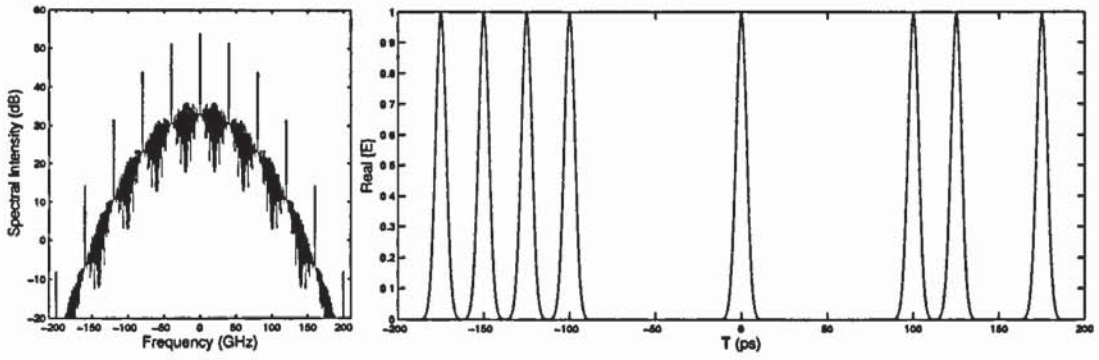

Figure 1.3: Left, spectral domain plot of RZ-OOK, and right temporal domain representation of optical bits.

NRZ channels to be multiplexed into a WDM system. However, dispersive and nonlinear effects can castrate NRZ performance by distorting the optical pulses during transmission, thus spreading them outside of their designated bit slots. This limits the application of NRZ to 10 Gb/s and below.

RZ pulse are, however, more robust to inter-symbol interference and thus preform better at higher data rates as opposed to NRZ. Figure 1.2(a), shows the symbol diagram associated with RZ-OOK. It captures the intensity and phase information of the format and maps them onto the complex optical field plane. As we can see RZ-OOK has a symbol set of $\{0, +1\}$. The temporal and spectral domains for RZ-OOK are depicted in figure 1.3. RZ-OOK transmission is limited at data-rates of 40 Gb/s and above by intra-channel nonlinearities.

1.2.3 CS-RZ

Carrier-suppressed return-to-zero (CS-RZ), is a quasi-multilevel format. It is also an intensity modulated format. However, it differs from RZ-OOK in that an alternating phase shift is applied to adjacent bits of 0 and π. This effectively gives, on average, a positive sign to half the 1 bits while the other half have a negative sign. This results in a zero mean optical field envelope. The quasi-multilevel level nature can be more clearly seen in figure 1.2(b), again the symbol diagram represents the intensity and phase information of the format (mapped onto the complex plane). The symbol set which is associated with CS-RZ are $\{-1, 0, +1\}$.

The spectral intensity and the real part of the complex field is illustrate in figure 1.4,

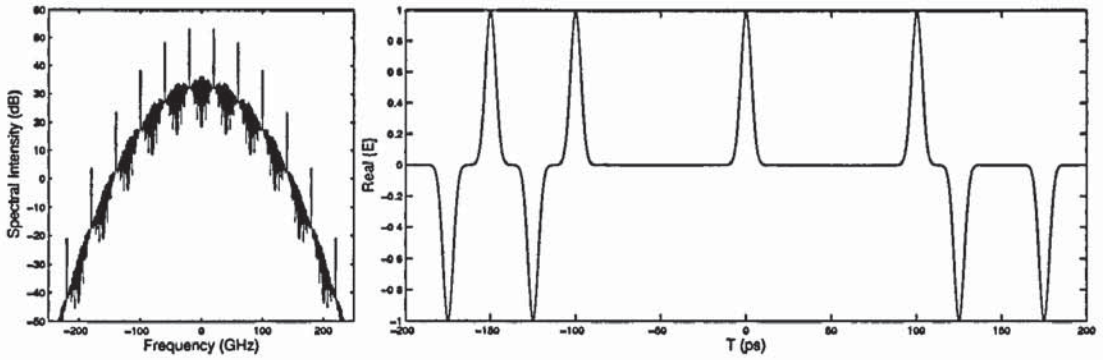

Figure 1.4: Left, spectral domain plot of CS-RZ and right, temporal domain representation of optical bits.

where we can clearly see the multilevel nature of the format.

CS-RZ has been found to preform better than RZ-OOK at data rates of 40 Gb/s [27]. It was found to resist fibre nonlinearities much more effectively and shown to be capable of suppressing intra-channel four-wave mixing (IFWM) at high powers over short distances [28].

1.2.4 RZ-DPSK

Return-to-zero differential phase-shift keying is a phase modulated format. Unlike intensity based modulation formats, the information is encoded in the change of phase between adjacent pulses. In this case, a 1 bit is represented by π change of phase, where as a 0 bit is encoded by 0 phase change. The symbol diagram associated with RZ-DPSK is shown in figure 1.2(c). We can observe that the symbol set $\{-1, 1\}$ represents the data in RZ-DPSK. The spectral intensity and the real part of the complex field is illustrate in figure 1.5, where we can see a single bit occupying each bit slot and some bits possessing a phase change of π.

The inherent advantage of deploying DPSK over OOK is a 3 dB receiver sensitivity improvement [64]. The main nonlinear effects that inhibit DPSK performance are nonlinear phase noise at lower bit rates and IFWM at higher data rates [128].

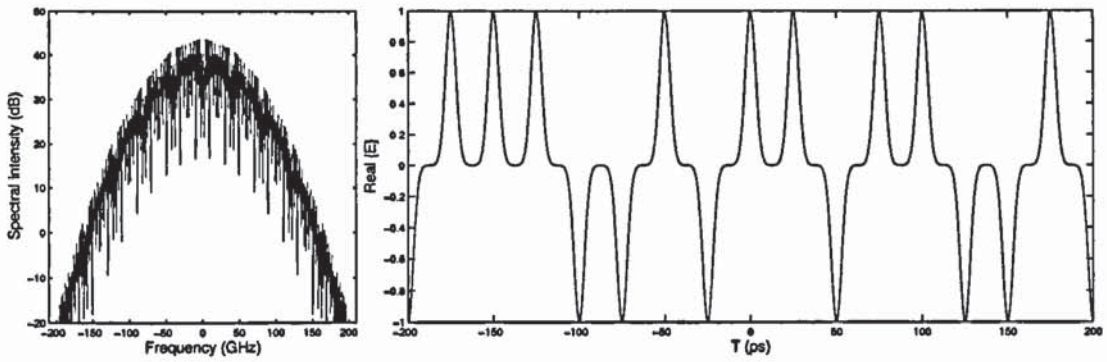

Figure 1.5: Left, spectral domain plot of RZ-DPSK and right, temporal domain representation of optical bits.

1.3 Thesis Synopsis

This thesis provides a theoretical investigation of advance modulation formats including RZ-OOK, CS-RZ and RZ-DPSK applied to fibre optic communications systems. These formats are applied to photonic devices such as semiconductor optical amplifiers (SOAs) and nonlinear optical loop mirror (NOLMs). In the first half of the thesis we will present a study of three advanced modulation formats applied to lightwave systems.

The second half will concentrate on RZ-DPSK and its application to advanced photonic devices. Finally we will look into the dispersion management of RZ-DPSK.

Throughout this thesis I have numerically implemented the various advanced modulation formats, photonic/optical devices, fibre optic transmission systems and preformed a vast array of large scaled numerical optimisations.

In this chapter, a brief historical background is presented and an overview of modulation formats.

A theoretical description of optical fibre communications is presented in Chapter 2. The effects governing the propagation of electromagnetic fields within the optical fibre are paramount to the development of modern optical fibre communications. In this chapter, we aim to present a quantitative analysis of the propagation of the electromagnetic field within a single mode optical fibre. We will begin by deriving a scalar propagation equation describing this process, known as the Nonlinear Schrödinger Equation (NLSE). The main linear and nonlinear characteristics of the optical fibre affecting optical pulse propagation will then

be considered. These include fibre attenuation, dispersion and the Kerr effect. The Kerr-induced self-phase modulation and cross-phase modulation effects will be outlined. We will then derive the fundamental soliton solution of the NLSE. The next section will deal with the analytical implementation of noise and loss in the NLSE. The last four section of the chapter will be associated with the practical generation and detection of RZ-OOK, CS-RZ and RZ-DPSK and also the principles behind vestigial side-band (VSB) and single side-band (SSB) signalling.

In the next two chapters we will primarily concentrate on the intensity modulation formats.

In Chapter 3, we investigate the use of VSB filtering for improving the system performance of RZ-OOK modulation format. We simultaneously optimise both the temporal and spectral domain characteristics of the signal. We also apply an advanced frequency allocation scheme.

In Chapter 4, we continue our analysis on VSB filtering. We now however, apply the CS-RZ modulation format and investigate both spectral and temporal characteristics of the system, with the aim of increasing the transmission performance.

Chapter 5 begins our investigation with the RZ-DPSK modulation format. We begin the chapter with a analytically investigation of the calculation of the Q-factor. The next section describes how this new method is implemented numerically. Finally we apply the format and detection scheme, to a dense wavelength division multiplexing (DWDM) optical transmission system.

In Chapter 6, we analyse a soliton-like phase-shift keying in a 40Gb/s transmission system using cascaded in-line SOAs. Numerical optimisation of the proposed soliton-like regime is presented. With the promising results obtain at 40Gb/s, we then further extend our investigation to 80Gb/s.

Chapter 7, presents a concept for all-optical regeneration of signal modulated in phase-sensitive modulation formats (such as DPSK), which is based on a new design of Raman amplified nonlinear optical loop mirror (RA-NOLM). We demonstrate simultaneous amplitude-shape regeneration and phase noise reduction in high-speed DPSK transmission systems by

use of the RA-NOLM combined with spectral filtering.

Chapter 8 we numerically investigate the dispersion map characteristics of RZ-DPSK, by rearranging arrangements of dispersion management in an existing terrestrial link, with the aim of finding a cost effective solution with reasonably good performance.

In the final chapter we present the conclusions of the work undertaken in this thesis.

Chapter 2

Theory of Fibre Optic Communication

2.1 Introduction

At the heart of modern telecommunication infrastructure is a network of information highways and submarine links consisting of optical fibre. An optical fibre is, in essence, a silica glass thread composed of a core surrounded by a cladding. Its basic operation is to confine the light, which is directed into the core of the fibre, by reflecting it off the cladding wall. Thus, guiding the beam of light along the fibre. To ensure this, both the core and the cladding have a constant index of refraction, with the core having a higher refractive index than that of the cladding. This mechanism is the basic principle of total internal reflection.

The effects governing the propagation of the guided lightwave signal within the optical fibre are paramount to the development of modern optical fibre communications. In this chapter, we aim to present a quantitative analysis of the propagation of the electromagnetic field within a single mode optical fibre. We will begin by first deriving a scalar propagation equation describing this process, known as the Nonlinear Schrödinger Equation (NLSE), in section 2.2. The main linear and nonlinear characteristics of the optical fibre which effect optical pulse propagation will then be considered in sections 2.3 and 2.4. These will include the optical loss, dispersion, the Kerr effect, self-phase modulation and cross-phase modulation. Section 2.5, will deal with the derivation of the fundamental soliton solution of the NLSE. In section 2.6 we will investigate the analytical implementation of noise and loss in

the NLSE. The practical generation and detection of RZ-OOK, CS-RZ and RZ-DPSK will be discussed in sections 2.7, 2.8 and 2.10. Here the implementation and design of the transmitter and receiver for all formats used in this thesis will be shown. While in section 2.9, we will present the basic principles behind VSB and SSB signalling.

2.2 Derivation of the Nonlinear Schrödinger Equation

In this section we will derive the equation that governs the propagation of an optical field within an optical fibre, the NLSE.

In order to derive the NLSE we need to begin from first principles and consider the propagation of electromagnetic waves within a dispersive nonlinear media. To study this phenomenon we will employ Maxwell's equations

$$\nabla \times \mathbf{E} = -\frac{\partial \mathbf{B}}{\partial t} \tag{2.1}$$

$$\nabla \times \mathbf{H} = \mathbf{J} + \frac{\partial \mathbf{D}}{\partial t} \tag{2.2}$$

$$\nabla \cdot \mathbf{D} = \rho_f \tag{2.3}$$

$$\nabla \cdot \mathbf{B} = 0 \tag{2.4}$$

where $\mathbf{E}$ and $\mathbf{H}$ are defined to be the electric and magnetic field vectors, while $\mathbf{D}$ and $\mathbf{B}$ are the electric and magnetic flux densities. The vector $\mathbf{J}$ represents the current density and ρ_f the charge density. When applying the above equations to the application of electromagnetic wave propagation within the optic fibre medium, we find $\mathbf{J} = 0$ and $\rho_f = 0$, which is due to the absence of free charges.

The flux densities $\mathbf{B}$ and $\mathbf{D}$ are related to the electric and magnetic field, $\mathbf{E}$ and $\mathbf{H}$ by [29,30]

$$\mathbf{D} = \varepsilon_0 \mathbf{E} + \mathbf{P} \tag{2.5}$$

$$\mathbf{B} = \mu_0 \mathbf{H} + \mathbf{M} \tag{2.6}$$

where **P** is defined to be the electric polarisation, **M** the magnetic polarisation, μ_0 the vacuum of permeability and ε_0 the vacuum of permittivity. Note that the fibre optic medium is nonmagnetic, therefore, $\mathbf{M} = 0$.

We proceed to produce the wave propagation equation by taking the curl of Eq. (2.1) and using Eq. (2.2) and using the above definitions of **D** and **B** we get

$$\begin{aligned} \nabla \times \nabla \times \mathbf{E} &= -\nabla \times \frac{\partial \mathbf{B}}{\partial t} \\ &= -\mu_0 \frac{\partial}{\partial t}(\nabla \times \mathbf{H}) \\ &= -\mu_0 \frac{\partial^2}{\partial t^2}(\varepsilon_0 \mathbf{E} + \mathbf{P}) \\ \nabla \times \nabla \times \mathbf{E} &= -\frac{1}{c^2}\frac{\partial^2 \mathbf{E}}{\partial t^2} - \mu_0 \frac{\partial^2 \mathbf{P}}{\partial t^2} \end{aligned} \tag{2.7}$$

where c is the speed of light within a vacuum and we've used the relation $\varepsilon_0 \mu_0 = 1/c^2$. We can further simplify Eq. 2.7 by using the vector relation

$$\nabla \times \nabla \times \mathbf{E} = \nabla(\nabla \cdot \mathbf{E}) - \nabla^2 \mathbf{E} \tag{2.8}$$

but here we note that $\nabla \cdot \mathbf{D} = 0$ due to absence of charge density ρ_f, hence $\varepsilon \nabla \cdot \mathbf{E} = 0$. As a result, we arrive at,

$$\nabla^2 \mathbf{E} = \frac{1}{c}\frac{\partial^2 \mathbf{E}}{\partial t^2} + \mu_0 \frac{\partial^2 \mathbf{P}}{\partial t^2} \tag{2.9}$$

The nonlinear behavior of optical pulse propagation, within the optic fibre, arises from the response of the dielectric medium (silica glass $Si0_2$) to intense electromagnetic fields. These interactions with the medium are characterised by the polarisation **P**. In the case of weak nonlinearity, **P** can be expressed as a power series of **E**

$$\mathbf{P} = \varepsilon_0 \left(\chi^{(1)} \cdot \mathbf{E} + \chi^{(2)} : \mathbf{EE} + \chi^{(3)} \vdots \mathbf{EEE} + \cdots \right) \tag{2.10}$$

where $\chi^{(n)} (n = 1, 2, 3, \cdots)$ are the susceptibility tensor of rank i. Here we are only interested in the first three terms of the series and have neglected tensors of order four and above. Physical, $\chi^{(n)}$ are responsible for the interaction of the field **E** with the microscopic structure

of the medium. The only way to evaluate χ^n is by the use of quantum mechanics, see [31–34] for a detailed discussion. $\chi^{(1)}$ is the linear susceptibility. The quantities $\chi^{(2)}$ and $\chi^{(3)}$ are nonlinear and known as the second and third-order susceptibility, the $\chi^{(2)}$ term can be neglected, since the crystal structure of $Si0_2$ is centrosymmetric. Thus we can now express Eq. (2.10) in terms of it linear and nonlinear components

$$\mathbf{P}(\mathbf{r},t) = \mathbf{P}_L(\mathbf{r},t) + \mathbf{P}_{NL}(\mathbf{r},t) \tag{2.11}$$

where,

$$\mathbf{P}_L(t) = \varepsilon_0 \int_{-\infty}^{\infty} \chi^{(1)}(\mathbf{r},t-t_1)\cdot\mathbf{E}(\mathbf{r},t_1)dt_1 \tag{2.12}$$

$$\mathbf{P}_{NL}(\mathbf{r},t) = \varepsilon_0 \iiint_{-\infty}^{\infty} \chi^{(3)}(t-t_1,t-t_2,t-t_3)\vdots\mathbf{E}(\mathbf{r},t_1)\mathbf{E}(\mathbf{r},t_2)\mathbf{E}(\mathbf{r},t_3)dt_1dt_2dt_3 \tag{2.13}$$

In order to proceed with the derivation a number of simplifying approximations will need to be made. We will assume $\mathbf{P}_{NL}$ to be a small perturbation to $\mathbf{P}_L$. If we consider the nonlinear response to be instantaneous, it will allow us to neglect any Raman contribution generated from molecular vibrations. Thus $\mathbf{P}_{NL}$ can be approximated by

$$\mathbf{P}_{NL} \approx \varepsilon_0 \varepsilon_{NL} \mathbf{E}(\mathbf{r},t) \tag{2.14}$$

where

$$\varepsilon_{NL} = \frac{3}{4}\chi^{(3)}_{xxxx}|\mathbf{E}(\mathbf{r},t)|^2 \tag{2.15}$$

With these simplifications we can now proceed to solve Eq. (2.9). We begin by substituting Eq. (2.12) and Eq. (2.15) into Eq. (2.9) giving us,

$$\nabla^2\mathbf{E} - \frac{1}{c^2}\frac{\partial^2\mathbf{E}}{\partial t^2} - \frac{1}{c^2}\frac{\partial^2}{\partial t^2}\left(\int_{-\infty}^{\infty}\chi^{(1)}(t-t_1)\cdot\mathbf{E}(\mathbf{r},t_1)dt_1 + \varepsilon_{NL}\mathbf{E}(\mathbf{r},t)\right) \tag{2.16}$$

Let us now apply the slowly varying envelope approximation, this in essence allows us to conveniently separate the rapidly varying part of the electric field $\mathbf{E}(\mathbf{r},t)$ into

$$\mathbf{E}(\mathbf{r},t) = \frac{1}{2}\hat{x}(E(\mathbf{r},t)e^{(-i\omega_0 t)} + c.c.) \tag{2.17}$$

where $E(\mathbf{r},t)$ is the slowly varying envelope, $\hat{x}$ is the polarisation unit vector of light and *c.c.* is the complex conjugate. With the application of the slowly varying envelope approximation to the electric field $\mathbf{E}(\mathbf{r},t)$ and the perturbative nature of P_{NL}, we are now able to treat the nonlinear parameter ε_{NL} as a constant, thus considerable simplifying the solution of Eq. (2.16). Let us now transpose Eq. (2.16) into the spectral domain by the use of the following Fourier transformations.

$$\widetilde{\mathbf{E}}(\mathbf{r},\omega-\omega_0) = \int_{-\infty}^{\infty} \mathbf{E}(\mathbf{r},t)e^{i(\omega-\omega_0)t}dt \tag{2.18}$$

$$\widetilde{\chi}^{(1)}(\omega) = \int_{-\infty}^{\infty} \chi^{(1)}(t-t_1)e^{i\omega(t-t_1)}dt_1 \tag{2.19}$$

$$\begin{aligned} \nabla^2\widetilde{E}+\frac{\omega^2}{c^2}\widetilde{E}+\frac{1}{c^2}\left(\omega^2\widetilde{\chi}\widetilde{E}+\omega^2\varepsilon_{NL}\widetilde{E}\right) &= 0 \\ \nabla^2\widetilde{E}+\frac{\omega^2}{c^2}\widetilde{E}(1+\widetilde{\chi}+\varepsilon_{NL}) &= 0 \end{aligned} \tag{2.20}$$

where we now define the dielectric constant

$$\varepsilon(\omega) = 1+\widetilde{\chi}+\varepsilon_{NL} \tag{2.21}$$

The dielectric constant also contributes to the nonlinear modification of the index of refection and becomes power dependent due to the nature of ε_{NL},

$$n(\omega,|E|^2) = n_0(w)+n_2(w)|E|^2 \tag{2.22}$$

where

$$n_2 = \frac{3}{8n_0}Re\left\{\chi^{(3)}_{xxxx}\right\} \tag{2.23}$$

Using the relation $k_0 = \frac{\omega}{c}$ and the above equations, we reduce Eq. (2.20) to

$$\nabla^2\widetilde{E}+k_0^2\varepsilon(\omega)\widetilde{E} = 0 \tag{2.24}$$

We can see that Eq. (2.24) is of the form of a second-order partial differential equation (PDE), which can be solve by applying the method of separation of variables, also known as the product method. We begin by imposing Eq. (2.24) has a solution of the form:

$$\widetilde{E}(\mathbf{r},\omega-\omega_0)=F(x,y)\widetilde{U}(z,\omega-\omega_0)e^{i\beta_o z} \tag{2.25}$$

where $\widetilde{U}(z,\omega)$ is a slowly varying function of z and ω, while $F(x,y)$ contains the transverse components of the field and β_0 is the wave number yet to be determined. We now insert our expected solution Eq. (2.25) into Eq. (2.24),

$$\widetilde{U}e^{i\beta_o z}\frac{\partial^2 F}{\partial x^2}+\widetilde{U}e^{i\beta_o z}\frac{\partial^2 F}{\partial y^2}+\frac{\partial}{\partial z}\left[\left(e^{i\beta_o z}\frac{\partial\widetilde{U}}{\partial z}+i\beta_0\widetilde{U}e^{i\beta_o z}\right)F\right]+k_o^2F\widetilde{U}e^{i\beta_o z}=0$$

$$\widetilde{U}e^{i\beta_o z}\frac{\partial^2 F}{\partial x^2}+\widetilde{U}e^{i\beta_o z}\frac{\partial^2 F}{\partial y^2}+\underbrace{Fe^{i\beta_o z}\frac{\partial^2\widetilde{U}}{\partial z^2}}_{=0}+$$

$$2i\beta_0e^{i\beta_o z}F\frac{\partial\widetilde{U}}{\partial z}-\beta_0^2F\widetilde{U}e^{i\beta_o z}+k_0^2\varepsilon(\omega)F\widetilde{U}=0 \tag{2.26}$$

Due to the application of the slowly varying approximation, the second derivative $(\partial^2/\partial z^2)$ in Eq. (2.26), can be neglected.

$$\widetilde{U}\frac{\partial^2 F}{\partial x^2}+\widetilde{U}\frac{\partial^2 F}{\partial y^2}+2i\beta_0F\frac{\partial\widetilde{U}}{\partial z}-\beta_0^2F\widetilde{U}+k_0^2\varepsilon(\omega)F\widetilde{U}=0 \tag{2.27}$$

We now move onto the procedure of separating the variables by dividing Eq. (2.27) by $F\widetilde{U}e^{i\beta_o z}$ and splitting the equation such that both the LHS and RHS in Eq. (2.27) are independent of each other.

$$\begin{aligned}\frac{1}{F}\left[\frac{\partial^2 F}{\partial x^2}+\frac{\partial^2 F}{\partial y^2}\right]+-\beta_0^2+k_0^2\varepsilon(\omega) &= -\frac{2i\beta_0}{\widetilde{U}}\frac{\partial\widetilde{U}}{\partial z}=p\\ \frac{\partial^2 F}{\partial x^2}+\frac{\partial^2 F}{\partial y^2}+F(k_0^2\varepsilon(\omega)-\beta_0^2-p) &= 0 \qquad (2.28)\\ 2i\beta_0\frac{\partial\widetilde{U}}{\partial z}+\widetilde{U}p &= 0 \qquad (2.29)\end{aligned}$$

This yields immediately two separated PDEs. With the parameter p. Lets choose p such that

$$p=\widetilde{\beta}^2-\beta_0^2 \tag{2.30}$$

Here we have chosen $\widetilde{\beta}$ to be slightly perturbed from β_0, giving rise to the following approximation.

$$\widetilde{\beta}+\beta_0 \approx 2\beta_0 \tag{2.31}$$

We finally complete the method by substituting our parameter Eq. (2.30) into our two PDEs. Hence arriving at the final form of the equations.

$$\frac{\partial^2 F}{\partial x^2}+\frac{\partial^2 F}{\partial y^2}+F(k_0^2\varepsilon(\omega)-\widetilde{\beta}^2) = 0 \tag{2.32}$$

$$2i\beta_0\frac{\partial \widetilde{U}}{\partial z}+\widetilde{U}(\widetilde{\beta}^2-\beta_0^2) = 0 \tag{2.33}$$

Equation (2.32) can be solved to obtain the modal distribution function $F(x,y)$. However this is more applicable to the study of optical pulse propagation along multi-mode fibre. Here we focus on single-mode fibre as current telecommunication links are dominated by single-mode fibre.

We now predominantly concentrate on Eq. (2.33) and the evaluation of $\widetilde{\beta}$.

$$\widetilde{\beta}=\beta(\omega)+\Delta\beta \tag{2.34}$$

Our objective now is to ultimately apply an inverse Fourier transform to Eq. (2.33) and obtain the propagation equation for $U(z,t)$. In order to do this we will need to expand $\beta(\omega)$ by the use of a Taylor expansion, thus giving

$$\beta(\omega)=\beta_0+(\omega-\omega_0)\beta_1+\frac{1}{2}(\omega-\omega_0)\beta_2+\frac{1}{6}(\omega-\omega_0)\beta_3+\cdots \tag{2.35}$$

where

$$\beta_n=\left[\frac{d^n\beta}{d\omega^n}\right]_{\omega=\omega_0} \qquad n=1,2,3,\cdots$$

From Eq. (2.31) we can obtain the useful result

$$\widetilde{\beta}^2+\beta_0^2\approx 2\beta_0(\widetilde{\beta}-\beta_0) \tag{2.36}$$

Now compiling all the information we have on $\beta(w)$, let us now use equations (2.34) (2.35) and (2.36), to further simplify Eq. (2.33).

$$\begin{aligned} i\frac{\partial \widetilde{U}}{\partial z} + \widetilde{U}(\widetilde{\beta} - \beta_0) &= 0 \\ \frac{\partial \widetilde{U}}{\partial z} &= i\widetilde{U}(\beta(\omega) + \Delta\beta - \beta_0) \\ \frac{\partial \widetilde{U}}{\partial z} &= i\widetilde{U}\left((\omega - \omega_0)\beta_1 + \frac{1}{2}(\omega - \omega_0)^2\beta_2 + \Delta\beta\right) \end{aligned} \tag{2.37}$$

We are now in a position to apply an inverse Fourier transform to the above equation and transform it back to the time domain. On applying the transform we note the relation $i(\omega - \omega_0) \Longleftrightarrow \frac{\partial}{\partial t}$, thus the resulting equation for $U(z,t)$

$$\frac{\partial U}{\partial z} + \beta_1 \frac{\partial U}{\partial t} + i\frac{\beta_2}{2}\frac{\partial^2 U}{\partial t^2} = i\Delta\beta \tag{2.38}$$

The small perturbation term $\Delta\beta$ contains both the nonlinear effects of propagation and fibre loss. It can be evaluated [45] and is related to the dielectric constant and absorption coefficient via the following.

$$\Delta\beta = \frac{k_0 \iint_{\infty}^{\infty} \Delta n |F(x,y)|^2 dxdy}{\iint_{\infty}^{\infty} |F(x,y)|^2 dxdy} \tag{2.39}$$

and

$$\Delta n = n_2 |E|^2 + \frac{i\alpha}{2k_0} \tag{2.40}$$

Thus finally arrive at the Nonlinear Schrödinger Equation, which governs the propagation of scalar optical pulse along a single-mode fibre,

$$\frac{\partial U}{\partial z} + \beta_1 \frac{\partial U}{\partial t} + i\frac{\beta_2}{2}\frac{\partial^2 U}{\partial t^2} + \frac{\alpha}{2}U = i\gamma|U|^2 U \tag{2.41}$$

where γ, the nonlinear parameter is defined to be

$$\gamma = \frac{n_2 \omega_0}{c A_{eff}} \tag{2.42}$$

where A_{eff} is known as the effective core area and defined to be

$$A_{eff} = \frac{\left(\iint_{\infty}^{\infty} |F(x,y)|^2 dxdy\right)^2}{\iint_{\infty}^{\infty} |F(x,y)|^4 dxdy} \tag{2.43}$$

As you can see from Eq. (2.41) the NLSE encapsulates all of the most important linear and nonlinear optical effects which characterises optical pulse propagation. It includes the following linear effects, chromatic dispersion, through the terms β_1 and β_2 and optical loss, through the attenuation term α. The nonlinear characteristics of the fibre are described by the γ parameter.

Let us now introduce two length scales [46], which will allow us to characterise the propagation properties of an optical fibre. More specifically, they will allow us to determine the relative contributions of both the dispersion and nonlinearity of the fibre. The first length scale is the dispersion length (L_D) and gives a measure of the distances at which dispersion becomes an important factor. It is defined as,

$$L_D = \frac{T_o^2}{|\beta_2|} \tag{2.44}$$

where β_2 is the second order dispersion term and T_0 is the initial temporal characteristics of the pulse.

The nonlinear length (L_{NL}) is defined to be,

$$L_{NL} = \frac{1}{\gamma P_0} \tag{2.45}$$

where P_0 is the initial pulse peak power.

Using these length scales we can now define four regions in which the different effects dominate the pulse evolution along the fibre. The first case is where $L \ll L_D$ and $L \ll L_{NL}$, here neither the dispersive or the nonlinear effects dominate. The second is where $L \geq L_D$ and $L \ll L_{NL}$, here dispersive effects dominate propagation. The third is where $L \ll L_D$ and $L \geq L_{NL}$, here nonlinear effects dominate propagation. Finally, the fourth scenario is where $L \geq L_D$ and $L \geq L_{NL}$, here both dispersive and nonlinear effects dominate propagation. However, their interaction creates the conditions necessary for the support of solitary waves, in the situation of pulse dispersion, in the anomalous-dispersion region ($\beta < 0$) and pulse compression in normal-dispersion region $\beta > 0$.

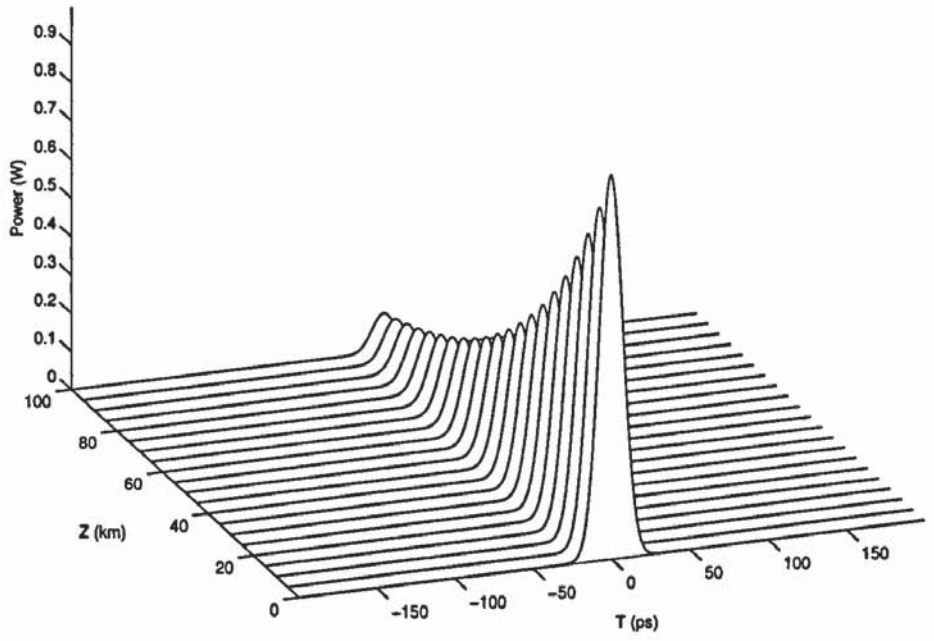

Figure 2.1: Pulse attenuation due to optical loss in the absence of dispersion and nonlinearity. The launched Gaussian pulse has a initial pulse width of 25 ps.

2.3 Linear Optical Fibre Characteristics

In this section we will examine the main linear properties of equation 2.41, that limits the performance of optical communications. The main two linear effects that we will consider are, optical attenuation and group velocity dispersion (GVD).

2.3.1 Optical Loss

Optical loss limits the performance of lightwave systems by absorbing the power of propagating optical pulses. The attenuation of the pulses leads to a lower signal power received at the receiver, thus inherently limiting propagation distances. This was overcome, with the advent of optical amplifiers, which when distributed along the transmission fibre, would enable transmission distances into thousands of kilometers.

In figure 2.1, we can observe the effects of attenuation on a optical pulse. Here we have

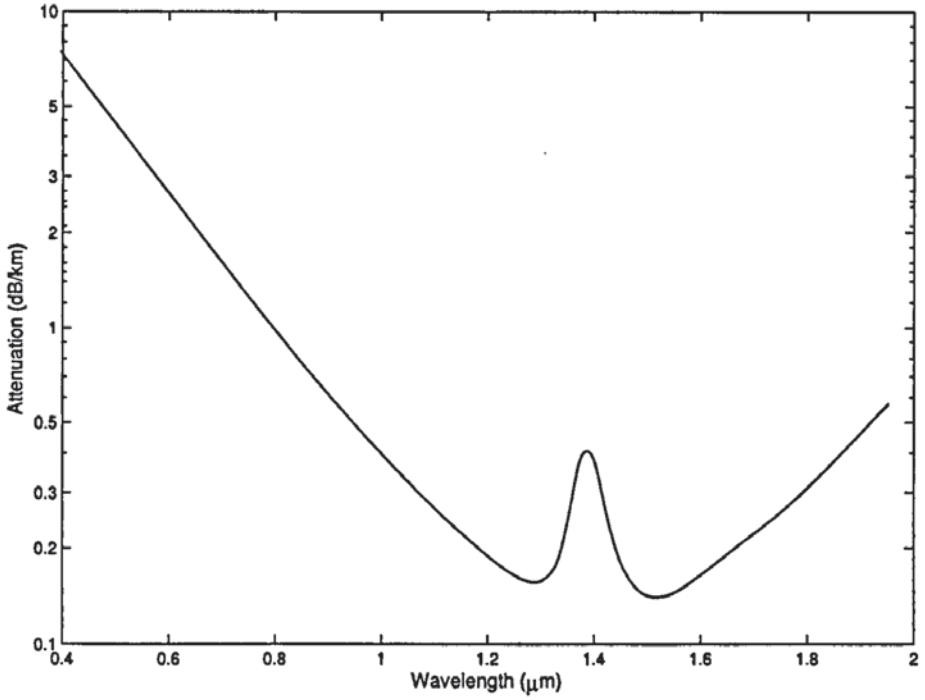

Figure 2.2: Optical attenuation profile of single mode fibre.

pulse attenuation of a Gaussian pulse with a initial pulse width of 25 ps ($T_0 = 25$), in the absence of fibre dispersion and nonlinearity.

By neglecting the dispersive and nonlinear terms in equation 2.41, we can obtain the equation which governs the attenuation of optical pulses propagating along the fibre,

$$\frac{\partial U}{\partial z} = -\frac{\alpha}{2}U \tag{2.46}$$

where α is the absorption coefficient. We solve the above equation to obtain the output power of an optical pulse after traveling a distance L km along the fibre.

$$U = U_0 e^{-\alpha L} \tag{2.47}$$

Physically the action of optical attenuation can be described through physical effects of the fibre, as outlined below.

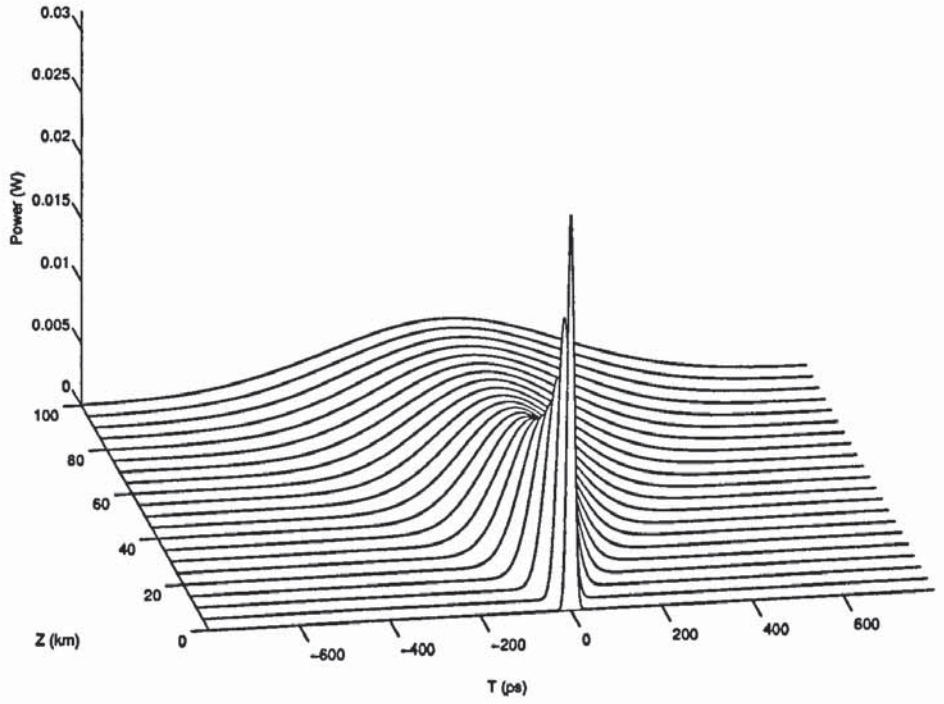

Figure 2.3: GVD induced pulse broadening due to optical second order dispersion term in NLSE, in the absence of loss and nonlinearity. The launched Gaussian pulse has a initial pulse width of 25 ps.

Material Absorption

The effects of material absorption can be define into two categories, intrinsic and extrinsic.

Intrinsic absorption is associated with the molecular properties of silica ($Si0_2$). Here the $Si0_2$ molecules interact with the incident photons via the action of electronic and vibrational resonances. The electronic resonances are associated with the loss in the ultraviolet region ($\lambda < 0.4\mu$m), while the vibrational resonances occur in the infrared region ($\lambda > 7\mu$m).

Extrinsic absorption is associated with impurities present in the fibre. The main contribution of extrinsic absorption is from the presence of water vapour. The HO ions fused into the silica fibre which courses vibrational resonances at $\lambda = 1.4\mu$m, this results in significant losses, as observed in figure 2.2.

Rayleigh Scattering

Rayleigh scattering is associated with microscopic fluctuations in the density of the fibre. These local density fluctuations result in random perturbations of the refractive index. This contributes to the loss of the fibre as light is scatted as it propagates along the optical fibre. This intrinsic loss mechanism is fundamental in silica fibre and represents the lower attenuation limit.

Waveguide Imperfections

Waveguide imperfections contribute to fibre loss in the form of imperfections of the optical fibre. These include imperfections in core-cladding interface, i.e. random variations in the core radius. Bends in the fibre and many others including splices. A more detailed description of theses effects can be found in references [35–42].

2.3.2 Group Velocity Dispersion

Group velocity dispersion (GVD) dominates pulse propagation in the regions $L_D \leq L$ and $L \ll L_{NL}$. The effect of GVD is to broaden or narrow the pulse as it propagates along the optical fibre. This dispersion-induced pulse broadening/narrowing is produced as different frequency components travel at slightly different velocities. In essence higher frequency components travel at slower speed, as apposed to the lower frequency components which travel at greater velocity, in normal dispersion fibre ($\beta_2 > 0$). The opposite is true while in anomalous dispersion fibre ($\beta_2 < 0$).

In figure 2.3 illustrates the detrimental effect GVD has on an optical pulse. Here we can clearly see the how the pulse broadens along the fibre. However, the energy of the pulse is preserved. We can obtain an expression describing the pulse broadening as a function of the second order dispersion constant (β_2) and propagation distance (z), by solving the resulting equation arising from neglecting the loss and nonlinearity in equation 2.41. The solution of which is [43]

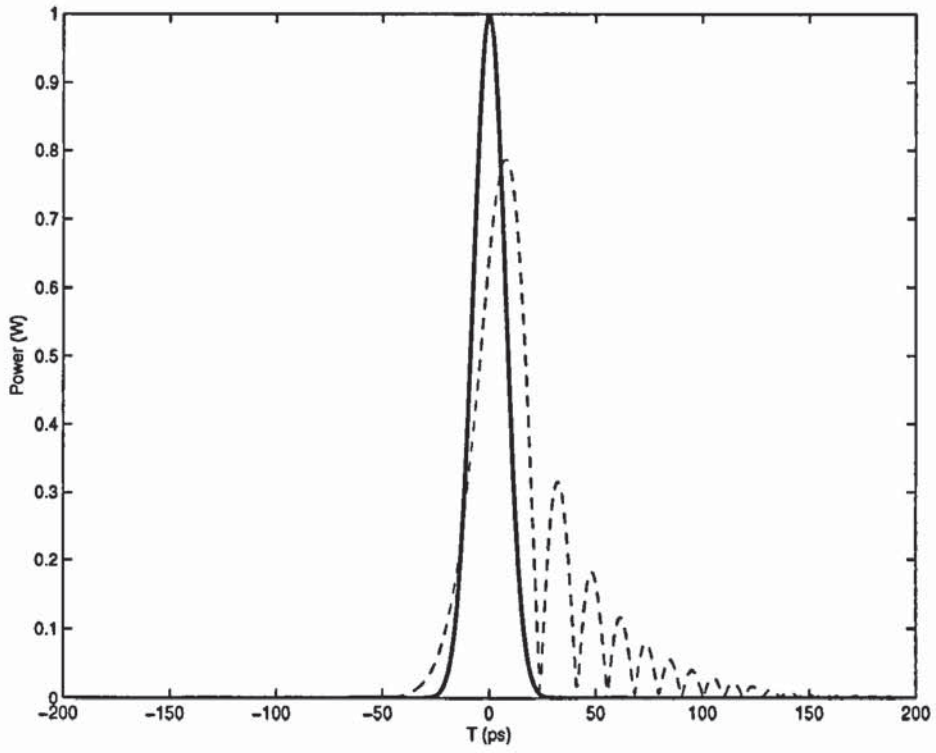

Figure 2.4: Third order induced pulse broadening due to optical third order dispersion term in the generalised Nonlinear Schrödinger equation (GNLSE), in the absence of loss and nonlinearity. The launched Gaussian pulse has a initial pulse width of 25 ps, a peak power of 1W, the second order dispersion term was set to D = 0 ps/nm/km, the third order dispersion term was set to S = 3 ps/nm^2/km. The solid line represents the pulse at 0 km and the dashed line shows the pulse profile after 500 km

$$t_1(z) = t_0 \left[1 + \left(\frac{z\beta_2}{t_0^2} \right)^2 \right] \tag{2.48}$$

where t_1 is the pulse width after propagating a distance z along the fibre and t_0 is the initial pulse width. It can be seen from the above equation that shorter pulses are affected by GVD more intensely than pulses with larger t_0.

We can observe higher order dispersive effects by neglecting the second order dispersion term, fibre loss and nonlinearity. Figure 2.4 depicts the action of third order dispersion on a Gaussian pulse with an initial pulse width of 25 ps. Its effect is to distort the pulse in such a way as to break the symmetry of the Gaussian pulse and creates an oscillating tail.

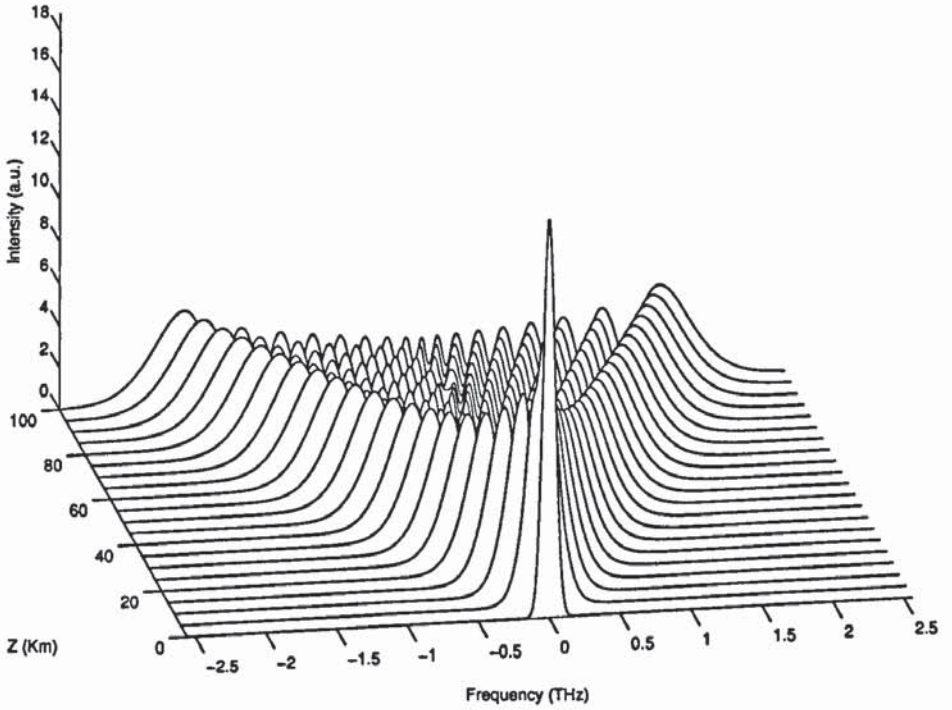

Figure 2.5: SPM induced spectral broadening of a Gaussian pulse, in the absence of loss and dispersion. The launched Gaussian pulse has a initial pulse width of 25 ps.

2.4 Nonlinear Optical Fibre Characteristics

Under the action of intense electromagnetic fields, the dielectric medium (silica optic fibre) exhibits nonlinear characteristics. These effects manifested itself through changes in the refractive index with optical power or to scattering phenomenon. The Kerr effect is responsible for the power dependence of the refractive index.

The scattering phenomenon occurs when the optical field interacts with the microscopic properties of the fibre producing local phonons. Two fundamental scattering processes are involved. The first is Brillouin scattering, here the field interacts with the lattice structure and acoustic phonons are produced. The second is Raman scattering, here optical phonons are created.

2.4.1 Kerr Effect

The Kerr effect is due to the $\chi^{(3)}$ term in the susceptibility tensor. It manifests it self through self phase modulation, cross phase modulation and fourwave mixing. Through out this thesis we assume a linearly polarized field. The components of the third order susceptibility tensor that govern the nonlinearity are given by [44]

$$n_2 = \frac{3}{8n}\mathrm{Re}\left(\chi^{(3)}_{xxxx}\right) \tag{2.49}$$

2.4.2 Self Phase Modulation and Cross Phase Modulation

The regions in which nonlinearity dominates optical pulse is defined as $L_{NL} \leq L$ and $L \ll L_D$. The two main nonlinear effects that are associated in this region are self phase modulation (SPM) and cross phase modulation (XPM).

The result of SPM on a optical pulse is to give an intensity dependent phase shift which results in distorting the pulse spectrum. However, the optical peak power and pulse width are unaffected, i.e. the temporal pules shape remains undistorted. This effect can be seen is figure 2.5. Here the we launch a Gaussian pulse with a initial pulse width of 25 ps, we observe the spectral broadening of the pulse as it propagates along the fibre.

XPM arises when two or more optical channel are propagated simultaneously along the fibre. Here the pulses experience a XPM-induce phase shift as they overlap in the time domain.

2.5 Solitary Wave Solution

In this section we aim to derive the solitary wave solution of the NLSE. Following in the spirit of [47], we begin from the NLSE normalised in soliton units, see section 2.6 for normalisation details.

$$A_\xi = \frac{i}{2}A_{\tau\tau} + i|A|^2A \tag{2.50}$$

Let us search for a solution of the normalised NLSE where the amplitude of A is stationary along the length of the fibre ξ, i.e. $|A|^2 = f(\tau)$ where $f(\tau)$ is real and only dependent on τ. Hence let us assume A to take the form of

$$A(\xi,\tau) = f(\tau)e^{i\phi(\xi,\tau)} \tag{2.51}$$

where $\phi(\xi,\tau)$ is also real. Substituting equation (2.51) into (2.50)

$$\begin{aligned}\frac{\partial}{\partial\xi}\left[fe^{i\phi}\right] &= \frac{i}{2}\frac{\partial^2}{\partial^2\tau}\left[fe^{i\phi}\right] + i\left|fe^{i\phi}\right|^2 fe^{i\phi} \\ i\frac{\partial}{\partial\xi}\left[fe^{i\phi}\right] &+ \frac{1}{2}\frac{\partial^2}{\partial^2\tau}\left[fe^{i\phi}\right] + f^3e^{i\phi} = 0\end{aligned} \tag{2.52}$$

We now perform the partial derivatives to give

$$\begin{aligned}-fe^{i\phi}\frac{\partial\phi}{\partial\xi} + \frac{1}{2}\frac{\partial}{\partial\tau}\left[\frac{\partial f}{\partial\tau}e^{i\phi} + ife^{i\phi}\frac{\partial\phi}{\partial\tau}\right] + f^3e^{i\phi} = 0 \\ -fe^{i\phi}\phi_\xi + \frac{1}{2}\left[e^{i\phi}f_{\tau\tau} + ie^{i\phi}f_\tau\phi_\tau + ie^{i\phi}f_\tau\phi_\tau - fe^{i\phi}(\phi_\tau)^2 + ife^{iphi}\phi_{\tau\tau}\right] \\ + f^3e^{i\phi} = 0\end{aligned} \tag{2.53}$$

After some simplification we arrive at

$$-f\phi_\xi + \frac{1}{2}\left[f_{\tau\tau} - f(\phi_\tau)^2 + if\phi_{\tau\tau}\right] + if_\tau\phi_\tau + f^3 = 0 \tag{2.54}$$

We now separate the above equation into its real and imaginary parts, to give

$$-f\phi_\xi + \frac{1}{2}f_{\tau\tau} - \frac{f}{2}(\phi_\tau)^2 + f^3 = 0 \tag{2.55}$$

$$\frac{1}{2}f\phi_{\tau\tau} + f_\tau\phi_\tau = 0 \tag{2.56}$$

If we now use the following,

$$\frac{\partial}{\partial\tau}\left(f^2\frac{\partial\phi}{\partial\tau}\right) = 2f\frac{\partial f}{\partial\tau}\frac{\partial\phi}{\partial\tau} + f^2\frac{\partial^2\phi}{\partial\tau^2} \tag{2.57}$$

we can rewrite the real and imaginary parts to give

$$\frac{\partial\phi}{\partial\xi}+\frac{1}{2}\left(\frac{\partial\phi}{\partial\tau}\right)^2 = \frac{1}{f}\left(\frac{1}{2}\frac{\partial^2 f}{\partial\tau^2}+f^3\right) \tag{2.58}$$

$$\frac{f}{2}\frac{\partial^2\phi}{\partial\tau^2}+\frac{\partial f}{\partial\tau}\frac{\partial\phi}{\partial\tau} = \frac{\partial}{\partial\tau}\left(f^2\frac{\partial\phi}{\partial\tau}\right)=0 \tag{2.59}$$

Putting the above two equations in a more convenient form,

$$\frac{\partial\phi}{\partial\xi}=-\frac{1}{2}\left(\frac{\partial\phi}{\partial\tau}\right)^2+g(\tau) \tag{2.60}$$

and from integrating equation (2.59) gives us

$$\frac{\partial\phi}{\partial\tau}=\frac{1}{f^2}C(\xi) \tag{2.61}$$

where $g(\tau)$ is the right hand side of equation (2.58) and only dependent on τ, also $C(\xi)$ is a function of the normalised distance ξ. Given that we have two equations for $\phi(\xi\tau)$, we can therefore apply the compatibility condition by using

$$\frac{\partial^3\phi}{\partial\xi^2\tau}=\frac{\partial^3\phi}{\partial\tau\xi^2} \tag{2.62}$$

Applying the above to equations (2.60) and (2.61) leads to

$$\frac{\partial^2 C}{\partial\xi^2}=\frac{2}{f(\tau)^2}\frac{\partial C}{\partial\xi} \qquad \frac{\partial C}{\partial\xi}=\frac{2}{f(\tau)^2} \tag{2.63}$$

which implies

$$C(\xi)=C_0=constant \tag{2.64}$$

We perform the integration of equations (2.60) and (2.61),

$$\int d\phi = \int^{\tau}\frac{C_0}{f^2(\tau')}d\tau' \tag{2.65}$$

$$\int d\phi = \int\left(-\frac{1}{2}\left(\frac{\partial\phi}{\partial\tau}\right)^2+g(\tau)\right)d\xi \tag{2.66}$$

and combine both equation (2.65) and (2.66) together to get $\phi(\xi,\tau)$

$$\phi(\xi,\tau) = \int^{\tau} \frac{C_0}{f^2(\tau')}d\tau' + \left(-\frac{1}{2}\frac{C_0^2}{f^4(\tau)} + g(\tau)\right)\xi + \sigma_0 \tag{2.67}$$

$$\phi(\xi,\tau) = \int^{\tau} \frac{C_0}{f^2(\tau')}d\tau' + K_0\xi + \sigma_0 \tag{2.68}$$

where

$$K_0 = -\frac{1}{2}\frac{C_0^2}{f^4(\tau)} + g(\tau) \tag{2.69}$$

Both K_0 and σ_0 are real constants. Now we substitute $g(\tau)$ back into K_0

$$K_0 = -\frac{1}{2}\frac{C_0^2}{f^4} + \frac{1}{f}\left(\frac{1}{2}f_{\tau\tau} + f^3\right) \tag{2.70}$$

after some rearranging we arrive at

$$\frac{\partial^2 f(\tau)}{\partial\tau^2} = \frac{C_0^2}{f^3(\tau)} - 2f^3(\tau) + 2K_0 f(\tau) = -\frac{\partial}{\partial f}V(f) \tag{2.71}$$

We now integrate the above equation to find the potential function $V(f)$

$$V(f) = -K_0 f^2 + \frac{1}{2}f^4 + \frac{C_0^2}{2f^2} \tag{2.72}$$

With no losses in equation (2.71), we can apply the conservation of the total energy to give

$$\frac{1}{2}\left(\frac{df}{d\tau}\right)^2 + V(f) = E_0 \tag{2.73}$$

We can see that a stable solution can be found if we set $E_0 = 0$, $C_0 = 0$ and $K_0 > 0$. Substituting these values into equation (2.73) gives

$$\frac{1}{2}\left(\frac{df}{d\tau}\right) + \frac{1}{2}f^4 - K_0 f^2 = 0 \tag{2.74}$$

Now we make a change of variable of the form $f = \sqrt{\chi}$, the above equation now becomes,

$$\begin{aligned}\frac{df}{d\tau} &= \frac{df}{d\chi}\frac{d\chi}{d\tau} = \frac{1}{2}\chi^{-\frac{1}{2}}\frac{d\chi}{d\tau} \\ \left(\frac{d\chi}{d\tau}\right)^2 &= 8K_0\chi^2 - 4\chi^3 \\ \left(\frac{d\chi}{d\tau}\right)^2 &= -4\chi^2(\chi-\eta^2) \end{aligned} \tag{2.75}$$

where η is an arbitrary constant and $K_0 > \eta^2/2$. We can now integrate equation (2.75) to give

$$\chi = \eta^2 \text{sech}^2[\eta(\tau-\tau_0)] \tag{2.76}$$

We now change variables back to f to get the final solution of $f(\tau)$

$$f(\tau) = \eta \text{sech}[\eta(\tau-\tau_0)] \tag{2.77}$$

where τ_0 represents the centre of the localised solution. Finally substituting $\phi(\xi,\tau)$, $f(\tau)$ and K_0 into equation (2.51) we arrive at the solitary wave solution for the Nonlinear Schrödinger Equation, Eq.(2.50)

$$A(\xi,\tau) = \eta \text{sech}[\eta(\tau-\theta_0)]e^{i\frac{\eta^2}{2}\xi+i\sigma} \tag{2.78}$$

2.6 Optical Noise

Following the method of [48], our aim is add noise to the NLSE. We will begin from the NLSE for a lossy fibre which is periodically compensated by lumped amplifiers.

$$\frac{\partial U}{\partial z} = f(z)U + i\frac{\langle\beta_2\rangle}{2}\frac{\partial^2 U}{\partial t^2} + i\sigma|U|^2U \tag{2.79}$$

where $\sigma = 2\pi n_2/(\lambda A_{eff})$ is the nonlinear coefficient, n_2 the Kerr coefficient of the fibre, λ the wavelength and A_{eff} the effective area of the fibre. The function $f(z)$ represents the periodic loss gain cycle. Substitute the following transformation into the above

$$U(z) = F(z)V(z) \tag{2.80}$$

where

$$F(z) = e^{\int_0^z f(z')dz'} \tag{2.81}$$

After some manipulation we get

$$V_z = i\frac{\langle\beta_2\rangle}{2}V_{tt} + i\sigma|F(z)|^2|V(z)|^2V \tag{2.82}$$

where subscripts represent partial derivatives. The function $|F(z)|^2$ represents the periodic loss and amplification of the signal. Hence it is a periodic discontinuous function with a period equivalent to the amplification distance L. In between the amplifiers $|F(z)|^2$ will have the form

$$|F(z)|^2 = e^{-\alpha z} \tag{2.83}$$

By using Fourier analysis we are able to expand $|F(z)|^2$ in terms of a Fourier series by using

$$f(z) = \sum_{\infty}^{\infty} c_n e^{\frac{i2\pi nz}{L}}, c_n = \frac{1}{4L}\int_0^L f(x)e^{-\frac{i2\pi nz}{L}}dz \tag{2.84}$$

to give

$$|F(z)|^2 = \sum_{-\infty}^{\infty} e^{i\frac{2\pi nz}{L}} f_n \tag{2.85}$$

where

$$f_n = \frac{1 - e^{-\alpha L}}{\alpha L + i2\pi n} \tag{2.86}$$

Taking the z independent term and using the amplifier gain to be $G = \exp(-\alpha L)$ we get

$$f_0 = \frac{G-1}{G\ln G} \tag{2.87}$$

Now we perturbative expand V

$$V = V_0 + LV_1 + \ldots \tag{2.88}$$

Substitute this into the NLS and taking the lowest order terms we arrive at

$$\frac{\partial V_0}{\partial z} = i\frac{\langle \beta_2 \rangle}{2}\frac{\partial^2 V_0}{\partial t^2} + i\sigma\frac{G-1}{G\ln G}|V_0|^2 V_0 \tag{2.89}$$

The above equation can be seen to describe the evolution of the optical field along a 1-dimensional lattice, with amplifiers situated on each node. We can now proceed to add amplified spontaneous emission (ASE) noise to the amplifiers. This is accomplished by distributing the noise function across the system nodes. Equation (2.89) now becomes

$$\frac{\partial V_0}{\partial z} = i\frac{\langle \beta_2 \rangle}{2}\frac{\partial^2 V_0}{\partial t^2} + i\sigma\frac{G-1}{G\ln G}|V_0|^2 V_0 + N(z,t) \tag{2.90}$$

The ASE term is well defined to possess the following properties

$$\langle N_i(z,t) \rangle = 0 \tag{2.91}$$

$$\langle N_i(z,t) N_j(z',t') \rangle = 0 \tag{2.92}$$

$$\langle N_i(z,t) N_j^*(z',t') \rangle = \hbar w_0 F \frac{(G-1)}{L}\delta(z-z')\delta(t-t') \tag{2.93}$$

where w_0 is the angular carrier frequency of the soliton and F is the inversion factor of the amplifier. We will assume total inversion and set $F = 1$. Lets rescale equation (2.90) in terms of soliton units.

$$\xi = \frac{z}{L_D} \qquad \tau = \frac{t}{t_0} \tag{2.94}$$

$$d\xi = \frac{dz}{L_D} \qquad d\tau = \frac{dt}{t_0} \tag{2.95}$$

where

$$L_D = \frac{t_0^2}{\langle \beta_2 \rangle} \tag{2.96}$$

Substituting equation (2.94) and (2.95) into equation (2.90) we get

$$\begin{aligned}\frac{1}{L_D}\frac{\partial V_0}{\partial \xi} &= i\frac{\langle \beta_2 \rangle}{2t_0^2}\frac{\partial^2 V_0}{\partial \tau^2} + i\sigma\frac{G-1}{G\ln G}|V_0|^2 V_0 + L_D N(z,t) \\ \frac{\partial V_0}{\partial \xi} &= \frac{i}{2}\frac{\partial^2 V_0}{\partial \tau^2} + i\sigma L_D\frac{G-1}{G\ln G}|V_0|^2 V_0 + L_D N(z,t)\end{aligned} \tag{2.97}$$

Now we rescale the field using

$$A = \frac{V_0}{V'} \qquad P_0 = \frac{\langle \beta_2 \rangle}{\sigma t_0^2} \tag{2.98}$$

where V' is the normalisation field

$$V' = \sqrt{P} = \left[\frac{G-1}{G\ln G}\sigma L_D\right]^{-1/2} = \left[\frac{G\ln G}{G-1}P_0\right]^{1/2} \tag{2.99}$$

Equation (2.97) now becomes

$$\begin{aligned}V' A_\xi &= \frac{i}{2}V' A_{\tau\tau} + i\sigma\frac{G-1}{G\ln G}V'^2|A|^2 V' A + L_D N(z,t) \\ A_\xi &= \frac{i}{2}A_{\tau\tau} + i|A|^2 A + n(\xi,\tau)\end{aligned} \tag{2.100}$$

where

$$n(\xi,\tau) = \frac{L_D}{V'}N(z,t) \tag{2.101}$$

Equation (2.91) and (2.92) remain the same however, equation 2.93 becomes

$$\begin{aligned}\langle n_i(\xi,\tau) n_j^*(\xi',\tau')\rangle &= \frac{L_D^2}{V'^2}\hbar w_0\frac{(G-1)}{L}\delta(z-z')\delta(t-t') \\ \langle n_i(\xi,\tau) n_j^*(\xi',\tau')\rangle &= \frac{L_D^2}{V'^2}\hbar w_0\frac{(G-1)}{L}\frac{\delta(\xi-\xi')}{z_0}\frac{\delta(\tau-\tau')}{t_0} \\ \langle n_i(\xi,\tau) n_j^*(\xi',\tau')\rangle &= \frac{L_D^2\sigma}{t_0}\hbar w_0\frac{G-1}{G\ln G}\frac{(G-1)}{L}\delta(\xi-\xi')\delta(\tau-\tau')\end{aligned} \tag{2.102}$$

Finally

$$\langle n_i(\xi,\tau)n_j^*(\xi',\tau')\rangle = \langle n\rangle\delta(\xi-\xi')\delta(\tau-\tau')$$

where

$$\langle n\rangle = \hbar w_0 \frac{\sigma L_D^2}{t_0}\frac{(G-1)^2}{G(\ln G)^2} \tag{2.103}$$

Lets assume that the perturbation due to noise is small and that the soliton time $T = 0$. The statistical properties of the noise term

$$n_i(\xi) = \int dt f_i(\tau)n(\xi,\tau) \tag{2.104}$$

$$\langle n_i\rangle = Re\int d\tau f_i(\tau)\langle n(\xi,\tau)\rangle = 0 \tag{2.105}$$

$$\langle n_i(\xi)n_j(\xi')\rangle = Re\int d\tau f_i(\tau)\langle n(\xi,\tau)\rangle Re\int d\tau' f_i(\tau')\langle n(\xi',\tau')\rangle \tag{2.106}$$

By using equation (2.103)

$$\langle n_i(\xi)n_j(\xi')\rangle = \frac{\langle n_i\rangle}{2}\int d\tau|f_i|^2\delta(\xi-xi') \tag{2.107}$$

It can be shown that $\langle n_i(\xi)n_j(\xi')\rangle = 0$ for $i \neq j$. Hence the above equation becomes

$$\langle n_i(\xi)n_j(\xi') = n_i\delta(\xi-\xi')\delta_{i,j} \tag{2.108}$$

where

$$n_i = \frac{\langle n\rangle}{2}\int dt|f(\tau)|^2 \tag{2.109}$$

Using

$$f_T' = \frac{f_T}{q^2}, \qquad f_T = q\tanh[q(\tau-T)]A_0 \tag{2.110}$$

where

$$q = \left[\frac{G\ln G\langle\beta_2\rangle}{(G-1)\sigma}\right]^{1/2}\frac{1}{t_0} \tag{2.111}$$

and A_0 is the fundamental soliton solution. We get the noise figure D to be

$$n_T = \frac{\langle n \rangle}{q^3} \frac{\pi^2}{12} = D \tag{2.112}$$

2.7 RZ-OOK Generation and Detection

RZ-OOK is one of the most simplest modulation formats to implement practically (excluding NRZ-OOK) in optical fibre communications. Its simplicity can be attributed to the way information is represented. As its name suggest, data is encoded in the following way: a logic "1" is represented by the presents of an optical pulse, while a "0" is represented by an absence of a pulse.

In this section we will show a typical practical implementation of RZ-OOK transmitter and receiver designs.

2.7.1 Transmitter Design

By far the easiest way of generating an OOK carrier signal is by using a directly modulated laser (DML). Here data is modulated onto the driving current of the laser, thus switching the emerging light on and off. However, the main drawback of modulating the signal with a DML (especially at high bit rates, e.g. 40 Gbit/s) is their highly component-specific chirp. Which broadens the optical spectrum of the signal and increases signal distortions and impedes its performance in DWDM applications.

A more suitable way of modulating the carrier chirp free and at high bit rates is by the use of a Mach-Zehnder modulator (MZM). Unlike the DML, the MZM modulates the carrier by exploiting the principle of interference. This is done by modulating the optical phase of the signal. Its internal operation is as follows, the incoming beam is split into two (via a coupler) and propagates along the arms of the MZM. Each arm (or just one) is equipped with a phase modulator which allows the two beams to acquire a phase difference between them. The phase is controlled by the applied voltage, $V_{1,2}$, to the phase modulator. The beams finally interfere constructively/destructively at the output coupler, thus producing an

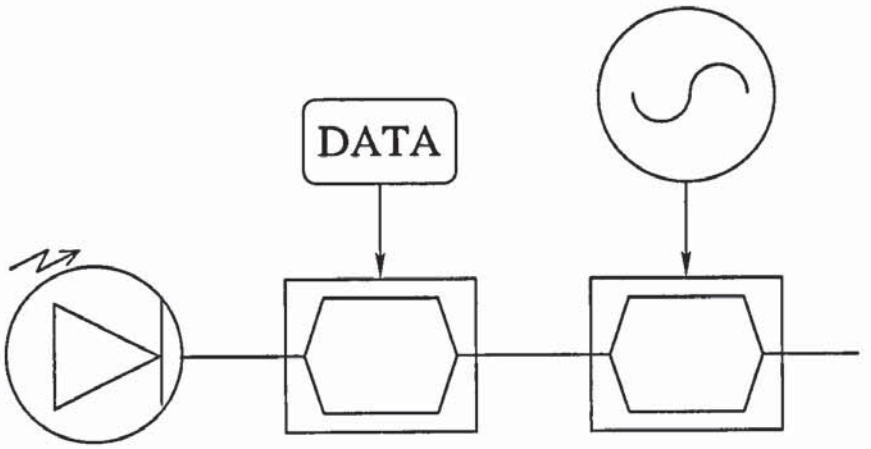

Figure 2.6: RZ-OOK transmitter design based on MZMs.

intensity modulated signal.

Here we will primarily focus on MZM based transmitter designs, due to their versatility and operational characteristics at higher bit rates, over a DML approach.

The transmitter design is presented in figure 2.6. Here a CW laser source is fed into a lithium niobate ($LiNbO_3$) electro-optic modulator arranged in a Marh-Zehnder configuration. Where the MZM is electronically driven by the user's data stream and is biased at 50% transmission, also known as the quadrature point and is driven from minimum to maximum transmission with a voltage swing of V_π. Thus, producing a NRZ-OOK signal. The next stage is to generate a RZ waveform by carving pulses out of the NRZ-OOK signal. This is accomplished by using a modulator known as a pulse carver, which consists of sinusoidally driving the MZM at the data rate between minimum and maximum transmission. The resulting RZ optical pulses have a duty cycle of 50%.

2.7.2 Receiver Design

Direct detection is the typical method used for detecting a RZ-OOK signal. Its configuration is illustrated in figure 2.7. Here the optical field is, first, directly detected by using a photodetector. The electrical signal is then filter by using an appropriate electrical filter. This is then followed by a clock and data recovery (CDR) circuit, which recovers the clock for timing purposes and extracts the data form the signal by using a decision circuit. In essence,

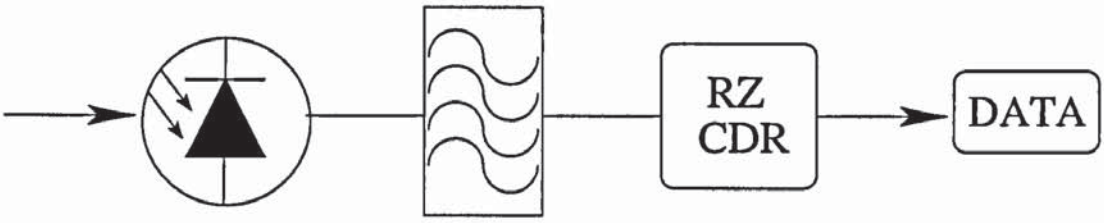

Figure 2.7: Direct detection receiver design.

the decision circuit, decides when the digital signal is a logical "1" or "0". Once the data is extracted the performance of the optical system can be measured by using a BER device, which counts the number of errors occurred during transmission.

2.8 CS-RZ Generation and Detection

An enhanced version of RZ modulation format is known as CS-RZ, which is a pseudo-multilevel format. It differs from RZ in that adjacent bit slots are π out of phase of each other. This simple phase alteration gives the format its name as the carrier at the optical centre of the signal, in the spectral domain, vanishes (see figure 1.4). Data modulated in CS-RZ format are more resilient to fibre nonlinearities, such as IFWM and ghost pulse generation. This is attributed to the π phase inversion between adjacent bits, as optical solitions which are π out of phase of each other, are repelled from one another (as opposed to an attracting interaction), thus reducing optical pulse iteration.

In this section we will show a typical practical implementation of CS-RZ-OOK transmitter and receiver designs.

2.8.1 Transmitter Design

As in section 2.7.1, we will primarily concentrate on CS-RZ-OOK transmitter designs based on MZMs.

Figure 2.8, schematically depicts the CS-RZ-OOK transmitter configuration. As in the case of RZ-OOK, a CW laser source is modulated by a MZM, which is driven by the users data, to produce a NRZ-OOK signal. As before a pulse carver is used to carve the CS-RZ-

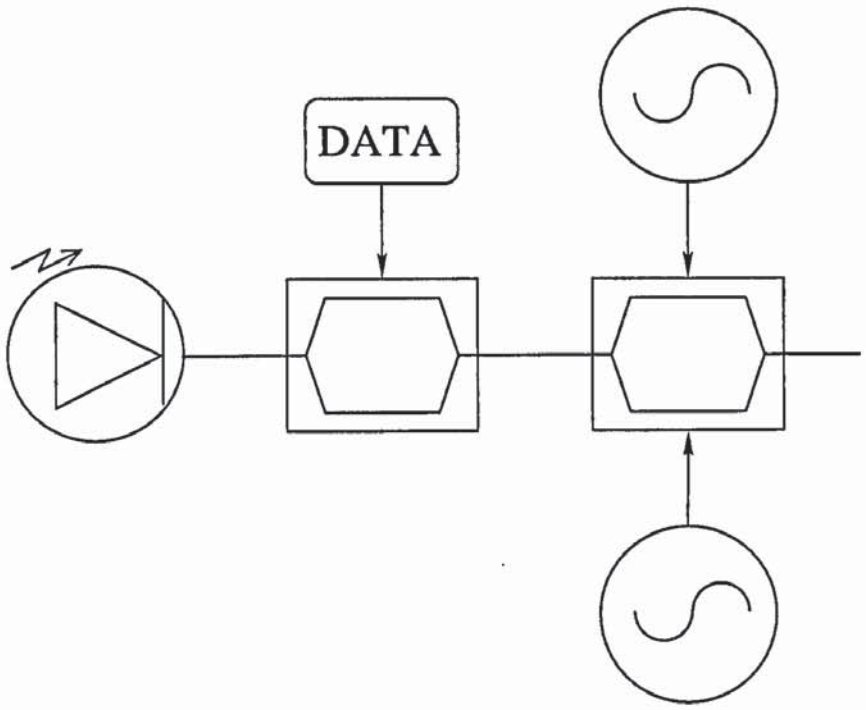

Figure 2.8: CS-RZ-OOK transmitter design based on MZMs.

OOK signal from the NRZ-OOK. Here the MZM arms are driven by the same amount but in opposite directions, i.e. $V_1 = -V_2$. This driving condition is known as balanced driving or push-pull operation. The MZM pulse carver is sinusoidally driven at half the data rate between its transmission maxima. Thus generating a 67% duty cycle RZ pattern with phase inversion between adjacent bit slots (a 67% duty cycle CS-RZ-OOK signal).

2.8.2 Receiver Design

As in RZ-OOK a CS-RZ-OOK signal is detected using square law detection. Note form figure 1.2 (b) the symbol set associated with CS-RZ is $\{-1,0,+1\}$ and the fact that square law detection is the square magnitude of the optical field E, i.e. the optical power $P = |E|^2$. This results in the detector unable to distinguish between the two symbols $E_{1,2} = \pm|E|$, as they both have the same optical power, $P_1 = P_2 = |\pm E|^2$. In effect this automatically maps the symbol set $\{-|E|,0,+|E|\}$ onto the set $\{0,\pm|E|^2\}$. Thus enabling the use of the same receiver design as in RZ-OOK.

The receiver design is described and depicted in section 2.7.2 and figure 2.7 respectively.

2.9 The Principles of VSB and SSB

Vestigial sideband (VSB) and single sideband (SSB) signaling can be applied to some modulation formats in order to suppress half of their spectral content, in an attempt to spectrally pack N data channels into a dense WDM (DWDM) configuration.

The basic principles of this technique is as follows, since the spectrum of real-valued signals are symmetric around the centre of the channel, it is possible to filter out the redundant half of the signal spectrum (as the information is duplicated twice, either side of the central frequency). The signal spectrum can be suppressed, by using ultra narrow filters, in two possible ways. The first is to completely suppress one of the sidebands, this is known as SSB signaling. The second is to apply an optical filter with a gradual roll-off, off the centre of the channel, thus significantly suppressing one of the side bands, while simultaneously preforming some filter action on the other. The later method is known as VSB signaling.

In both WDM and DWDM applications, VSB filtering can be implemented at the transmitter, before the channels are multiplexed, or at the receiver, in demultiplexing process. By applying the VSB filtering at the transmitter, we are able to achieve a significant amount of spectral compression and high spectral efficiency, as channels can be closely packed. In the case of employing VSB filtering at the receiver, would have the action of reducing WDM channel crosstalk for the desired sideband. It is possible to implement VSB filtering at both the transmitter and at the receiver simultaneously in order to benefit from high spectral efficiency and WDM crosstalk suppression.

2.10 RZ-DPSK Generation and Detection

We begin this section, with an introduction to the basic characteristics of RZ-DPSK format, and discuss how to encode a RZ-DPSK signal at the transmitter and then how to decode the transmitted signal at the receiver. We then present a typical configuration of both transmitter and receiver implementations for RZ-DPSK.

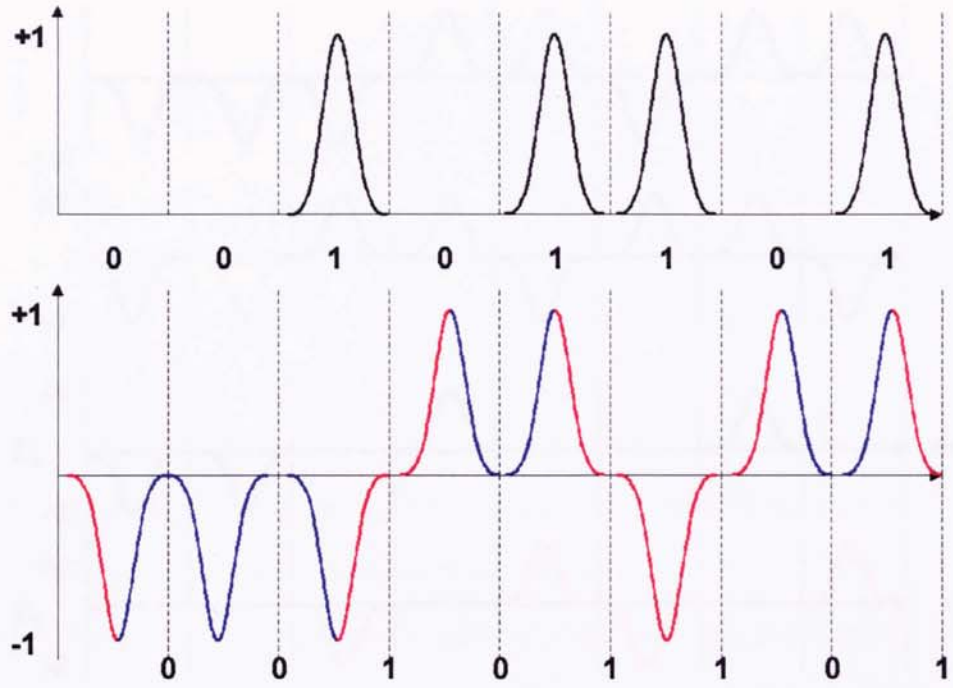

Figure 2.9: Data encoded in OOK format (top). Data encoded in RZ-DPSK (bottom)

2.10.1 Introduction

DPSK is a PSK based modulation format, which unlike its ASK rivals (RZ and CS-RZ), offers to substantively reduce the impact of SPM and XPM on optical pulse propagation. This is due to the constant power associated to each bit slot.

One of the most striking benefits of RZ-DPSK is the ~ 3 dB lower optical-signal-to-noise (OSNR) ratio needed to achieve a given bit-error-rate (BER) performance. This can be demonstrated by considering the quantum limit for an optical pre-amplified receiver, at a BER of 10^{-9}. It has been shown in [63, 64] that 38 photons/bit are required by an OOK signal. However, a RZ-DPSK signal in conjunction with balanced detection, only requires 20 photons/bit, as shown by [64, 65]. Within a practical receiver configuration, 60 photons/bit has been demonstrated by [66], using 10 Gbits/s RZ-OOK. By using RZ-DPSK coupled with an balanced-photo-diode detection scheme, this value was improved to 30 photons/bit [66]. Also at 42.7 Gbits/s a sensitivity of 45 photons/bit has been reported by [67], who also implemented RZ-DPSK. Thus demonstrating approximately 3 dB improvement over the best OOK results.

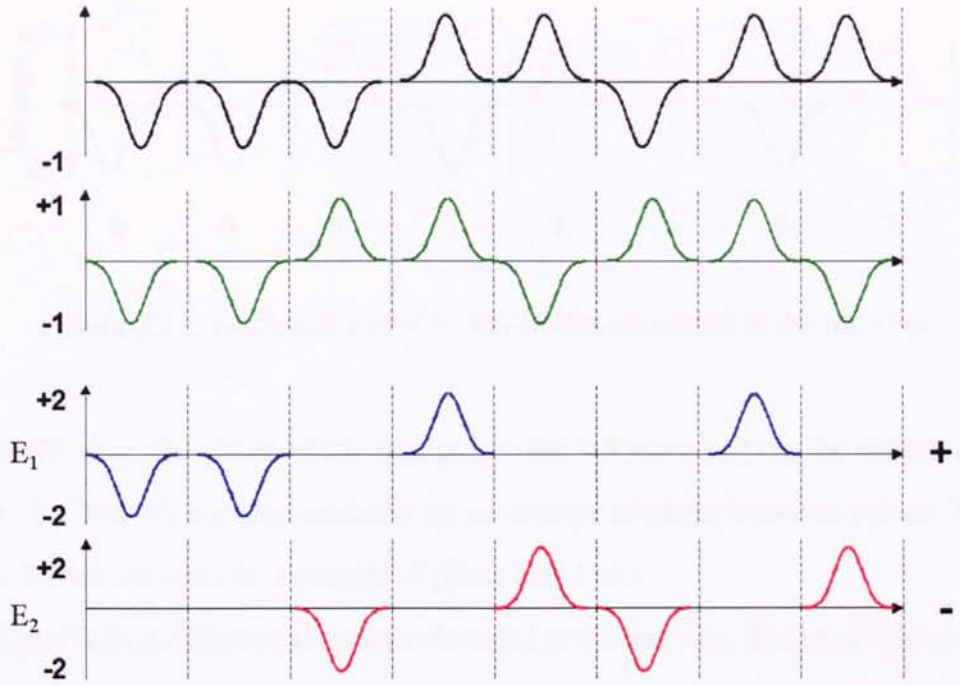

Figure 2.10: Decoding process at the receiver: original signal (top), shifted signal (top middle), black and green added together (bottom middle), black and green subtracted from each other (bottom).

This inherent performance improvement can be more intuitively be observed by considering figure 1.2 (c). Here we note that the symbol separation for DPSK is increased by a factor of $\sqrt{2}$, as compared to RZ-OOK. This increase in symbol distance results in a DPSK signal able accept a $\sqrt{2}$ larger standard deviation of the optical field noise than OOK for equal BER. This translates into a 3 dB reduction of OSNR.

2.10.2 Operational Principles of RZ-DPSK Transmitter and Receiver

In this section we will discuss the function and implementation of the RZ-DPSK format at the transmitter and receiver of an optical lightwave system.

In the OOK modulation format, the data is encoded (at the transmitter) by the presence (denoting a logical 1) and absence (denoting a logical 0) of an optical pulse. However, in RZ-DPSK a single pulse (i.e. a 1) occupies every bit slot and the data is encoded in the change of phase between adjacent pulses Figure (2.9) depicts the inherent differences between RZ-OOK and RZ-DPSK. Here the data *00101101* is encoded in both OOK and RZ-DPSK. In

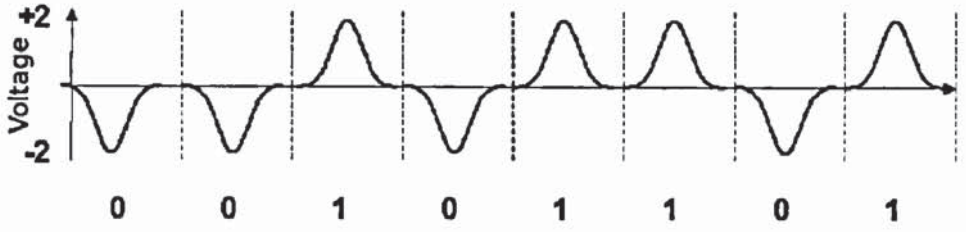

Figure 2.11: Electrical signal of RZ-DPSK produced at the receiver

the RZ-DPSK case, the phase of the first pulse (the left most bit) can be chosen arbitrarily (here it is -1). The *0's* are then encoded by no change of phase between pulses (blue line). While the *1's* are encoded by a change of phase (red line).

The signal is then differentially phase decoded at the receiver. The practical model of the DSPK receiver structure consists of an optical filter, a Mach-Zehnder delay interferometer (MZDI) with differential delay T (equal to the bit period), a balanced photodetector consisting of two photodiodes and a post-detection electrical filter. The task of differentially phase decoding the signal is preformed by the MZDI. The process can be analytically described as follows: if $E(t)$ is the optical field at the input of the MZDI, the signals at the output of the two arms can be written as

$$E_1(t) = \frac{1}{2}\left[E(t)+E(t-T)e^{i\delta\phi}\right] \tag{2.113}$$

$$E_2(t) = \frac{1}{2}\left[E(t)+E(t-T)e^{i\pi}e^{i\delta\phi}\right] \tag{2.114}$$

$$\tag{2.115}$$

where $\delta\phi$ is a phase error, which is zero for optimal reception.

The current is then obtained as

$$I = |E_2(t)|^2 - |E_1(t)|^2 \tag{2.116}$$

The decoding process is illustrated in figures 2.10 and 2.11. The process begins by moving the left most bit into the right most bit slot and shifting the rest of the signal to the left by one, as shown in figure 2.10. The original signal and shifted signal are then added and subtracted from each other (see figure 2.10). Giving us both E_1 and E_2 respectively,

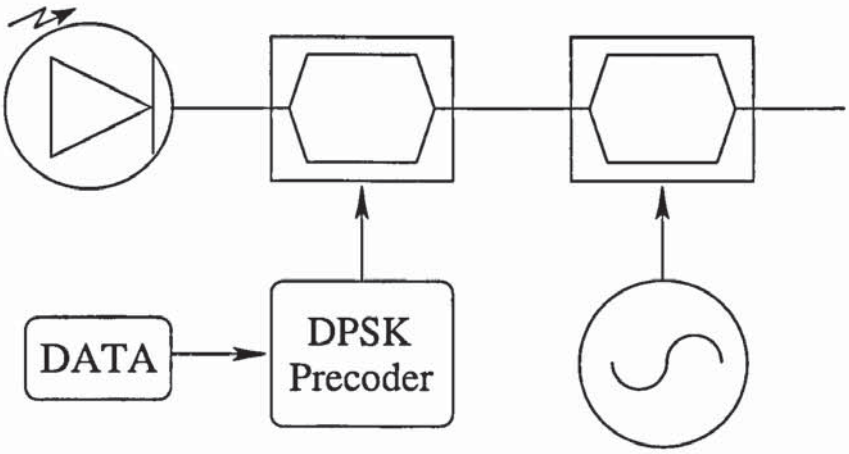

Figure 2.12: RZ-DPSK transmitter based on a phase modulated MZM and a pulse carver.

as indicated by equations 2.113 and 2.114. Finally we apply equation 2.116 and obtain the electrical signal as depicted in figure 2.11.

2.10.3 Transmitter Design

The main differences between RZ-OOK and RZ-DPSK signal generation is of the need to preform optical phase modulation as opposed to intensity modulation and to encode the data into the relative phase changes between adjacent pulses.

Figure 2.12 shows the schematic diagram of a RZ-DPSK transmitter. A CW laser source is modulated by a phase MZM. However, unlike the other formats discussed in the previous sections, the data for a DPSK system is required to be encoded in a different manner, and thus does not directly drive the MZM. Instead a precoder is employed which encodes the data into the change of phase between adjacent pulses. A more detailed operation of the DPSK precoder is presented in section 2.10.2. As with the other modulation transmitter schemes, a sinusoidally driven MZM is then used as a pulse carver to carve the NRZ-DPSK waveform into a RZ-DPSK signal.

2.10.4 Receiver Design with Balanced Detection

Unlike RZ-OOK and CS-RZ-OOK, the transmitted RZ-DPSK signal cannot be directly received by using square law detection. Hence another method is used to extract the data from

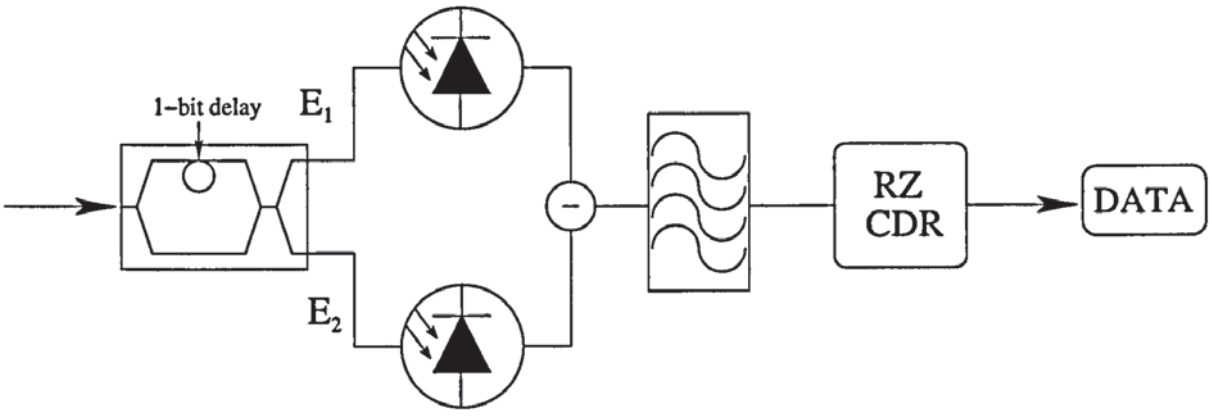

Figure 2.13: RZ-DPSK receiver design with MZDI and balanced detection.

the phase information of the optical signal.

The DPSK receiver structure is illustrated in figure 2.13. First the differential phase modulated data needs to be converted into a intensity modulated format. This is accomplished by the used of a MZDI with a differential delay T (equal to the bit period). This device enables one of the signals, traveling in one of the arms, to experience a delay equal to the bit duration T. Thus enabling the two neighbouring bits to interfere at the output of the MZDI, and produce the two fields E_1 and E_2. The field E_1 consists of the two fields (within the MZDI) interfering destructively whenever there is no phase change and E_2 is the constructive interference which is case when a phase change is present between adjacent bits. The field E_2, however logically inverted, due to energy conservation within the MZDI. By employing balanced detection on fields E_1 and E_2, a 3 dB sensitivity advantage is seen. The balanced photodetector consisting of two photodiodes connected so as to form the difference of fields E_1 and E_2. The superior performance and a detailed quantum mechanical description of the operation of balanced detection can be found in references [49–52]. A post-detection electrical filter is then applied and a RZ-CDR is used to recover the clock and the data is extracted form the signal using the data recovery circuit, which has a decision level set at "0", which is due to the symmetric nature and inherently larger eye opening of the eye diagram associated with DPSK signals.

Chapter 3

DWDM Transmission with Narrow Asymmetric VSB Filtering

In this chapter we will study the effects of narrow, off-centre, optical filtering, known as vestigial side-band (VSB) filtering, applied to RZ-OOK.

Our main objective will be to investigate the impact of the pulse duty cycle on a wavelength allocated transmission at 40Gbit/s with VSB optical filtering. We will also study how the shape of the off-centred VSB filter affects the performance of the optical system.

3.1 Introduction

The development of transmission systems with high channel rates is driven by the possibility of reducing the number of terminals while keeping the same aggregate capacity. In order for 40Gbit/s optical transmission systems to compete with existing 10Gbit/s technologies and be cost effective, it is crucial not only to maintain a large aggregate capacity, but also to provide a high spectral efficiency. Recently, a number of promising approaches have been conceived in order to achieve higher spectral efficiencies at 40Gbit/s rate. It is feasible to obtain a 0.64bit/s/Hz spectral efficiency, by using a specific wavelength allocation scheme combined with VSB filtering, as proposed in [53–55]. With the use of polarisation-division multiplexing (PDM), as prescribed by [56], this spectral efficiency can be further increased

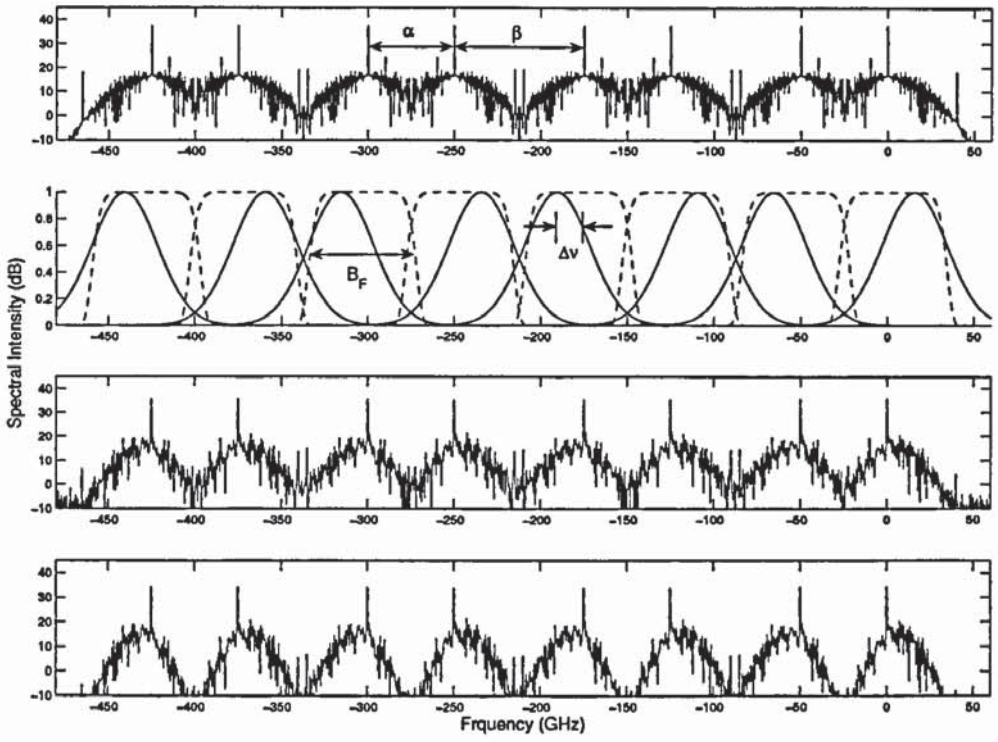

Figure 3.1: Top: Channel spectra before filtering; second from the top: VSB filters (Gaussian - solid, Super Gaussian (SG) - dashed); third from the top: Spectra after filtering; bottom: Spectra after propagation over 300 km of TL/RTL.

to 1.28bit/s/Hz. In this chapter we focus on discussion of the VSB technique only. For a more detailed discussion of VSB signalling/filtering, see section 2.9.

Currently investigations have mostly been focused on the signal reshaping and filtering in the frequency domain. It is obvious, however, that narrow filtering is made at the expense of increasing non-linear penalties due to narrower channel spacing and an inherent back-to-back waveform distortion. Therefore, further performance improvement can be gained by optimising simultaneously the spectral domain filtering and carrier pulse characteristics in the temporal domain.

Extending the results obtained in [53, 54], we investigate the impact of the duty cycle on a wavelength allocation scheme with ultra-narrow, off-centre, optical filtering to multiplex/demultiplex WDM channels at 40Gbit/s rate. We also examine how the shape of the off-centred VSB filter affects the performance of the optical system.

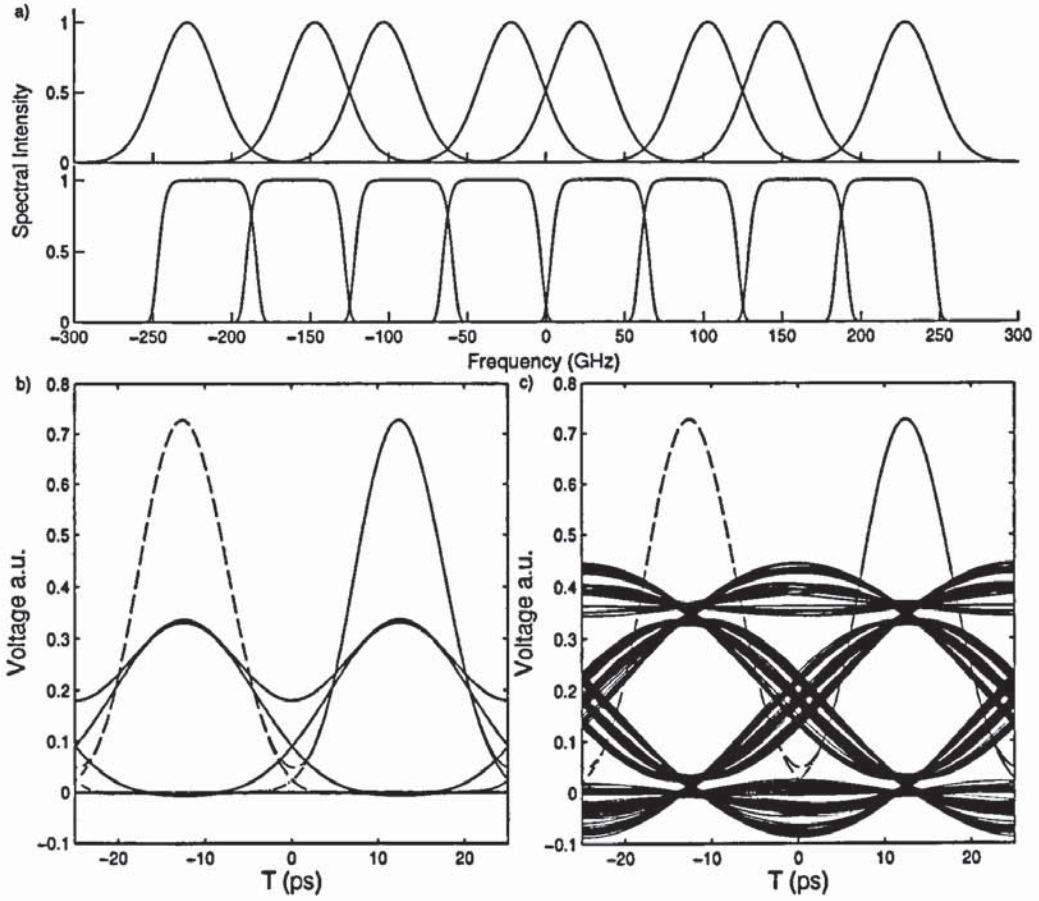

Figure 3.2: Effect of VSB filtering on Gaussian pulses. a) Top, narrow off centred Gaussian filters and bottom, narrow off centred Super Gaussian filters. b) Eye diagram of the signal before and after the application of a Gaussian filter. Dashed line, signal before filtering, solid line, filtered signal. c) Eye diagram of the signal before and after the application of a Super Gaussian filter. Dashed line, signal before filtering, solid line, filtered signal.

3.2 Frequency Allocation and VSB Off-Centre Filtering

In the numerical modelling, we have implemented the frequency allocation scheme first proposed by Bigo and Frignac [53]. Contrary to standard periodic frequency grid, here the channels are grouped into pairs, with an alternating frequency separation. The two channels, within the pair, are separated by α [GHz]. The pairs are then spaced by β [GHz] as illustrated in figure 3.1. Therefore, $(\alpha+\beta)/2$ gives the channel spacing for the corresponding standard WDM transmission occupying the same bandwidth. To achieve 5Tbit/s capacity over C and L bands (8THz total bandwidth), the condition $\alpha+\beta = 125$ GHz has to be satisfied [53]. It

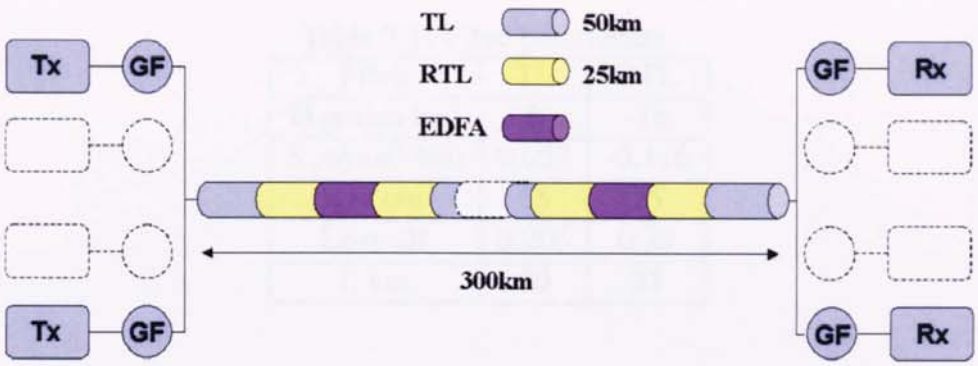

Figure 3.3: Diagram of lightwave system

has been previously shown in [53], that channel allocation $\alpha/\beta = 50$ GHz$/75$ GHz leads to better performance than the standard periodic channel spacing with $\alpha = \beta = 62.5$ GHz.

The aim of VSB filtering is to reshape the channel spectra, in an attempt to isolate one of the side bands and reduce crosstalk between adjacent channels. Detuning the narrow pass-band filter off the carrier enhances the favoured side-band, while making efficient reduction of crosstalk. The detuning is always done away from the centre of a pair of closely spaced channels. Thus, the side-band having the smallest overlap with adjacent channels is isolated while the impact of the crosstalk affecting the other side-band is minimised [53]. The best performance is a complex trade-off between crosstalk suppression and waveform distortion, leading to propagation penalties. Here we recognise that the important system parameters to be optimised in this scheme are the following: optical filter bandwidth, filter detuning and duty cycle.

The VSB off-centre filtering has been employed at both the transmitter and at the receiver, in order to suppress crosstalk during transmission. The scheme of the frequency allocation and VSB Gaussian filtering detuned off the centre frequency of the channel by $\Delta\nu$ is shown in figure 3.1.

It is a common belief that the performance of MUX/DEMUX device is better if the filter has a sharper profile and is believed to be more efficient in crosstalk suppression. Note that the VSB filter function is not only to isolate some part of the spectrum, but also to minimise waveform distortion. Therefore, the shape of the VSB filter plays an important role and the

Table 3.1: Fibre parameters.

Fibre	TL	RTL
D ps/(nm km)	8	-16
S ps/(nm^2 km)	0.057	-0.116
A_{eff} μm^2	65	25
Loss dB	0.205	0.28
L km	50	25

results of optimisation can directly depend on the filter form. We investigate how the shape of the optical filter effects the performance by considering both Gaussian and sharper, Super-Gaussian filter (SG) profiles. We constructed the optical filters numerically by the use of the transfer function Eq. 3.1.

$$f(\nu) = exp\left(-\frac{(\nu-\nu_0)^m}{B_F^m}\right) \tag{3.1}$$

The Super-Gaussian filter used in this investigation was of order m=10. Figure 3.2(a) depicts the arrangement used for both Gaussian and Super Gaussian filters. The eye-diagram in figure 3.2(b) shows the effect of applying a narrow Gaussian filter to a RZ-OOK signal. Also the effect of applying a Super Gaussian filter to a RZ-OOK is presented in 3.2(c).

3.3 System Set-Up and Results

The dispersion map consists of 50km of TeraLight (TL) fibre and 25km Reverse TeraLight (RTL) fibre followed by an EDFA (noise figure = 4.5 dB) and a similar block with the reverse order of TL and RTL. The fibre parameters are presented in the table 3.1.

Using Eq. (3.2), we constructed the dispersion map such that the span average dispersion is zero. The map was designed to be symmetric, so that we were able to launch the signal at the chip free point.

$$\langle\beta_2\rangle = \frac{\beta_{2,1}L_1 + \beta_{2,2}L_2}{L_1 + L_2} \tag{3.2}$$

Total transmission distance was 300 km. The system design is depicted in figure 3.3. Transmission of eight WDM channels (8×40Gbit/s) spaced using $\alpha = 50$GHz and $\beta =$

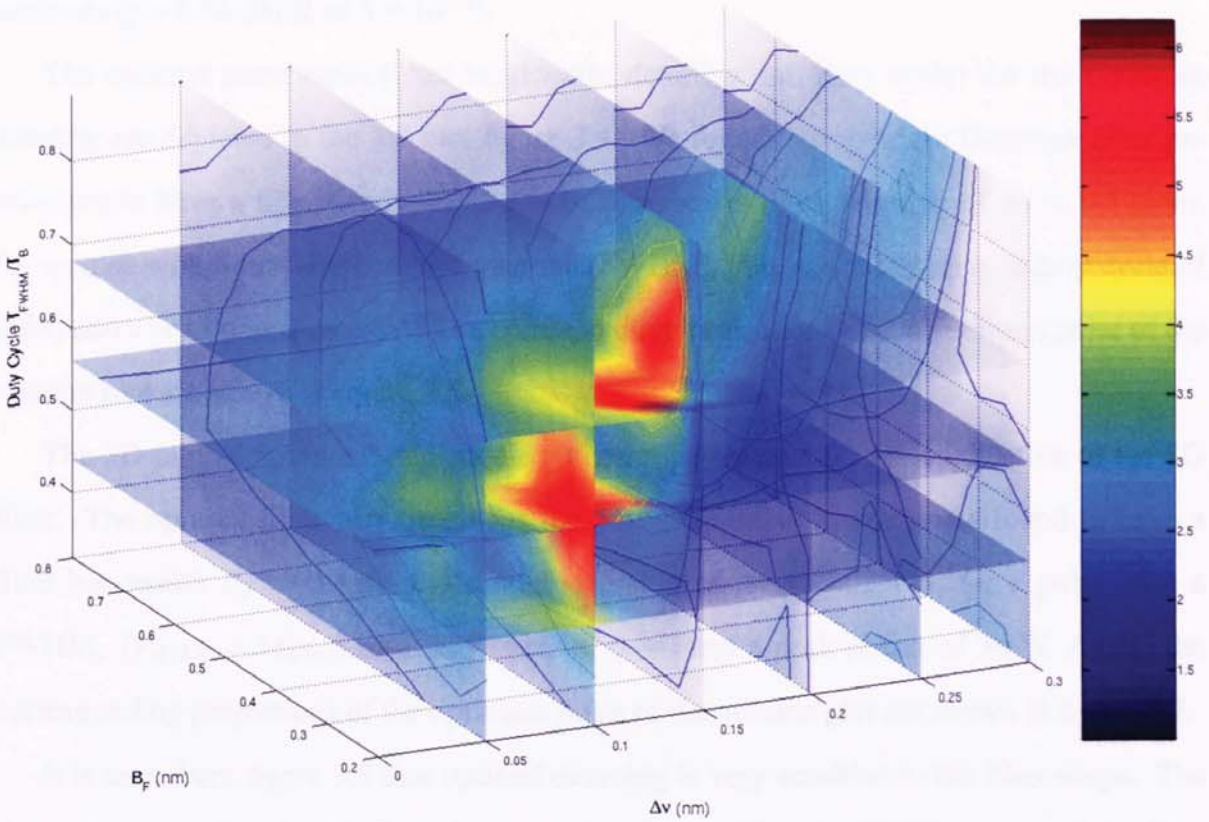

Figure 3.4: 3D volume plot of optimum system parameters for Gaussian Filter.

75GHz has been modelled using $2^7 - 1$ pseudo-random binary sequence data signal. A VSB filter has been realized at the multiplexer (MUX), in order to obtain a high spectral efficiency and at the demultiplexer (DEMUX), in an attempt to reduce crosstalk.

We numerically simulated the system by using the split-step Fourier method, as outlined in Appendix A. We measured the performance of the transmitted signal by calculating the BER through the statistical variations of the ones and zeros of the received electrical signal, see Appendix B for details and the analytical relation of the Q-factor with BER.

To account for statistical fluctuations 26 numerical runs were performed and the mean value of the Q-factor has been taken for each point near the best operational regime.

Both for the Gaussian and SG filters we found that, the maximum Q-factor is at a duty cycle value of 0.64. This optimum duty cycle improves performance by 1 dB for Gaussian filters and by 3dB for SG filters, when compared to a duty cycle of 0.5. We found that the Gaussian filter at the best point gives a Q = 6.2 (BER of 2×10^{-10}) while the SG filter

achieves $Q = 5.78$ (BER of 4×10^{-9}).

The optimal parameters (filter bandwidth, detuning and duty cycle) for the Gaussian filtering are depicted in the 3D plot figure 3.4. We found the optimum Gaussian filter parameters to have a filter bandwidth $B_F = 0.25$nm and a filter detuning of $\Delta\nu = 0.125$nm, for a pulse with a full width at half maxima (FWHM), $T_{FWHM} = 16$ps (i.e. a duty cycle of 0.64) and a peak power of 3mW. The corresponding projections of the optimum point of the volume plot are shown in figure 3.5.

The 3D plot of figure 3.6 depicts the optimum parameters for the application of the SG filter. The optimal filter parameters for the Super Gaussian filtering was found to have a filter bandwidth $B_F = 0.3$nm and a filter detuning of $\Delta\nu = 0.025$nm, for a pulse with a FWHM, $T_{FWHM} = 16$ps (i.e. a duty cycle of 0.64) and a peak power of 3mW. Again, the corresponding projections of the optimum point of the volume plot are shown in figure 3.7.

It is seen from figure 3.8 that optimal detuning is very sensitive to the filter shape. The more abrupt profile of a SG filter does not allow to significantly shift the centre of the filter away from the carrier. The Gaussian filter is more flexible and displays better performance in simultaneous side band isolation and minimisation of the cross-talks, which results in better performance and a higher Q-factor value.

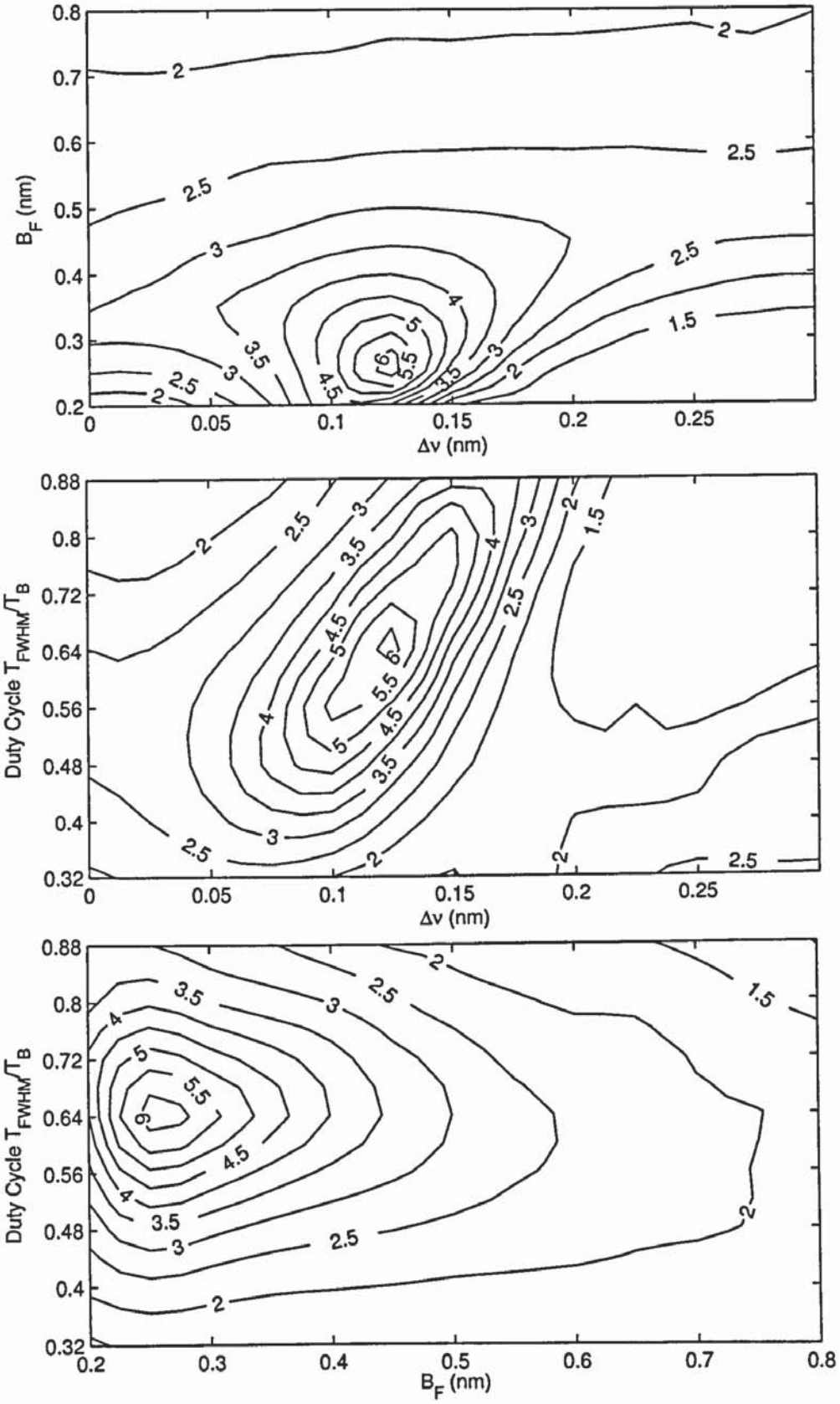

Figure 3.5: Three corresponding projections for Gaussian filter. Top, filter bandwidth vs filter detuning. Middle, duty cycle vs filter detuning. Bottom, duty cycle vs filter bandwidth.

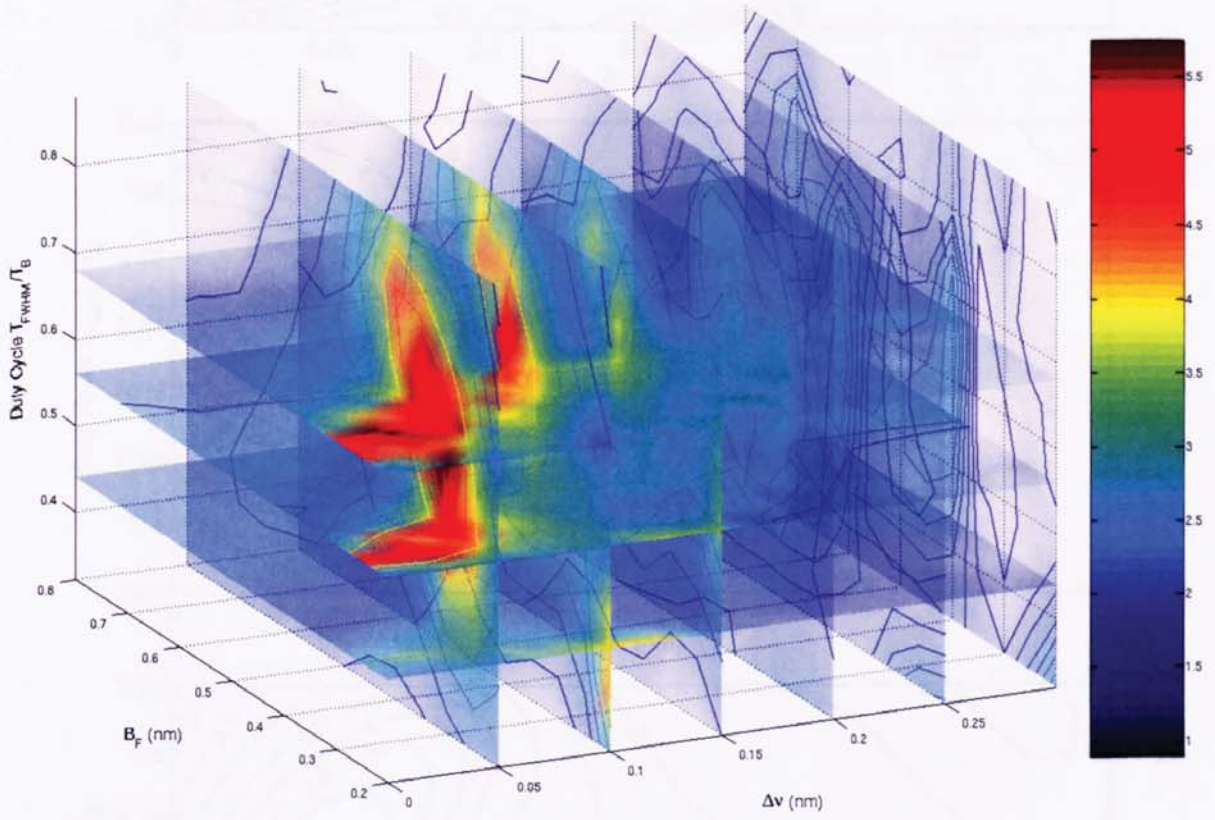

Figure 3.6: 3D volume plot of optimum system parameters for SG filter.

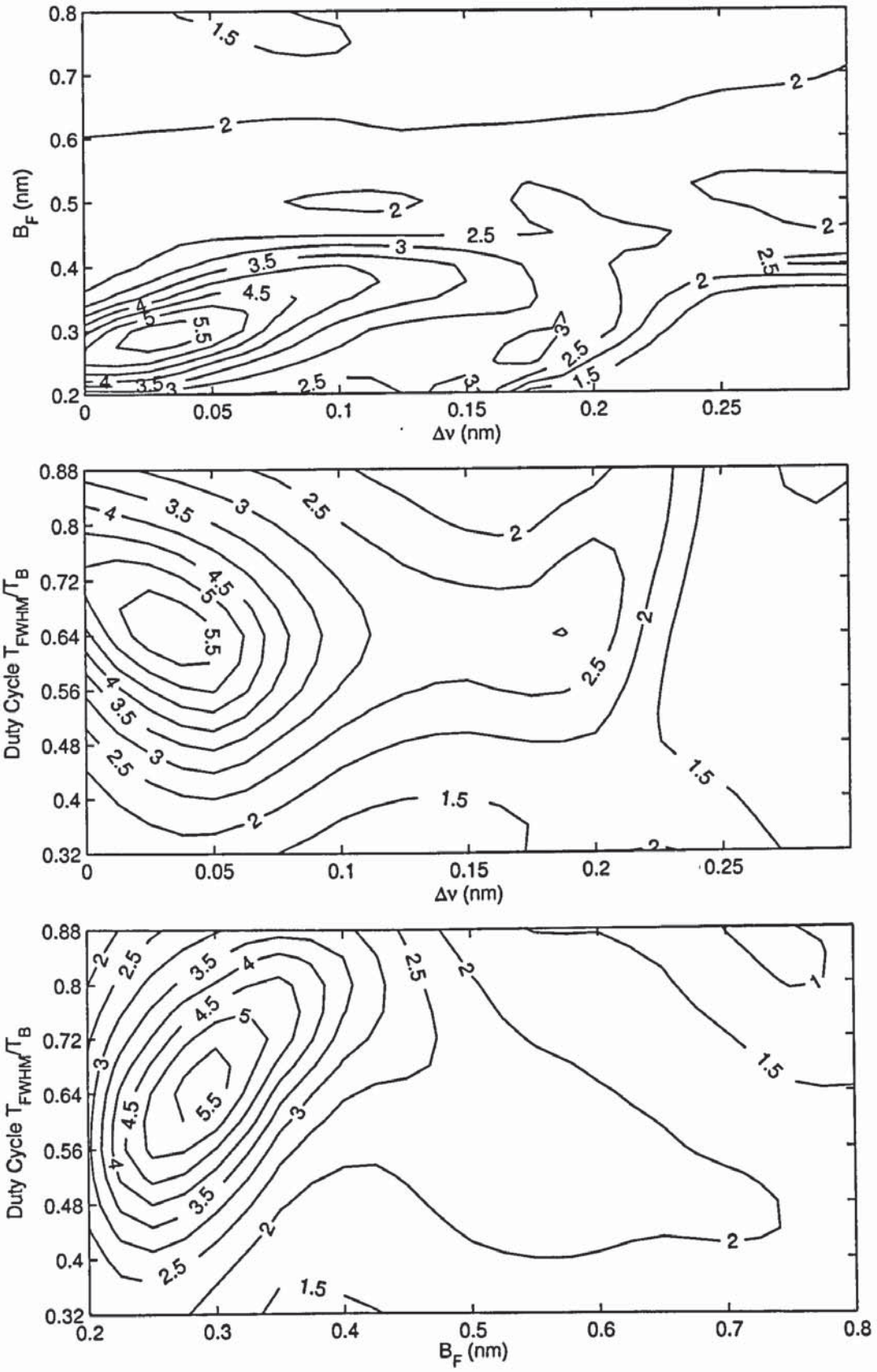

Figure 3.7: Three corresponding projections for SG filter. Top, filter bandwidth vs filter detuning. Middle, duty cycle vs filter detuning. Bottom, duty cycle vs filter bandwidth.

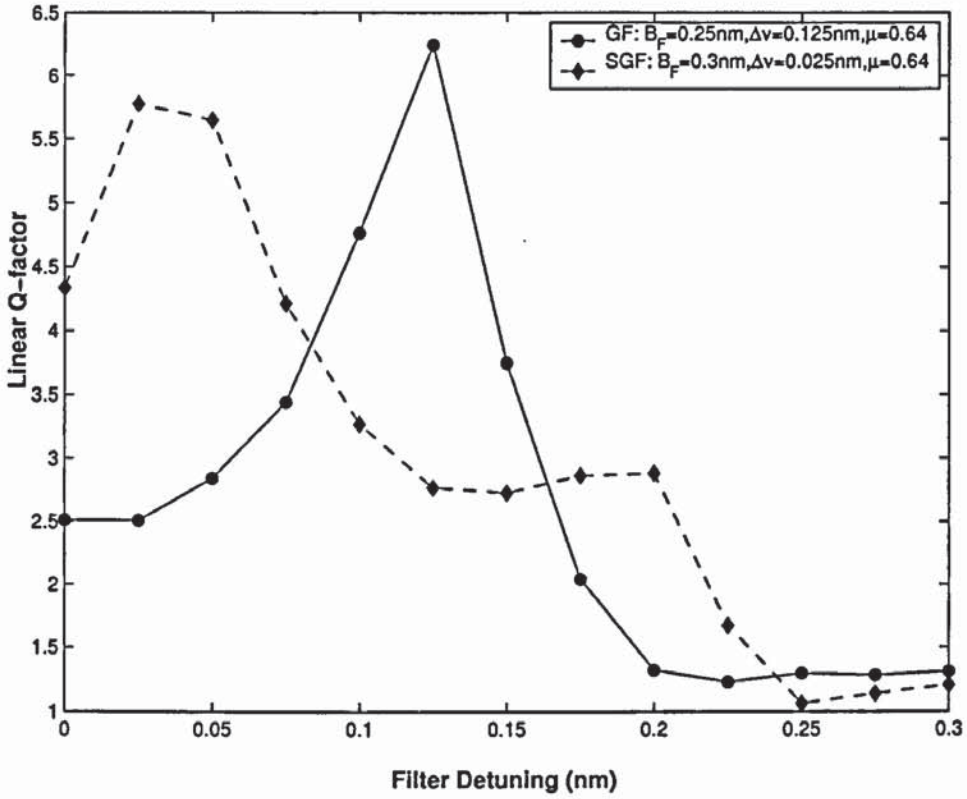

Figure 3.8: Linear Q-factor versus filter detuning. Solid line - Gaussian filter; dashed line - SG filter.

3.4 Conclusions

In this chapter we preformed various numerical simulations with the aim of investigating the effects of ultra narrow VSB filter on a $N\times 40$Gbit/s RZ-OOK fibre optic transmission system. We were particularly interested in achieving a high spectral efficiency of 0.64bit/s/Hz.

We designed a DWDM fibre optic transmission system with a symmetric dispersion map and an amplifier separation of 75km. We adopted a frequency allocation scheme where the optical channels were grouped into pairs, with their inner sidebands overlapping. We employed the use of VSB filtering (before the channels were multiplex), in order to achieve significant spectral compression and a high spectral efficiency of 0.64bit/s/Hz. VSB filtering were also implemented in the demultiplexing process in order to reduce crosstalk and increase receiver performance.

In our numerical simulations we simultaneously optimised both spectral domain filtering and carrier pulse characteristics in the temporal domain, in an attempt to improve on previous VSB investigations. In essence we considered the following parameters in our investigation: the filter shape (both Gaussian and Super Gaussian filters), the filter bandwidth, the detuning of the filter, the duty cycle of the carrier pulse and the peak power.

We have numerically demonstrated that by preforming a duty cycle optimisation in conjunction with spectral domain optimisations we were able to further optimise system performance. By using an optimum duty cycle of 0.64bit/s/Hz, as opposed to 0.5bit/s/Hz, we found a 1dB improvement in system performance when using Gaussian VSB filters and a 3dB improvement when using SG VSB filters.

We achieved a transmission distance of 300km using a DWDM $N\times 40$Gbit/s RZ-OOK at a spectral efficiency of 0.64bit/s/Hz.

We have found that a Gaussian filter based MUX/DEMUX performs better at VSB functions when compared to SG filter.

Chapter 4

DWDM CS-RZ Transmission with Narrow Asymmetric VSB Filtering

In this chapter we begin our analysis of the CS-RZ modulation format.

Here we aim to examine the correlations between the parameters of ultra-narrow off-centred filtering and pulse width on the performance of a wavelength paired Nx40Gbit/s DWDM transmission, consisting of CS-RZ signal with 0.64 bit/s/Hz (without polarization-division multiplexing (PDM)) spectral efficiency.

4.1 Introduction

In the previous chapter we utilised the OOK modulation format. However, another important approach in increasing spectral efficiency is using the CS-RZ modulation format. It enables the highest spectral efficiency among the other OOK formats [57–60].

The fundamental difference between the generation of a CS-RZ signal compared to OOK signal, is the alternating phase between adjacent pulses. Figure 4.1 represents the real part of the complex field for both RZ-OOK and CS-RZ. It can be see from figure 4.1 that the periodic nature of the phase correlation between adjacent pulses (in this case the phase is rotated from $\phi = 0$ to $\phi = \pi$), as opposed to the RZ-OOK signal, which has a constant phase (in this case a constant phase of, $\phi = 0$). Consult section 1.2.3, for more details.

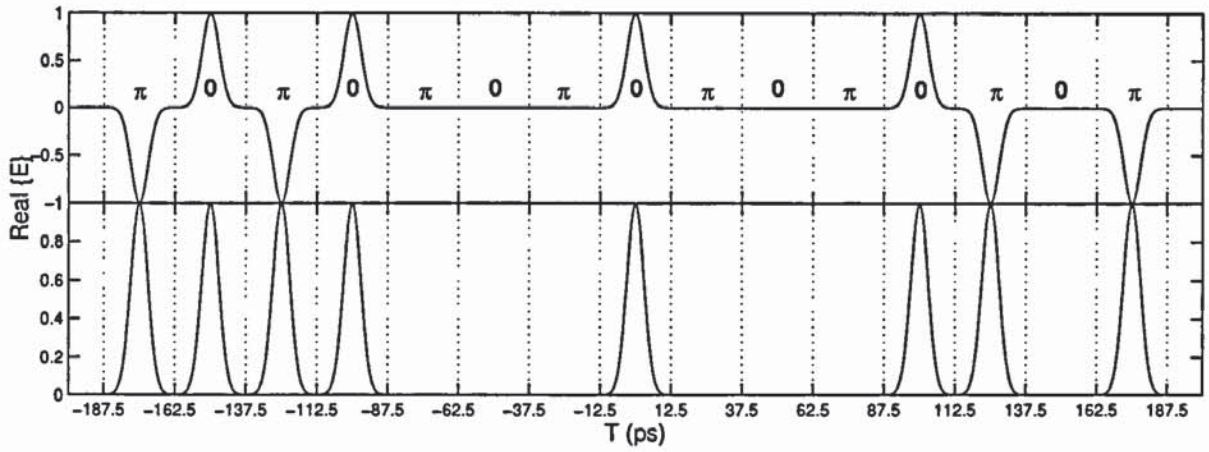

Figure 4.1: Temporal domain comparison of both CS-RZ (top) and RZ-OOK (bottom).

By examining the spectral domain of an CS-RZ and RZ-OOK signal, we can observe another fundamental difference between the two formats. Examining figure 4.2 we note the lack of a central carrier on each of the channels for a CS-RZ signal.

As in Chapter 3, the application of ultra-narrow filtering to systems using the CS-RZ modulation format is done at the expense of increasing non-linear penalties due to narrower channel spacing and an inherent temporal waveform distortion. Therefore, for any particular system it is important to find an optimum between the performance improvement gained by optimisation of the spectral domain filtering and determination of superior carrier pulse characteristics in the temporal domain.

Here we focus on the optimisation of ultra-narrow VSB filtering technique in application to the CS-RZ modulation format. As in the previous chapter, we generalise the results obtained in [53, 54]. We simultaneously optimise the signal pulse width and parameters of ultra-narrow off-centered VSB filtering without the use of PDM.

4.2 Wavelength Allocation and VSB Off-Centre Filtering

Though our approach is rather general, for the sake of clarity, we focus here on a particular example of a wavelength-paired Nx40Gbit/s DWDM transmission scheme with ultra-narrow,

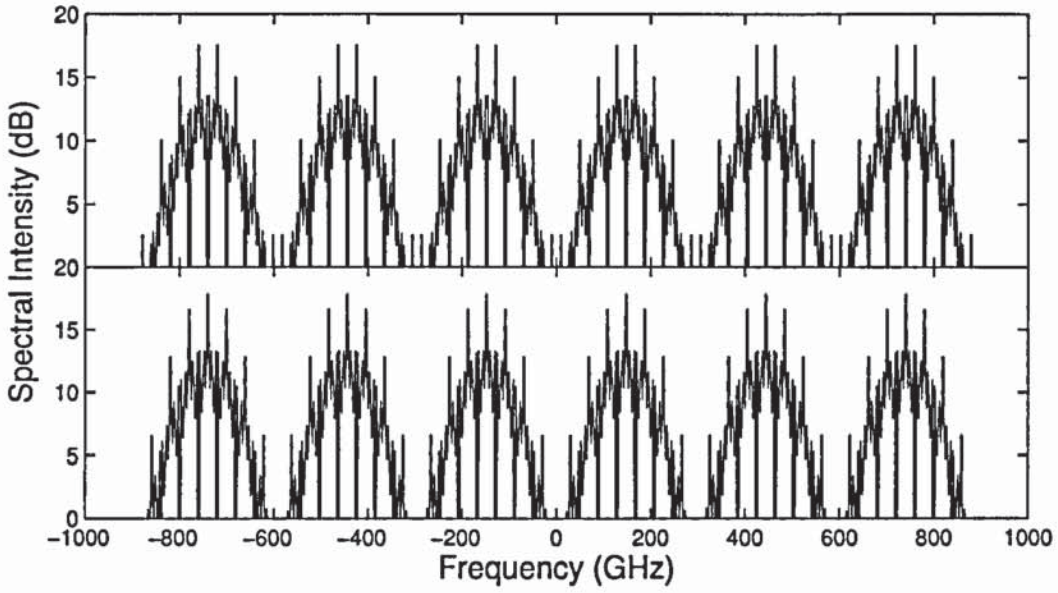

Figure 4.2: Spectral domain comparison of both CS-RZ (top) and OOK (bottom).

off-centre optical VSB filtering.

The wavelength allocation scheme described in the previous chapter is applied to CS-RZ modulation format. As we have seen, the aim of VSB filtering is to reshape the channel spectra, in an attempt to isolate one of the two single sidebands (SSBs) and further reduce crosstalk between adjacent channels. This approach makes use of either upper sideband (USB) or lower sideband (LSB) of adjacent channels [57]. Detuning the narrow passband filter off the carrier enhances the favoured sideband, while making efficient reduction of crosstalk. As before the detuning is always done away from the centre of a pair of closely spaced channels. Using this technique we find the sideband having the smallest overlap with adjacent channels is confined while the impact of the crosstalk affecting the other sideband is minimised [53, 57]. We find the resulting best performance is a rather complex trade-off between crosstalk suppression and waveform distortion.

Therefore, important system parameters to be optimised in this scheme are: optical filter bandwidth, filter detuning and duty cycle. Our goal is to find the optimal correlations between the impact of ultra-narrow off-centred VSB filtering and the duty cycle parameter on

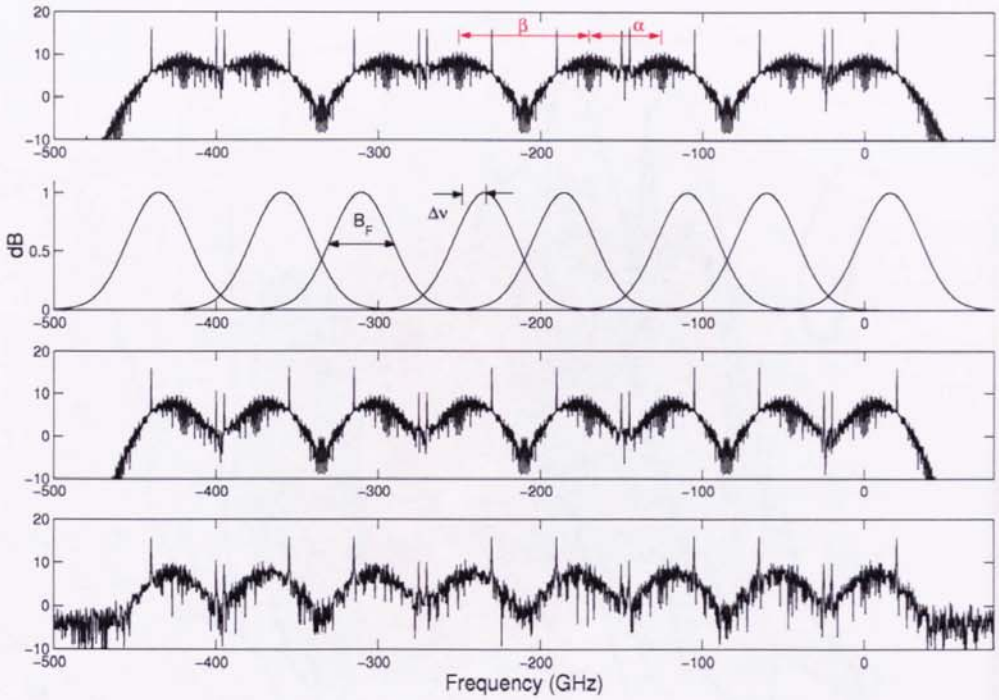

Figure 4.3: Channel spectra of CS-RZ signal before filtering (top); VSB filters (second from the top); Spectra after filtering (third from the top); Spectra after propagation over 650 km of TL/RTL (bottom).

the performance of a specific optical fibre line, as described in the next section.

4.3 System Design and Results

Without loss of generality, we now examine a particular fibre transmission link. The VSB off-centre filtering has been employed at both the transmitter and at the receiver, in order to suppress crosstalk during transmission. The scheme of the frequency allocation and VSB Gaussian filtering detuned off the centre frequency of the channel by $\Delta\nu$ is shown in figure 4.3.

We use a similar transmission system to that used in Chapter 3. Which consists of a CS-RZ transmitter, followed by a Gaussian VSB filter before the MUX and N spans of a symmetric dispersion map, which is constructed of 50km of TL fibre and 25km of RTL fibre followed by an EDFA (noise figure = 4.5 dB) and a similar block with the reverse order of

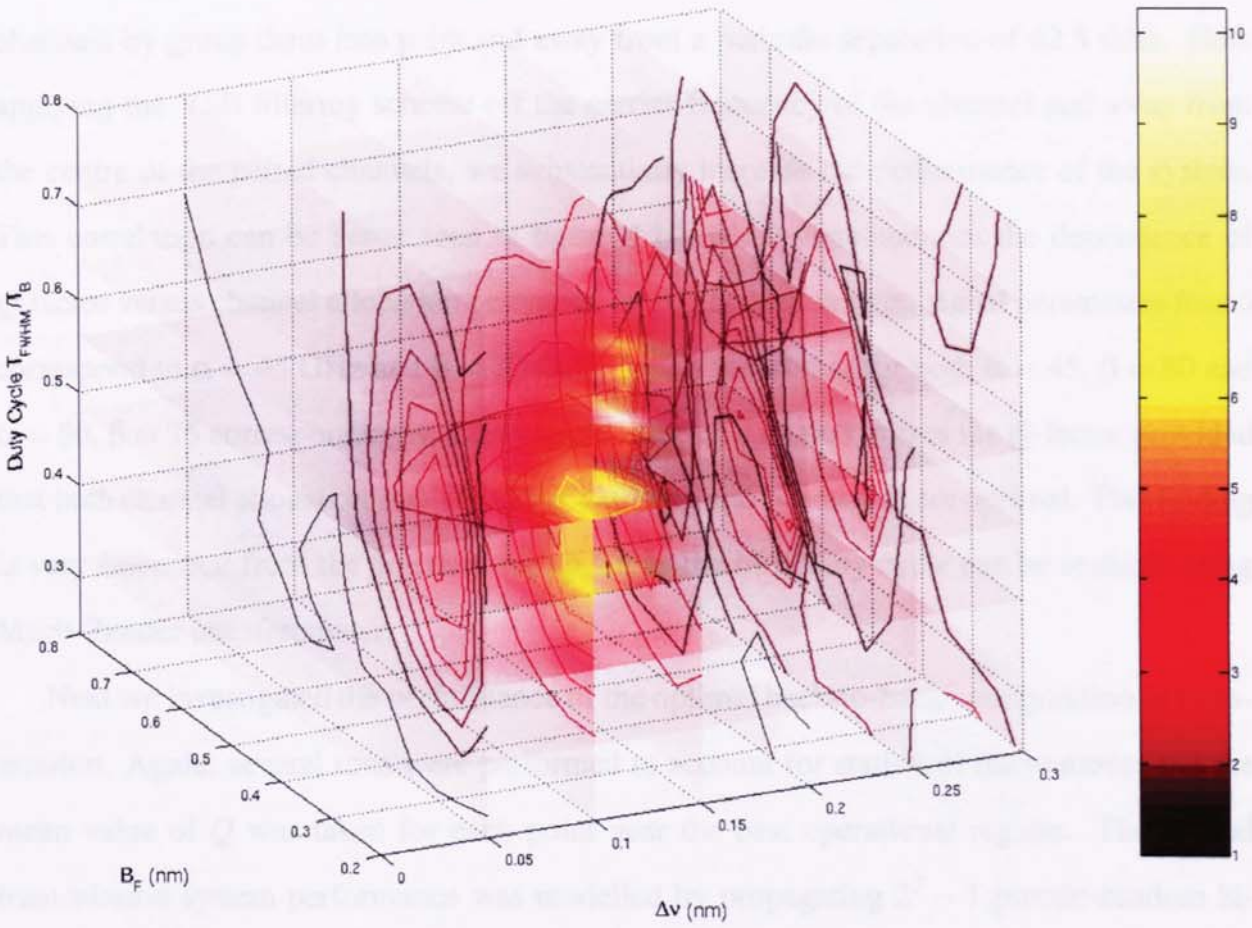

Figure 4.4: 3D volume plot of optimum system parameters for $\alpha = 45$ GHz and $\beta = 80$ GHz.

TL and RTL. The dispersion map was chosen so that the span average dispersion is zero, this was accomplished by applying equation 3.2. By ensuring the map to be symmetric, we were able to launch the signal at the chip free point, of the transmission line. The span length of the map was fixed at $L = 75$km, as typical values used in many experiments/commercial designs, are in the region of $L = 50\text{km} \rightarrow 100\text{km}$. Finally, a Gaussian VSB filter was realised at the receiver in the DEMUX process.

First, the best system parameters were determined for eight WDM channels (8x40Gbit/s) in back-to-back performance. At least five numerical runs were performed for each set of parameters to account for pattern dependences.

Figures 4.4, 4.5, 4.6, 4.7, 4.8 and 4.9 illustrate the performance in terms of Q-factor versus three optimisation parameters (filter bandwidth, detuning and duty cycle) for some

ratios of α/β. We can see from these figures, that we overlap the inner sidebands of the channels by group them into pairs and away from a periodic separation of 62.5 GHz. Now applying the VSB filtering scheme off the carrier frequency of the channel and away from the centre of the paired channels, we substantially increase the performance of the system. This correlation can be better seen in figure 4.10, which demonstrates the dependence of Q-factor versus channel allocation parameter α/β. The best system/signal parameters found correspond to $\alpha = 45$ GHz and $\beta = 80$ GHz. It was found that for both $\alpha = 45$, $\beta = 80$ and $\alpha = 50$, $\beta = 75$ correspondingly, a duty cycle value of 0.64 maximizes the Q-factor provided that both channel allocation and VSB filter detuning and bandwidth are optimal. This finding is very important from the practical viewpoint as the 66% duty cycle can be realized using Mach-Zender interferometer.

Next we investigated the performance of the optimal back-to-back configuration in transmission. Again, several runs were performed to account for statistical fluctuations, and the mean value of Q was taken for each point near the best operational regime. The optical transmission system performance was modelled by propagating $2^7 - 1$ pseudo-random binary sequence CS-RZ signal. The error-free transmission distance was defined using the standard definition of the Q-factor based on Gaussian statistics (see Appendix B for details). In this case a linear Q-factor of 6 is equivalent to a BER of 10^{-9}. The input signal power, duty cycle and span average dispersion have been optimised to maximize transmission distance.

Figure 4.11 demonstrates the effect of duty cycle on transmission propagation. It confirms that, indeed, a right choice of temporal pulse characteristics is important for the realisation of optimal narrow filtering.

Finally in figure 4.12, we further investigated the properties of the system by optimising the average dispersion of the map. We found, in this system, that a close to zero average dispersion of the map and a peak power of 6dB provides optimum transmission characteristics.

4.4 Conclusions

We have continued our analysis of VSB filtering on DWDM applications and have preformed large scale numerical simulations. Here we investigated the effects of VSB filtering on CS-RZ modulation format, which was applied to the same the same optic fibre transmission system as describe in the previous chapter. Again we adopted the same frequency allocation scheme.

The numerical simulations were preformed, such that, we were able to simultaneously optimise both carrier pulse characteristics and spectral domain filter parameters. We also investigated the ratio α/β for CS-RZ data channels. As our parameter space had become significantly larger, we adopted a new optimisation strategy, where we now optimised some of the parameters (namely the filter bandwidth, the filter detuning and the duty cycle) in back-to-back simulations, which decreased our computational overhead.

We found the CS-RZ modulation format to be more tolerant to spectral overlapping as the optimum performance of the system was found at $\alpha = 45$ and $\beta = 80$, as opposed to $\alpha = 50$ and $\beta = 75$ for RZ-OOK.

A feasibility of $N \times 40$ Gbit/s DWDM transmission of CS-RZ signal well over 500 km with 0.64 bit/s/Hz spectral efficiency, without using PDM, has been confirmed by numerical modelling. We have demonstrated that the selection of an optimal duty cycle close to 0.6 can improve the system performance without decreasing the spectral efficiency. By implementing the CS-RZ modulation format into the VSB signalling scheme, we were able to approximately double our system performance, when compared to RZ-OOK, which was investigated in the previous chapter.

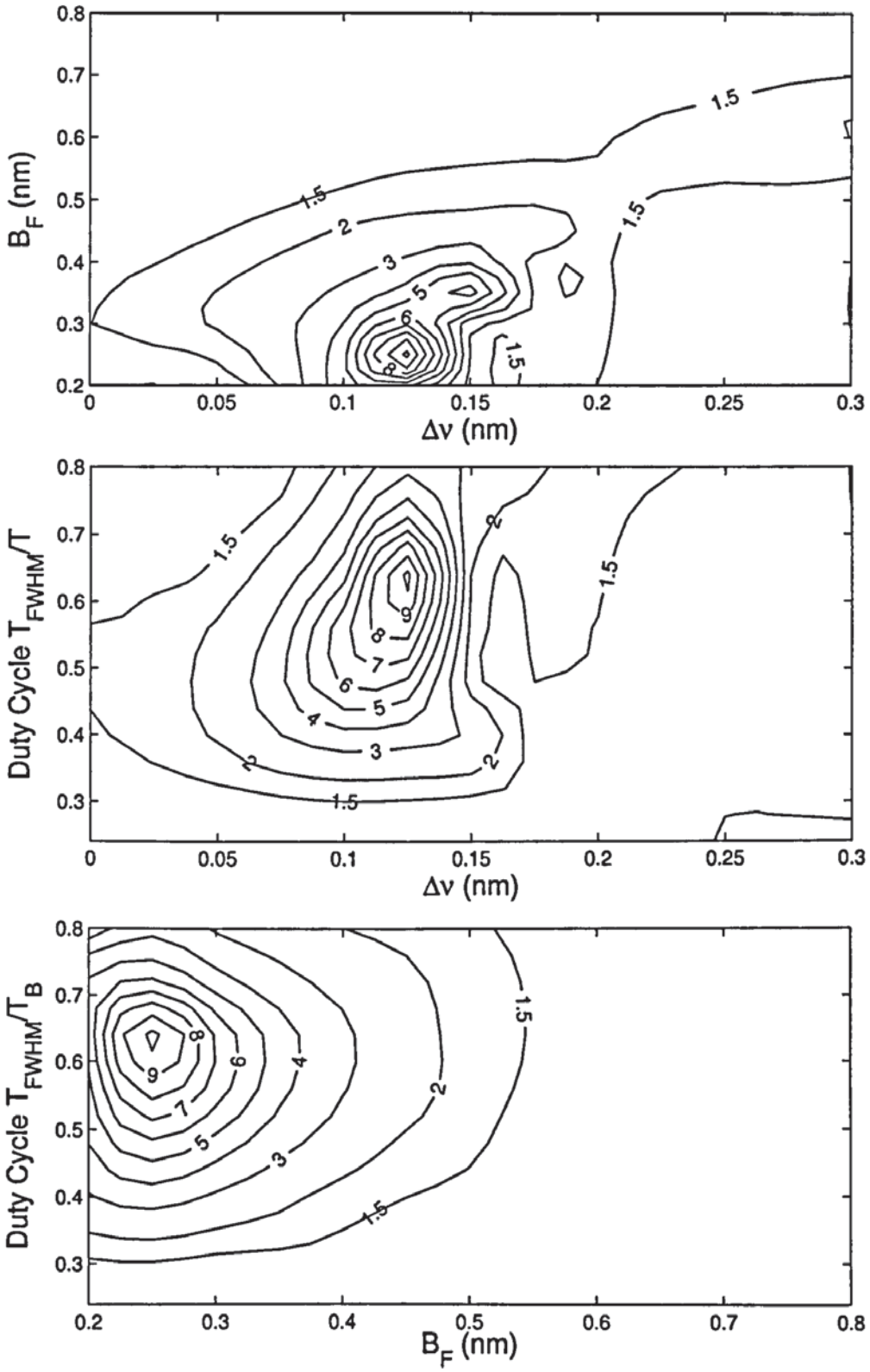

Figure 4.5: Three corresponding projections for $\alpha = 45$ GHz and $\beta = 80$ GHz. Top, filter bandwidth vs filter detuning. Middle, duty cycle vs filter detuning. Bottom, duty cycle vs filter bandwidth.

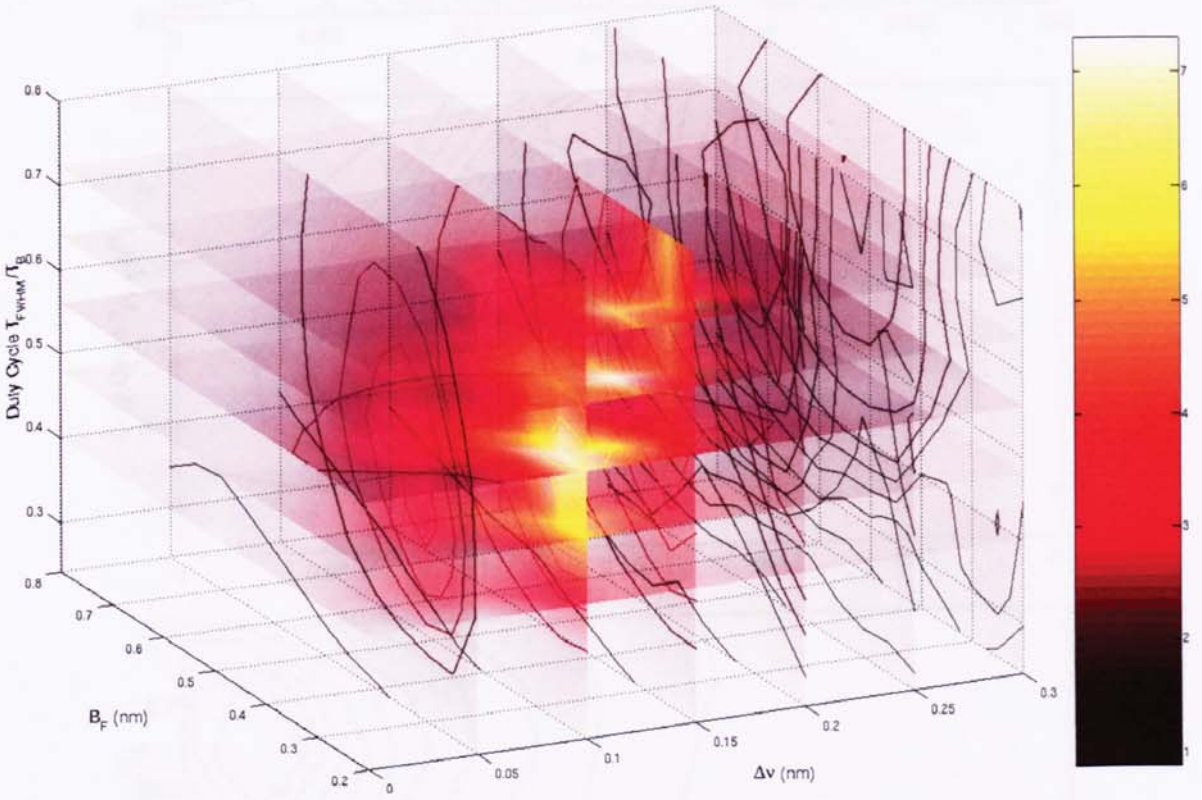

Figure 4.6: 3D volume plot of optimum system parameters for $\alpha = 50$ GHz and $\beta = 75$ GHz.

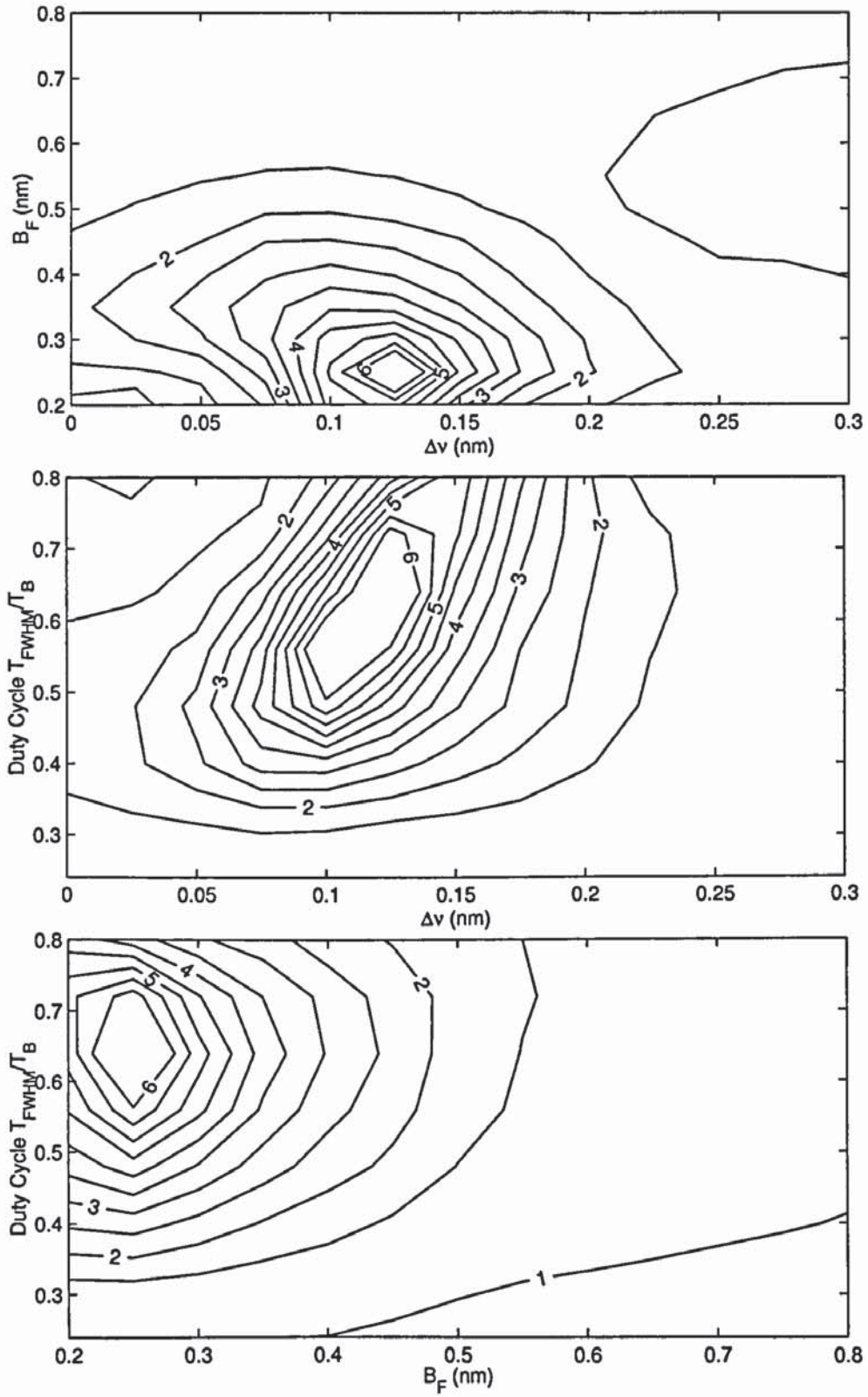

Figure 4.7: Three corresponding projections for $\alpha = 50$ GHz and $\beta = 75$ GHz. Top, filter bandwidth vs filter detuning. Middle, duty cycle vs filter detuning. Bottom, duty cycle vs filter bandwidth.

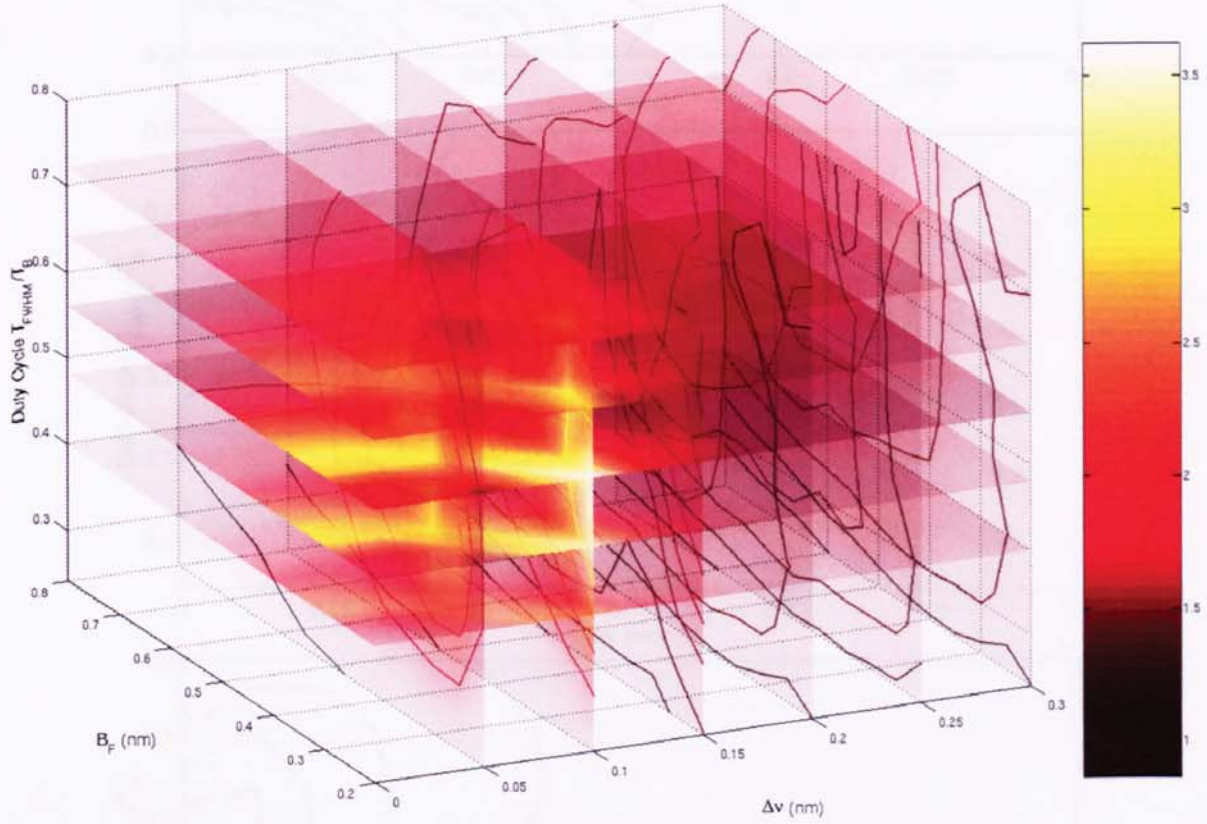

Figure 4.8: 3D volume plot of optimum system parameters for $\alpha = 62.5$ GHz and $\beta = 62.5$ GHz.

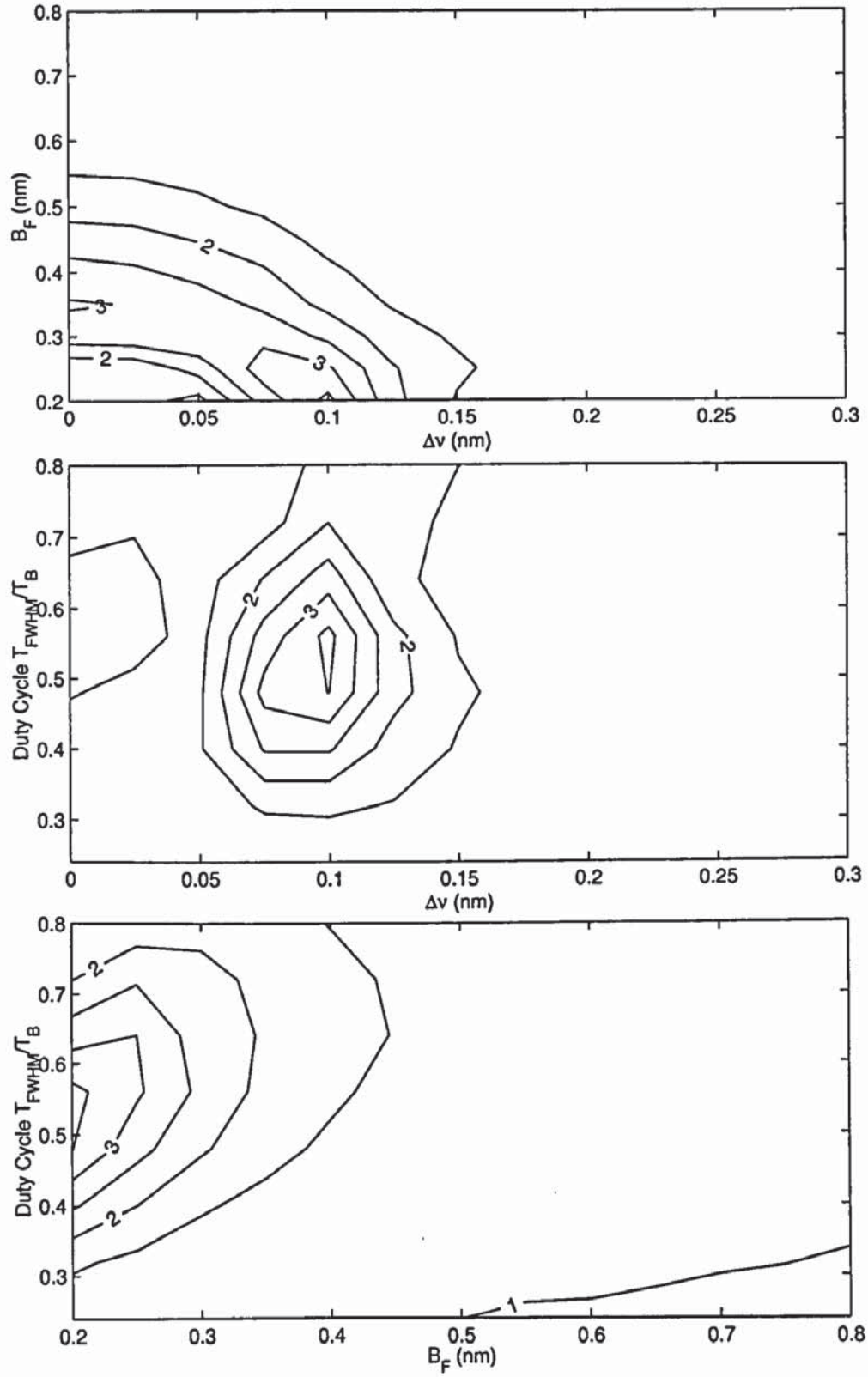

Figure 4.9: Three corresponding projections for $\alpha = 62.5$ GHz and $\beta = 62.5$ GHz. Top, filter bandwidth vs filter detuning. Middle, duty cycle vs filter detuning. Bottom, duty cycle vs filter bandwidth.

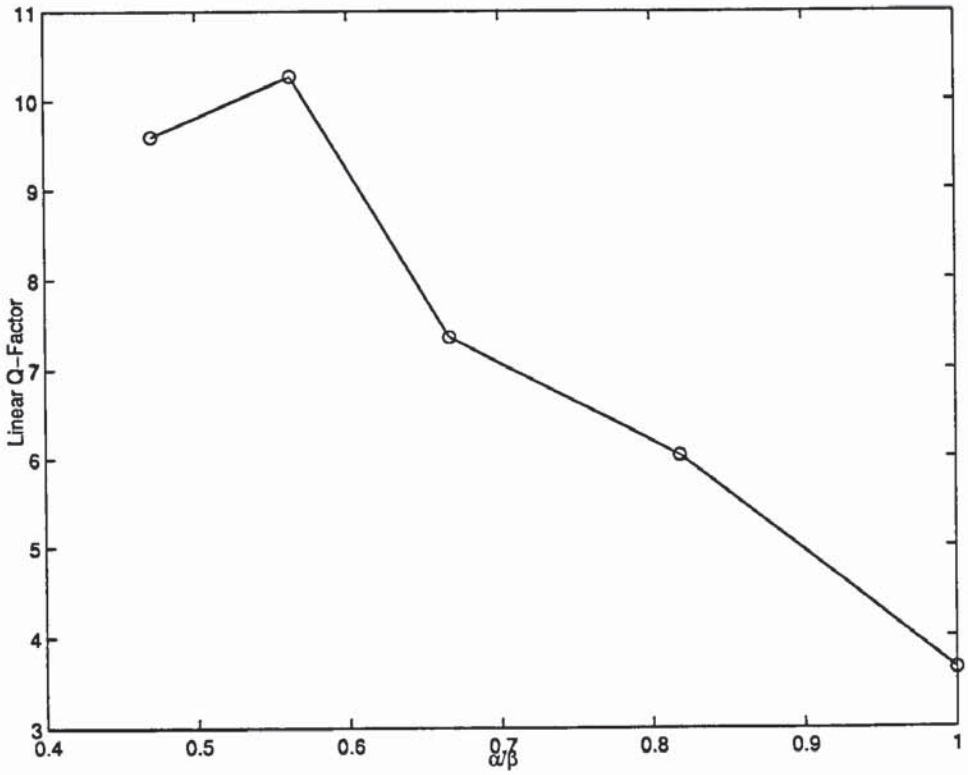

Figure 4.10: Linear Q-factor versus α/β.

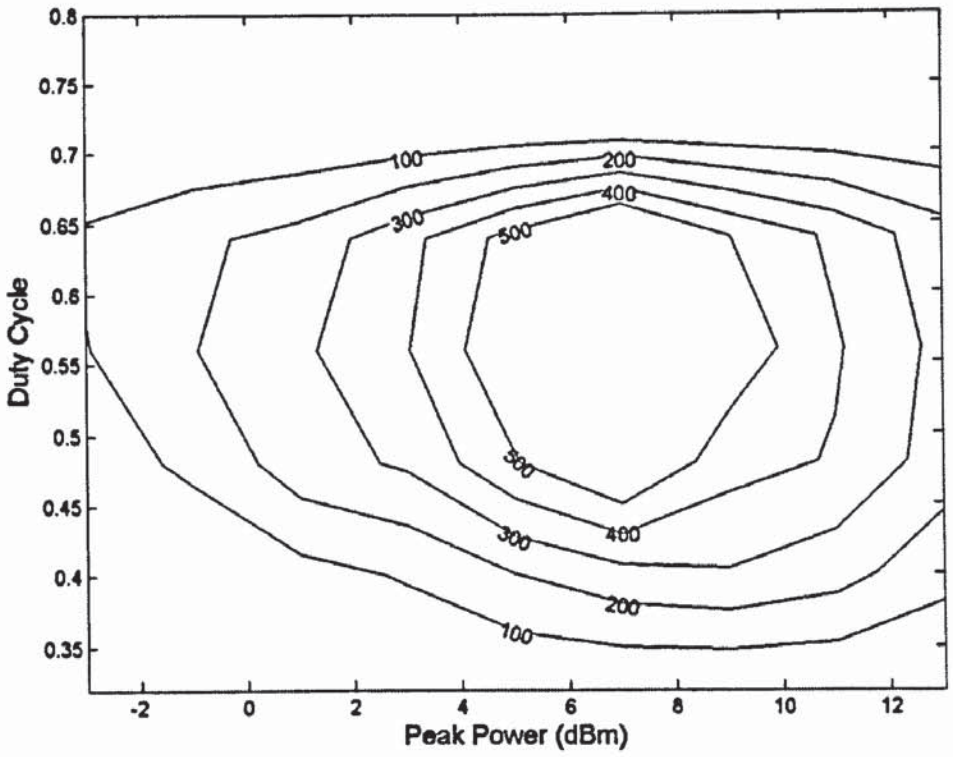

Figure 4.11: Maximum transmission distance optimisation in terms of pulse peak power and duty cycle.

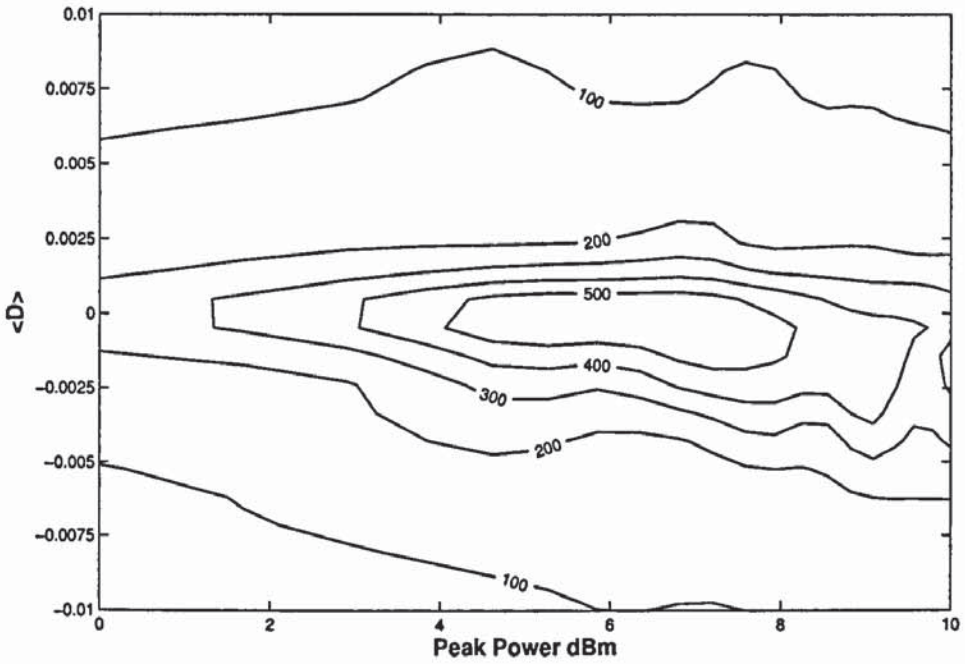

Figure 4.12: Maximum transmission distance optimisation in terms of pulse peak power and average dispersion.

Chapter 5

Numerical Modeling RZ-DPSK and DWDM Transmission

In the previous chapters we have studied the effects of VSB filtering and duty cycle optimisation on both RZ-OOK and CS-RZ formats.

In this chapter we intend to extend our analysis of advanced modulation formats by considering the RZ-DPSK format.

We begin the analysis with an investigation into the numerical technique used in measuring the performance of a DPSK optical signal (i.e. an estimation of the BER). Section 5.2, describes analytically, a new approach into estimating the performance of phase modulated data embedded into a optical signal (i.e. the calculation of the Q-factor).

Section 5.3, highlights the considerations needed when numerically implementing the new Q-factor calculation method.

By using the information presented in section 2.10, we are now able to numerically construct RZ-DPSK transmitters and receivers. Hence, we proceed with our analysis of DWDM optical transmission systems, by applying RZ-DPSK to a practical DWDM application, in section 5.4.

The optical transmission system that we will numerically model is described in section 5.5.

Section 5.6 describes the implementation of the numerical simulations and the optimisa-

tion strategy employed.

Finally the results of our extensive, large scale, numerical simulations are reported in section 5.7.

5.1 Introduction

Here we investigate a promising signal modulation technique known as RZ-DPSK modulation, which has gathered a lot of research interest recently [63–77].

The RZ-DPSK format is different from OOK and CS-RZ in that each bit slot is occupied with a pulse. The data is encoded in the change of phase between adjacent pulses. This makes the encoded data more resistant to the detrimental effects encountered during propagation along the optical fibre, in particular IFWM and ghost pulse generation.

As seen in section 2.10, the inherent OSNR benefits of RZ-DPSK enables us to extend the transmission distance, reduce optical launch power or design cheaper lightwave systems, by using components of lower quality.

5.2 Modeling DPSK Performance

In the early period of optical fibre communications, more specifically the late 1980's and beginning of the 1990's, extensive research was done on the receiver sensitivity of DPSK modulation formats [78–81]. One of the most striking results found at that time was the observation that a DPSK signal has a receiver sensitivity advantage over an OOK signal by approximately 3dB [82–85]. It was suggested more recently [86], that the standard numerical techniques, used to calculate the BER (based on Gaussian statistics) are unreliable for DPSK modulation format. This was due to the inherent non-Gaussian nature of the noise in the output intensity of the balanced receiver.

The BER is used as a measure of the performance of an optical fibre system. However, numerically the computational task of simulating bit patterns of the order 10^9 bits is highly unrealistic and a waste of resources. Thus an estimation of the BER is calculated through the statistical fluctuations of the ones and zeros of the received electrical signal, comprising of

only a few hundred bits. This approximation is based on Gaussian statistics and known as the Q-factor (quality factor). For an OOK and CS-RZ the Q-factor is defined as (see Appendix B) [87]

$$Q = \frac{|I_1 - I_0|}{\sigma_1 + \sigma_0} \tag{5.1}$$

where $I_1 - I_0$ is defined as the separations of the intensities of the "1" and "0" bits and σ_0 and σ_1 are the standard deviations of the intensities of the "1"s and "0"s.

The Q factor is related to the BER by

$$\text{BER} = \frac{1}{2}\text{erfc}\left(\frac{Q}{\sqrt{2}}\right) \approx \frac{1}{Q\sqrt{2\pi}} e^{-\frac{Q^2}{2}} \tag{5.2}$$

For intensity modulated systems this method gives a good prediction of the performance of the system, even though the actual noise distribution is not Gaussian [87].

In [86], it was suggested that a more reliable estimate of the BER in DPSK systems can be obtained by defining the Q-factor in the field domain, in contrast to the usual practice for OOK. Here we outline the Q model proposed in [86] for the BER calculation for DSPK. We consider a linear amplified optical transmission system with a field of N RZ pulses. The analytical description of the signal will take the form

$$F(t) = \left[\sum_{n=0}^{N-1} a_n u(t - nT) + z(t)\right] e^{-i\omega_c t} + c.c. \tag{5.3}$$

where n is the n^{th} bit, T is the bit period (temporal separation of the optical pulses), ω_c is the angular frequency of the optical carrier, $u(t - nT)$ is the envelope of the pulse, a_n the complex amplitude of the pulse and $z(t)$ is the additive Gaussian noise. The data in a DPSK signal, as opposed to OOK and CS-RZ, is encoded in the relative change of phase between adjacent bits, a_n and a_{n-1}. For the case of simplicity we will choose $a_n = \pm 1$, a "1" will be represented by a phase change of π and a "0" will be encoded by a 0 phase change between pulses a_n and a_{n-1}.

We place a matched optical filter in front of the receiver, in order to optimise the performance. Its impulse response function is given by

$$h(t) = \frac{1}{\sqrt{E_b}} u(-t) e^{i\omega_c t} + c.c. \tag{5.4}$$

where the energy per bit, E_b is defined to be

$$E_b = \int_{-\frac{T}{2}}^{\frac{T}{2}} u^*(t) u(t) dt \tag{5.5}$$

We now filter the signal by applying the convolution theorem on both $F(t)$ and $h(t)$. Thus giving us the signal

$$F_n(t) = f_n e^{-i\omega_c t} + c.c. \tag{5.6}$$

$$f_n = a_n \sqrt{E_b} + z_n \tag{5.7}$$

$$z_n = \int_{T(n-1/2)}^{T(n+1/2)} z(t) u^*(t - nT) dt \tag{5.8}$$

Here z_n is the filtered noise amplitude and is defined as

$$z_n = x_n + i y_n \tag{5.9}$$

where x_n and y_n are independent zero-mean Gaussian distributed quantities satisfying

$$\langle x_n^2 \rangle = \langle y_n^2 \rangle = \sigma^2 \tag{5.10}$$

Experimentally the filtered signal is decoded with the use of an MZDI. In essence it produces a constructive interference or a destructive interference between adjacent bits, relative to the difference of f_n and f_{n-1}. Analytically we simply apply the technique of the previous section, thus resulting in the two equations,

$$I_+ = \left| \frac{f_n + f_{n-1}}{2} \right|^2 \tag{5.11}$$

$$I_- = \left| \frac{f_n - f_{n-1}}{2} \right|^2 \tag{5.12}$$

We now subtract the two fields to give

$$\begin{aligned} I_{bal} &= I_+ - I_- \\ &= \frac{1}{4}\Big(f_n f_n^* + f_n f_{n-1}^* + f_{n-1} f_n^* + f_{n-1} f_{n-1}^* \\ &\quad - f_n f_n^* + f_n f_{n-1}^* + f_{n-1} f_n^* - f_{n-1} f_{n-1}^*\Big) \\ &= \frac{f_n f_{n-1}^* + f_n^* f_{n-1}}{2} \end{aligned} \tag{5.13}$$

We now substitute equations 5.7 and 5.9 into 5.13 and simplify, thus obtaining the following

$$I_{bal} = \left(a_n\sqrt{E_b} + x_n\right)\left(a_{n-1}\sqrt{E_b} + x_{n-1}\right) + y_n y_{n-1} \tag{5.14}$$

If we take the Gaussian noise contribution in equation 5.14 to be small, we can simplify 5.14 such that

$$I_{bal} \approx a_n a_{n-1} E_b \tag{5.15}$$

We note from equation 5.15, that depending on the relative sign of a_n and a_{n-1}, the zero bit is equivalent to $I_{bal} \approx E_b$ (i.e. no change in phase between adjacent bits, $a_n = a_{n-1}$) and the one bit is $I_{bal} \approx -E_b$ (i.e. a change in phase between adjacent bits, $a_n = -a_{n-1}$).

Using the Gaussian probability density function of x_n and y_n, it can be shown that the BER to be [86]

$$\text{BER} = \frac{1}{2}\exp\left(-\frac{E_b}{2\sigma^2}\right) \tag{5.16}$$

From equation 5.15 we can see that the output of the balanced receiver is $I_{bal} \approx \pm E_b$, thus corresponding to $I_1 - I_0 \approx 2E_b$. Since the z_n and z_{n-1} are independent we find that the standard deviation of I_{bal} is $\sigma_1 = \sigma_0 \approx \sigma\sqrt{2E_b}$. Thus equations 5.14 and 5.15 give the Q factor to be

$$Q \approx \frac{\sqrt{E_b}}{\sqrt{2}\sigma} \tag{5.17}$$

On substituting this into equation 5.2 we find the BER to be

$$\mathrm{BER} = \frac{1}{2}\mathrm{erfc}\left(\frac{Q}{\sqrt{(2)}}\right) \approx \sqrt{\frac{\sigma}{\pi E_b}} e^{-\frac{E_b}{4\sigma^2}} \tag{5.18}$$

Comparing Eq. 5.18 and Eq. 5.16 we note that the predicted BER in equation Eq. 5.18 is $\sim$ 3dB worse. Thus applying the conventional methods of equations Eq. 5.1 and Eq. 5.2 are inappropriate for DPSK signals. This is due fundamentally to the non Gaussian nature of the noise distribution in the output of the balanced receiver.

In order to obtain a more accurate prediction of the Q-factor, in [86] it was proposed to evaluate the variance of the $|f_n|$ before the MZDI, and an alternative "amplitude Q", Q_A was introduced as

$$Q_A = \frac{\langle |f_n| \rangle}{\sigma_{|f_n|}} \approx \frac{\sqrt{E_b}}{\sigma} \tag{5.19}$$

This Q-factor model, based on the assumption of a linear channel dominated by ASE noise, may be an overestimate of the performance in a nonlinear regime and is no longer reliable. To deal with the case of a nonlinear channel, in [86] it was proposed to evaluate the Q directly in the phase domain, by switching to polar coordinates and substituting $f_n = |f_n| e^{i\phi_n}$ into Eq. 5.13, thus I_{bal} becomes

$$I_{bal} = |f_n f_{n-1}| \cos \Delta\phi_n \tag{5.20}$$

Hence we define $\Delta\phi$ to be the differential phase,

$$\Delta\phi_n = \phi_n - \phi_{n-1} \tag{5.21}$$

Which is distributed around $\Delta\phi = 0$ for zero bits and around $\Delta\phi = \pi$ for the one bits. We thus introduce the Q based on the phase information of the signal, known as the differential-phase-Q, or $Q_{\Delta\phi}$ [86]

$$Q_{\Delta\phi} = \frac{\pi}{\sigma_{\Delta\phi,0} + \sigma_{\Delta\phi,\pi}} \tag{5.22}$$

$Q_{\Delta\phi}$ has been shown to qualitative reproduce the results obtained from direct counting BER calculation, and in particular, to correctly take into account nonlinear transmission

penalties at high launch powers [88]. To improve the accuracy of $Q_{\Delta\phi}$, a correction to the Gaussian approximation for the phase noise was proposed in [89], which yielded a modified differential phase Q equal to $Q_{\Delta\phi,mod} = 0.87Q_{\Delta\phi}$. However, in overall we can say that none of the existing Q models for the BER estimation for DSPK has an absolute superiority and there is still a search for a simple and reliable numerical method to estimate the BER of DPSK systems. For the purpose of this thesis, we choose the smaller one from Q_A and $Q_{\Delta\phi}$ as the overall Q for the BER estimation. In doing so we are able to take into account the contributions of both the amplitude noise and the phase noise as we vary the optical power levels in the DPSK simulations.

5.3 Numerical Implementation

In this section we briefly describe the numerically implementation of the Q factor calculation for DPSK signals, we will apply equations 5.19 and 5.22.

In order to obtain the phase information from the optical signal, We first transform the complex field, and extract the phase information using simple trigonometry.

We then proceed through the array and calculate the phase difference between the adjacent bits. Figure 5.1 shows the calculated phases. We note from figure 5.1, that we have a branch cut in the middle of our $\Delta\phi = \pi$ data. Making an accurate calculation of the variance of the data, in the current situation, would be inaccurate. This is due to the fact that the data points are spanning both sides of the branch cut, thus creating four possible values for $\Delta\phi$, which are 0, π, $-\pi$ and 2π, as opposed to just 0 and π.

We overcome this difficulty by simply moving the branch cut through $\frac{\pi}{2}$, thus remapping the data into a 0 to $\frac{3\pi}{2}$ space, as depicted in figure 5.2.

In its new location we are able to accurately calculate the variances of the 0 and π data. We finally produce eye diagrams of both the amplitude and the differential phase. Using these eye diagrams we scan the eye looking for the greatest eye opening. As illustrated in figure 5.3, the dashed vertical line scans the eye along the arrows. A dynamic decision level is used, which automatically adjusts to the optimum level as it scans the eye.

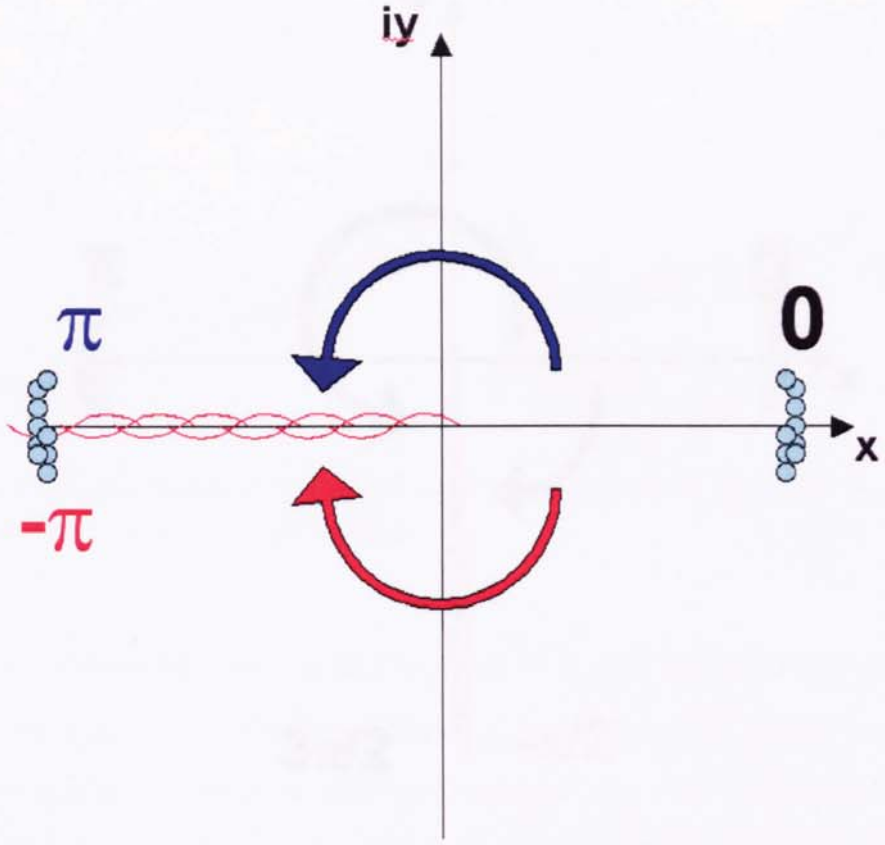

Figure 5.1: Calculated differential phase between adjacent bits.

5.4 Dense WDM Application

High spectral efficiency is a significant target in modern long haul fibre communications. New signal formats, and RZ-DPSK in particular, have become key enabling factors in increasing the spectral efficiency [90–97]. However, experimental studies of applications of the DPSK format in optical transmission have recently outpaced theoretical and numerical analysis. Such important resources for reaching the highest system performance, as carrier reshaping, channel pre- and post-filtering have not been systematically studied in the case of the new signal format. Asymmetric pre-filtering has been thoroughly studied for OOK formats (see e.g. [98]), and has recently been used for CS-RZ DPSK [99].

In this chapter we systematically explore the optimal duty cycle, carrier reshaping and channel pre- and post-filtering for RZ-DPSK system performance. Our main purpose is to

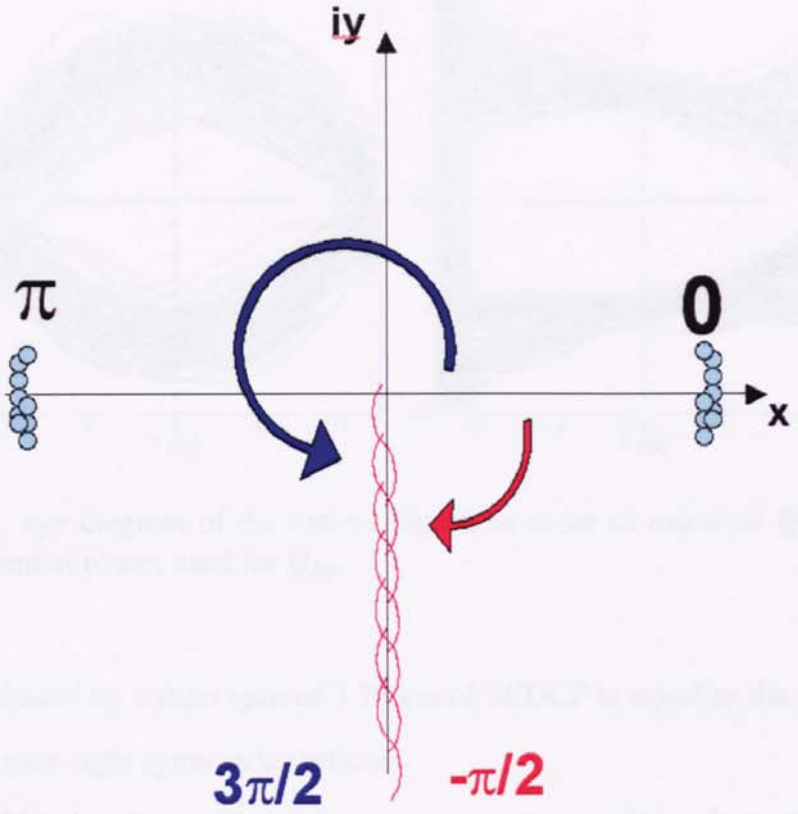

Figure 5.2: Remapping of Phase information into 0, $\frac{3\pi}{2}$ space.

tune the system and signal parameters corresponding to the highest experimentally available transoceanic transmission at spectral efficiency of 0.8 bit/s/Hz recently reported in [100] to further improve the performance.

5.5 System Configuration

The chosen system is essentially equivalent to that reported in [100].

The transmission line comprises of periodically allocated dispersion map including eight symmetrically deployed pairs of enlarged effective area single mode fibre (EE-SMF) with slope compensating dispersion-compensating fibre (SCDCF) between the spans of EE-SMF. The fibre parameters are summarized in Table 5.1 and the scheme of the modelled system is shown in figure 5.4.

Each symmetric map is followed by an EDFA, to compensate for optical attenuation.The

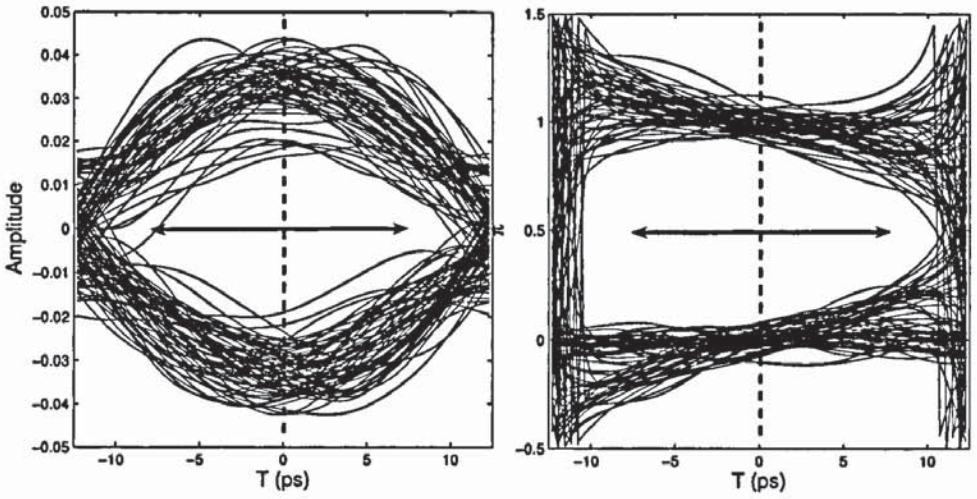

Figure 5.3: Left, eye diagram of the optical signal, in order to calculate Q_A. Right eye diagram of differential phase, used for $Q_{\Delta\phi}$.

last section is followed by a short span of 3.75 km of SCDCF to equalize the residual chromatic dispersion over eight symmetric sections.

Following [100], the choice of simple components was made to demonstrate superior ultra high density, up to 80% spectral efficient, transmission by means of fine tuning of system and signal parameters. No PDM have been used. Note that PDM could could be considered as an additional resort to improve the results.

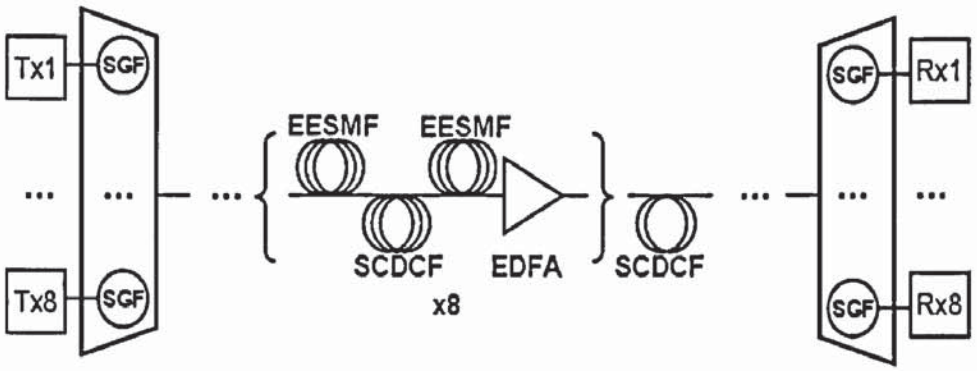

Figure 5.4: Scheme of the modelled system. The same SG filters are used for pre- and post-filtering.

Table 5.1: Fibre parameters.

Fibre	EE-SMF	SCDCF
D ps/(nm km)	20	-40
S ps/(nm^2 km)	0.06	-0.12
A_{eff} μm^2	110	30
L km	29	14

5.6 Modelling

We have performed numerical modelling of 8 channel RZ-DPSK transmission at 40 Gbit/s rate. Each channel had been pre-filtered before multiplexing in order to reduce inter-channel crosstalk. The same filters were used at the DEMUX. The following parameters were tuned during the optimisation process:

1. MUX/DEMUX filtering, including the optimisation of the detuning, bandwidth,and shape. SG filters of different orders with the filter transfer function,

$$H(f) = \exp\left[-\frac{1}{2}\left(\frac{(f-f_0)}{B}\right)^N\right] \tag{5.23}$$

have been tested over the filter steepness parameter N, as well as the filter bandwidth F_B and detuning $\Delta\nu$. The detuning of the filter were preformed away from the central frequency of the channel. All filters were detuned in the same direction.

2. Carrier pulse characteristics including the, duty cycle and pulse shape which varied from Gaussian to super-Gaussian of different orders.

A multi-stage optimisation strategy has been adopted due to the very large number of optimisation parameters. First, back to back optimisation has been performed of the carrier duty cycle and shape as well as the MUX/DEMUX filtering parameters. In a second stage, the optimized parameters have been used in a point-to-point scenario.

5.7 Results

Before we begin our inspection of the results, let us briefly observe the effects of narrow filtering on the signal. As it is seen from figure 5.5 the signal is distorted by the applica-

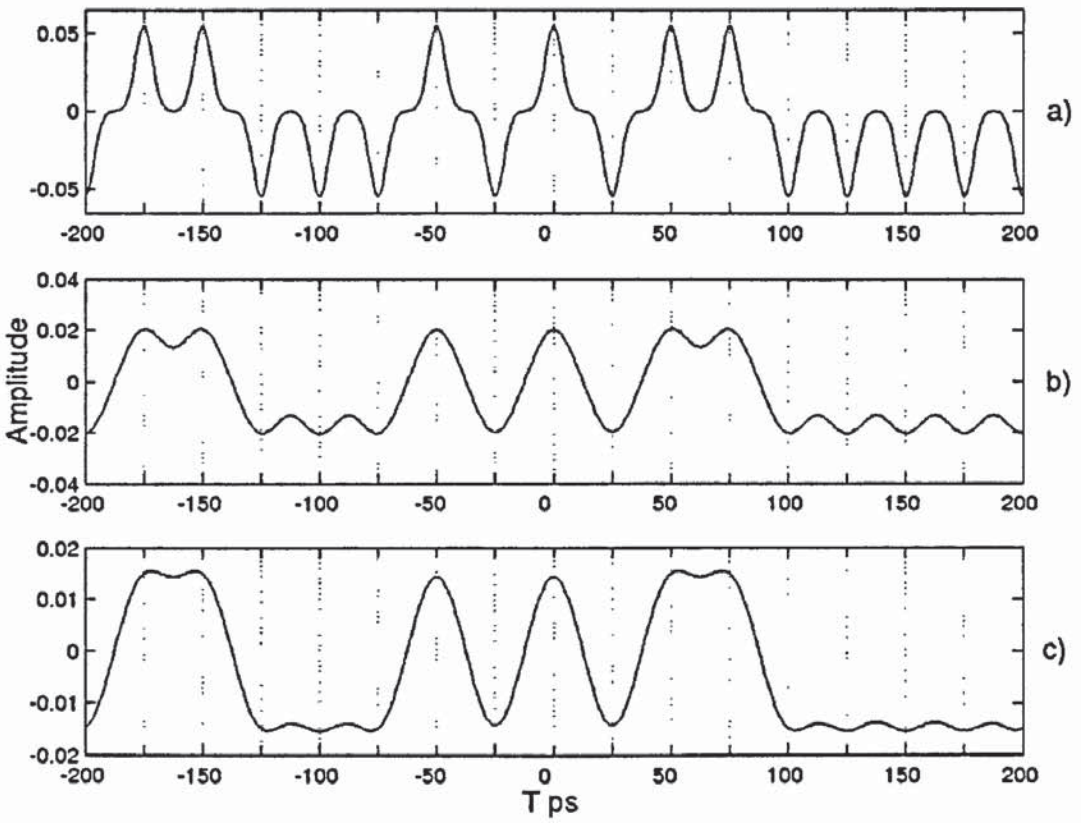

Figure 5.5: The effect of narrow filtering on the temporal domain signal characteristics. Top, unfiltered signal. Middle, application of filter for channel reshaping at the MUX. Bottom, application of filter for channel isolation at the DEMUX.

tion of narrow filters. Which results in a change of the temporal pulse characteristics, most importantly, we note an alteration of the duty cycle.

The results of the parameter optimisation are presented in figures 5.6, 5.7 5.8, 5.10 and 5.9. Figure 5.6 shows the contours of the linear Q-factor versus the filtering parameters (filter bandwidth and detuning) for different pulse width. Filter shapes were kept Gaussian. It was found that a pulse-width of 6ps provided the best performance.

Figure 5.7 shows the contours of the linear Q-factor versus the same filter parameters but for different filter shapes for a fixed duty cycle. It was found that steeper filters provide better discrimination between the channels and practically eliminate inter-channel crosstalk starting from N=12. In all the following simulations this parameter was set to 16 as steeper filters do not significantly improve performance and could be difficult to manufacture.

Figures 5.8 and 5.9 show the influence of the carrier shape on system performance. Fig-

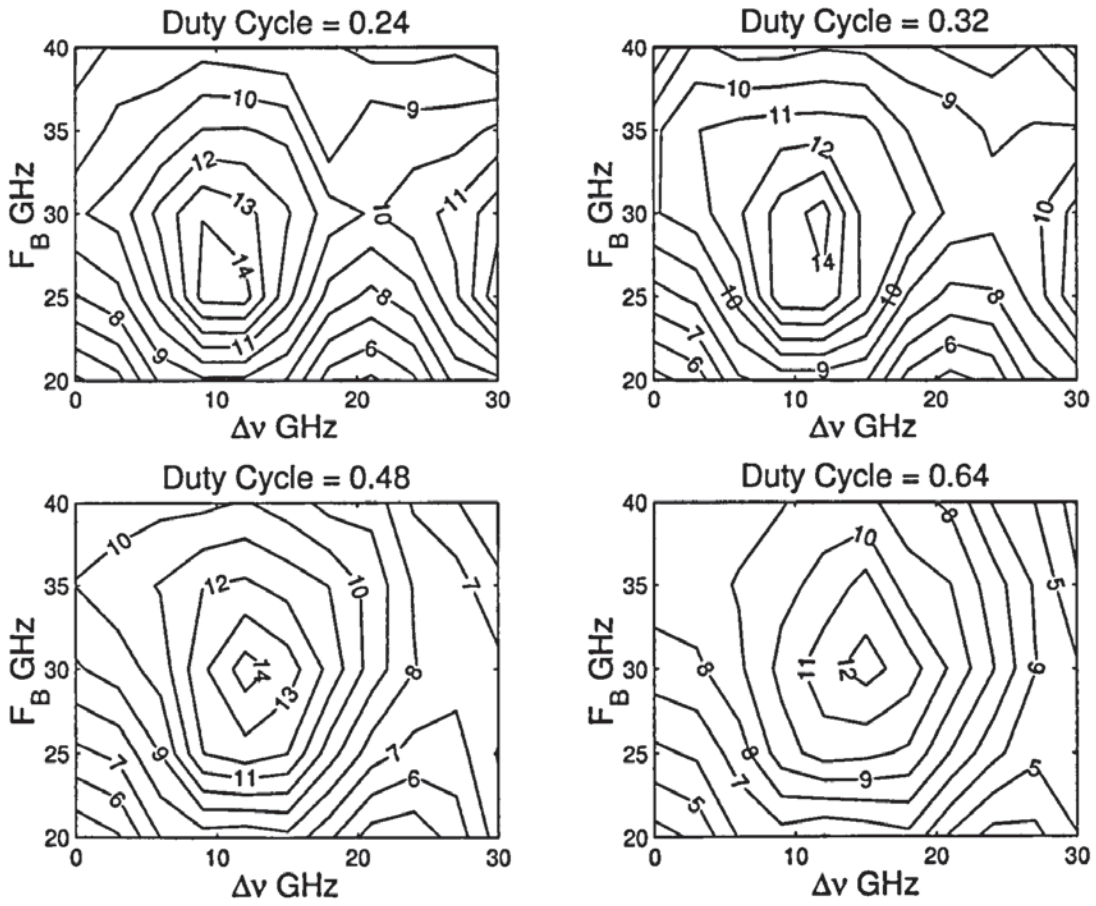

Figure 5.6: Contour plots of linear Q-factor versus filter bandwidth and detuning for different duty cycles, for back-to-back simulations

ure 5.8(a) and 5.8(b) depict the back-to-back performance gained by using a super-Gaussian carrier versus duty cycle. It is seen that the performance gain achieved by simply reshaping the carrier can be as much as 10 dB whereas after 2000 km the performance gain is still a respectable 4 dB in a wide range of duty cycle values as shown in figure 5.8b. Thus, for RZ-DPSK, we observe a direct correlation between carrier shape and transmission performance. We deduce that if we simply lower the duty cycle, we can easily improve propagation performance.

Figure 5.10 illustrates another benefit of using super-Gaussian carriers with steep shape index M=20. It shows the system performance after 2000 km versus the signal peak power. It is seen that super-Gaussian signals perform better at higher power by approximately 2 dB which results in a noticeably better signal to noise ratio. Using the optimum parameters and without the application of forward error correction (FEC), a transmission distance of 3700km

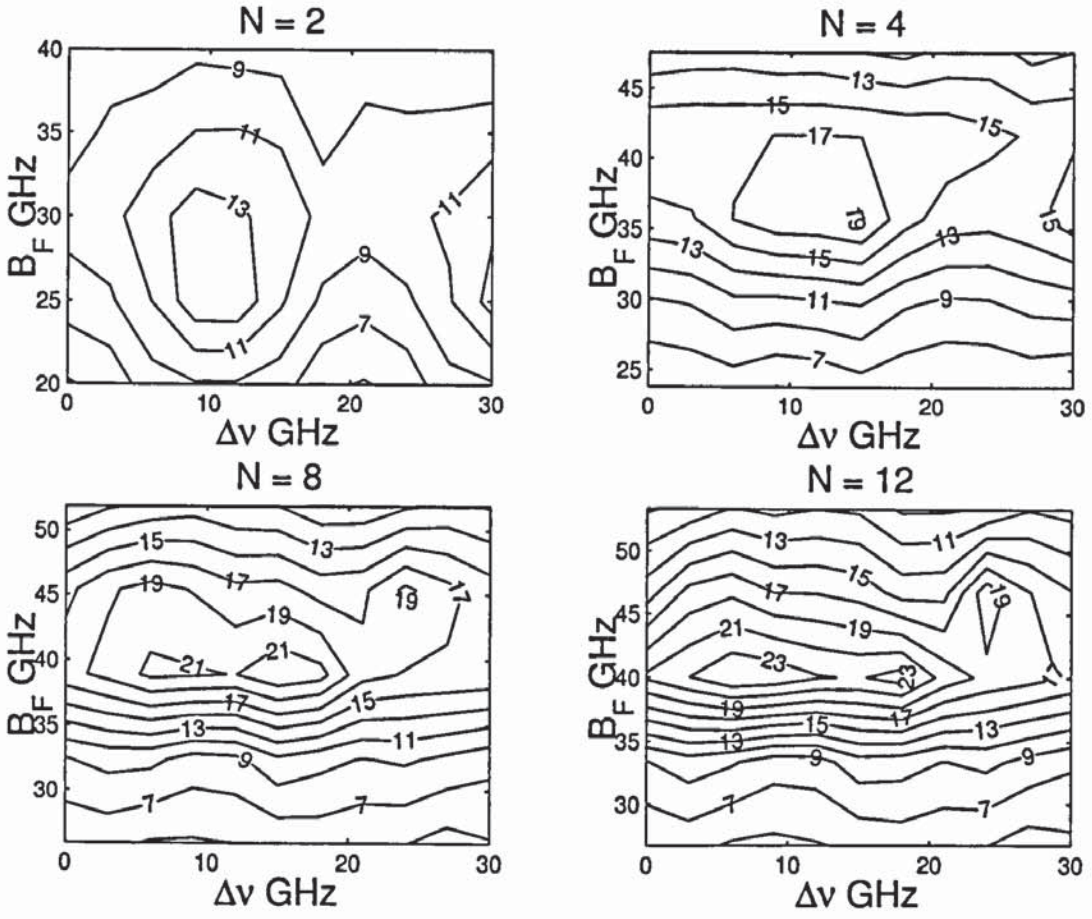

Figure 5.7: Contour plots of linear Q-factor versus filter bandwidth and detuning for different filter shapes: Gaussian: (a) N=2 and SG (b) N=4, (c) N=8, (d) N=12, for back-to-back simulations.

with a Q-factor of 15 dB, was achieved. Implementing FEC into the lightwave system would result in obtaining a transmission distance of over 6000km.

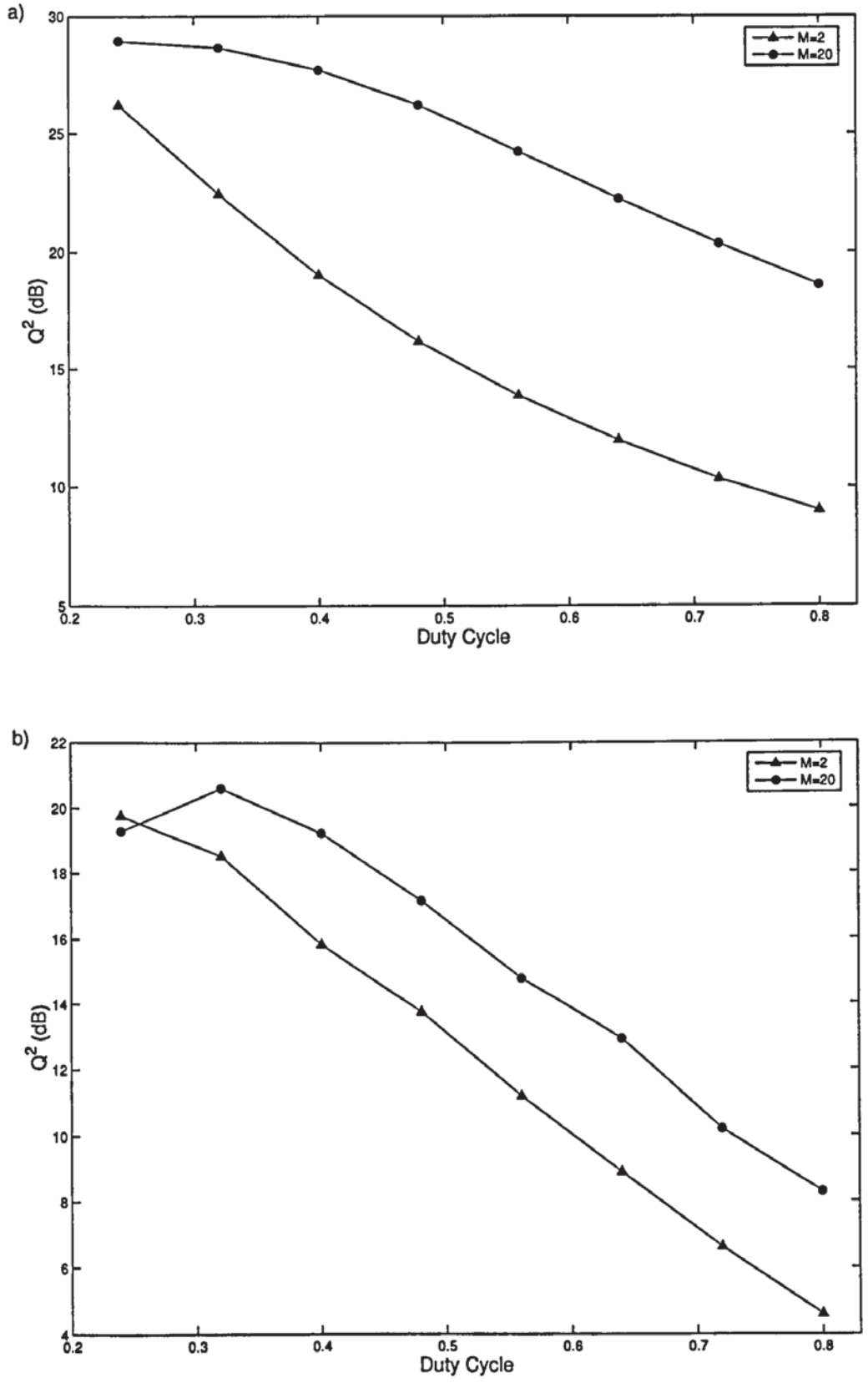

Figure 5.8: Q-Factor versus duty cycle for different carrier shapes: Gaussian M=2 (triangles) and super-Gaussian M=20 (circles): (a) - back to back (b)- after 2000 km.

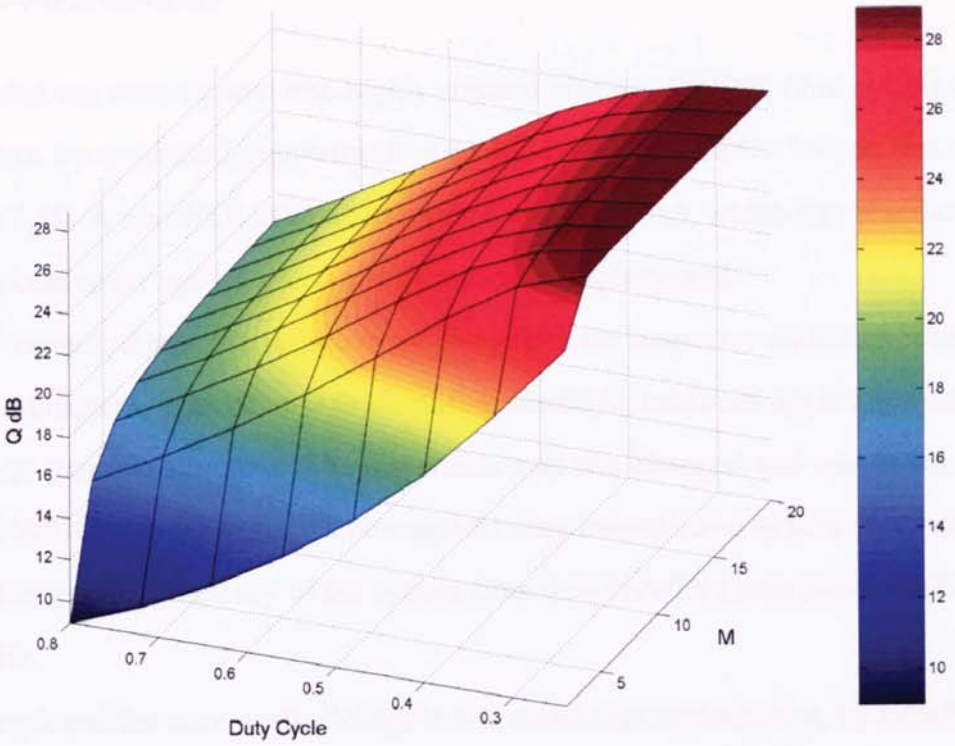

Figure 5.9: Q-factor versus pulse duty cycle and super-Gaussianicity parameter M for back-to-back simulations.

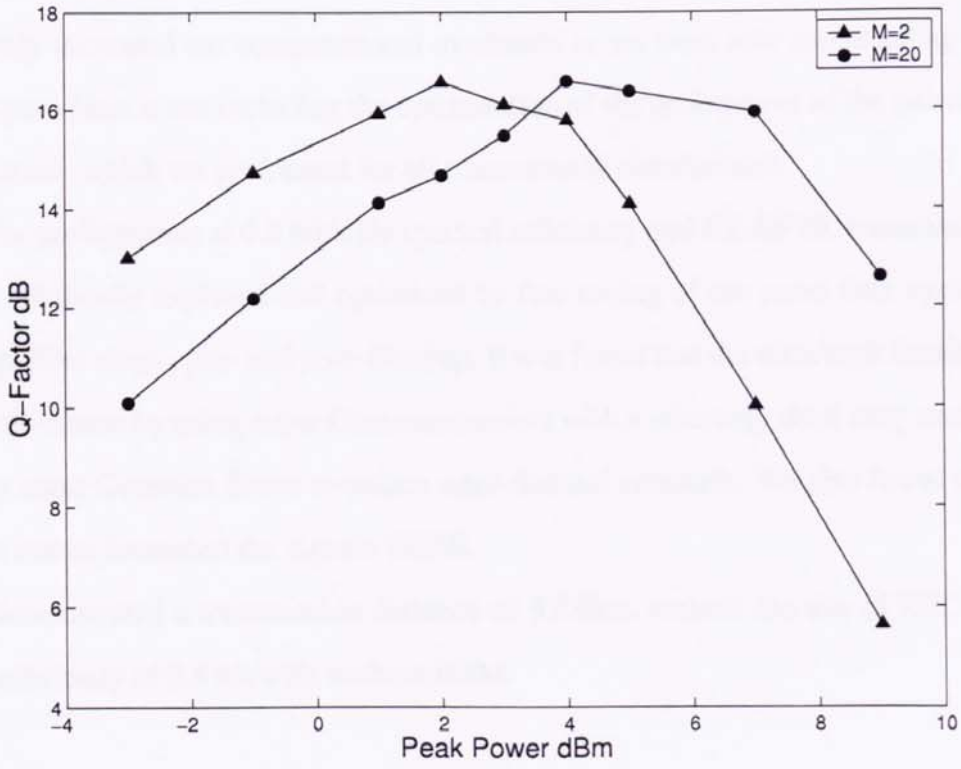

Figure 5.10: Q-Factor versus signal peak power for different carriers: M=2 (triangles) and M=20 (circles) after 2000 km.

5.8 Conclusions

We extended our investigation into highly spectral efficient DWDM fibre optical transmission systems, by numerically implementing the RZ-DPSK modulation format, first discussed in section 2.10. A new BER estimation method was presented, which was based on the differential phase of the optical signal and numerically implemented.

In our numerical simulations, we move away from the frequency allocation scheme, used in previous chapters, in an attempt to simplify practical/commercial application and considered a more periodic structure. The dispersion map was changed and was based on a EE-SMF and SCDCF fibres. With this new optical fibre transmission system, We were able to increase the spectral efficiency of the system from 0.64 bit/s/Hz (from previous chapters) to 0.8 bit/s/Hz.

We employed the same methodology in our simulation optimisation, by simultaneously optimising both the spectral and temporal domain parameters. We further investigated the correlation between spectral reshaping and the temporal form of optical pulses by including the pulse shape of the carrier as a variable in our parameter optimisation space. This significantly increased our computational overheads as we were now investigating a 5D parameter space (this is not including the optimisation of the peak power of the pulse and post compensation, which we preformed for all transmission simulations).

System performance at 0.8 bit/s/Hz spectral efficiency and RZ-DPSK transmission have been systematically explored and optimised by fine tuning of the pulse duty cycle, carrier reshaping, filter shape, pre- and post-filtering. It was found that the ultra high density system gains performance by using super Gaussian carriers with a relatively short duty cycle of 0.24 and steep super Gaussian filters to reduce inter-channel crosstalk. We also found that super Gaussian carrier increased the signals OSNR.

We demonstrated a transmission distance of 3700km without the use of FEC and high spectral efficiency of 0.8 bit/s/Hz without PDM.

Chapter 6

RZ-DPSK Transmission with In-Line SOAs

6.1 Introduction

Semiconductor optical amplifiers (SOAs) are a valuable alternative to in-line EDFAs and Raman amplifiers (RAs) for fibre optical communication systems. They offer a number of advantages for ultrahigh capacity transmission systems. These include compactness, integrability, low cost, low power consumption, and wide gain spectrum.

However, the use of SOAs in commercial fibre systems is very limited. The intrinsic nonlinear fast-gain dynamics, which differentiates SOAs from EDFAs and RAs and leads to data pattern-induced waveform distortion and inter-channel crosstalk, poses serious challenges to employing SOAs in the saturation regime with conventional OOK signals. A number of methods have been proposed to mitigate the detrimental effects of the SOA fast-gain dynamics [111–113]. In particular, significant improvement of the performance of SOAs has been demonstrated to be attainable by use of modulation formats with a homogeneous and data-free signal power distribution such as DPSK [114–116]. Furthermore, SOAs act as self-amplitude/phase modulators on continuous sequences of RZ pulses, which may lead to a solitary wave-sustaining transmission [117].

The amplitude-phase modulation action of SOAs can stabilise the carrier pulses, thus

enabling the re-emergency of solitonic technologies within an appropriate dispersion management context. A soliton-like transmission potentially offers new ways of alleviating or suppressing the growth of phase noise [118,119], which is the main limiting factor for DPSK systems. The full potential of this transmission technique is still to be explored.

In this chapter, we numerically demonstrate the feasibility of a robust quasi-periodic nonlinear (soliton-like) transmission regime of RZ-DPSK data utilising short pulses at both 40 Gbit/s and 80 Gbit/s channel rate, in single-mode fibre using cascaded in-line SOAs.

6.2 SOA Model

Throughout this chapter we adopt the following phenomenological model, first proposed in [101], for the action of the SOA. We assume a traveling-wave SOA, which can be described by a conventional rate equation for the carrier density and a linear relationship between the carrier density and the induced complex susceptibility. Neglecting carrier diffusion, intrinsic losses and ASE of the SOA. Using the model, we get for the slowly varying amplitude of the pulse U_{out} at the output is defined as,

$$U_{out} = e^{\frac{h(1-i\delta)}{2}} U_{in} \tag{6.1}$$

where the time dependent gain $h(t)$ is given by

$$\frac{dh}{dt} = \frac{h_0 - h}{\tau_c} - \frac{|U_{in}|^2}{\varepsilon_{sat}} \left(e^h - 1\right) \tag{6.2}$$

The gain dynamics is governed essentially by three phenomenological parameters, namely, the saturation energy ε_{sat}, the carrier lifetime t_c and the small signal gain $G_0 = e^{h_0}$. The linewidth enhancement factor δ, is the ratio between the real and imaginary parts of the carrier-induced susceptibility and is a phenomenological constant and amounts to $\delta \approx 5$ for a typical SOA.

We numerically solve the above equations.

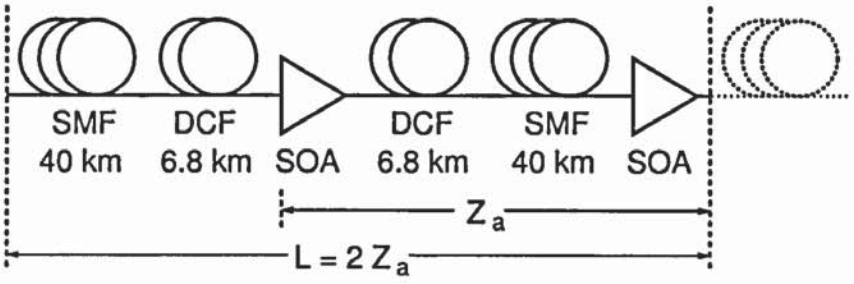

Figure 6.1: One element of the periodic transmission system.

6.3 Modelled System

The scheme of the transmission system considered in this chapter is shown in Fig. 6.1. The transmission link is composed of SMF spans and DCF spans. The unit cell of the periodic transmission system comprises of a SMF-DCF block and its mirror DCF-SMF block. The SMF has a dispersion of $D = 17\,\text{ps/(nm km)}$, a dispersion slope of $S = 0.065\,\text{ps/(nm}^2\text{km)}$, a nonlinear coefficient of $\gamma = 1.3\,(\text{W km})^{-1}$, and an attenuation of $\alpha = 0.21\,\text{dB/km}$. The parameters of the DCF are: $D = -100\,\text{ps/(nm km)}$, $S = -0.38\,\text{ps/(nm}^2\text{km)}$, $\gamma = 5.5\,(\text{W km})^{-1}$, and $\alpha = 0.5\,\text{dB/km}$. The length of each SMF segment is 40 km, and the DCF span length is set to 6.8 km such that the residual dispersion is zero. A SOA follows each of the two blocks.

The discrete action of the SOA is modelled by equations (6.1) and (6.2). Typical parameters are used for the SOA: linewidth enhancement factor $\delta = 5$, saturation energy $\varepsilon_{\text{sat}} = 3\,\text{pJ}$, and gain recovery time $\tau_c = 200\,\text{ps}$. The SOA noise figure is 5 dB.

6.4 Basic Technique

In much the same way as optical solitons arise from a balance between chromatic dispersion and Kerr nonlinearity in the fibre, the key physical mechanism that enables the soliton-like quasi-periodic regime is a balance between dispersion in the fibre and nonlinear amplitude-phase modulation in the lumped SOA. The fibre nonlinearity, although it is less pronounced in the quasi-linear propagation regime, also contributes to the balance. To some extent the soliton-like regime can be considered as a mixture of the quasi-linear propagation regime in the fibre and nonlinear mapping by the point-action SOAs. Indeed, the signal propagation

through the fibre parts of the system can be well described by the quasi-linear approximation. Nonlinear effects can be then accounted for as a sequence of transformations by the chain of SOAs.

The action of the SOA on the RZ-DPSK pulse trains can be described as follows: since in the DPSK format, an equal amount of energy is used in every bit slot, each pulse in the input signal effectively saturates the SOA gain in the same way, and this results in a nearly homogeneous periodically modulated gain response. The gain response, in turn, produces nearly homogeneous (identical from pulse to pulse) periodic amplitude and phase modulations to the output signal. Due to the nearly homogeneous amplitude modulation and chirp, the amplitude noise and waveform distortion, which are well-known problems of SOAs operating in the saturation regime with conventional OOK modulation, are significantly reduced for DPSK [102–104].

First we consider a periodic continuous sequence of pulses propagating through a single SOA. For a given average power $\bar{P}_{\text{in}}$ at the input of the SOA, the value of the SOA unsaturated gain G_0 that minimises variations of the output signal can be determined by the well-known steady-state gain equation [106]

$$\frac{\ln(G_0/\bar{G})}{\bar{G}-1} = \frac{\bar{P}_{\text{in}}\tau_c}{\varepsilon_{\text{sat}}}, \tag{6.3}$$

where $\bar{G}$ is the steady-state gain, and is balanced with the total fiber loss.

Next we consider the transformation of a pulse train after propagation in one segment of the transmission line as the mapping of the input signal into the output signal. A steady steady-state propagation regime (if it exists) in which the pulse train reproduces periodically at the output of each element of the line, corresponds to a fixed point of the mapping. For such a fixed point the integral quantity

$$I = \int_{-NT/2}^{NT/2} \mathrm{d}t \left(|u_{\text{out}}^{\text{syst}}(t-t_0)|^2 - |u_{\text{in}}^{\text{syst}}(t)|^2 \right)^2 \tag{6.4}$$

is zero, where $u_{\text{in}}^{\text{syst}}$ and $u_{\text{out}}^{\text{syst}}$ are the optical fields at the input and the output of the unit cell of the system, parameter t_0 is set such that it compensates the time shift introduced by the SOA, N is the length of the bit pattern, and T is the bit period.

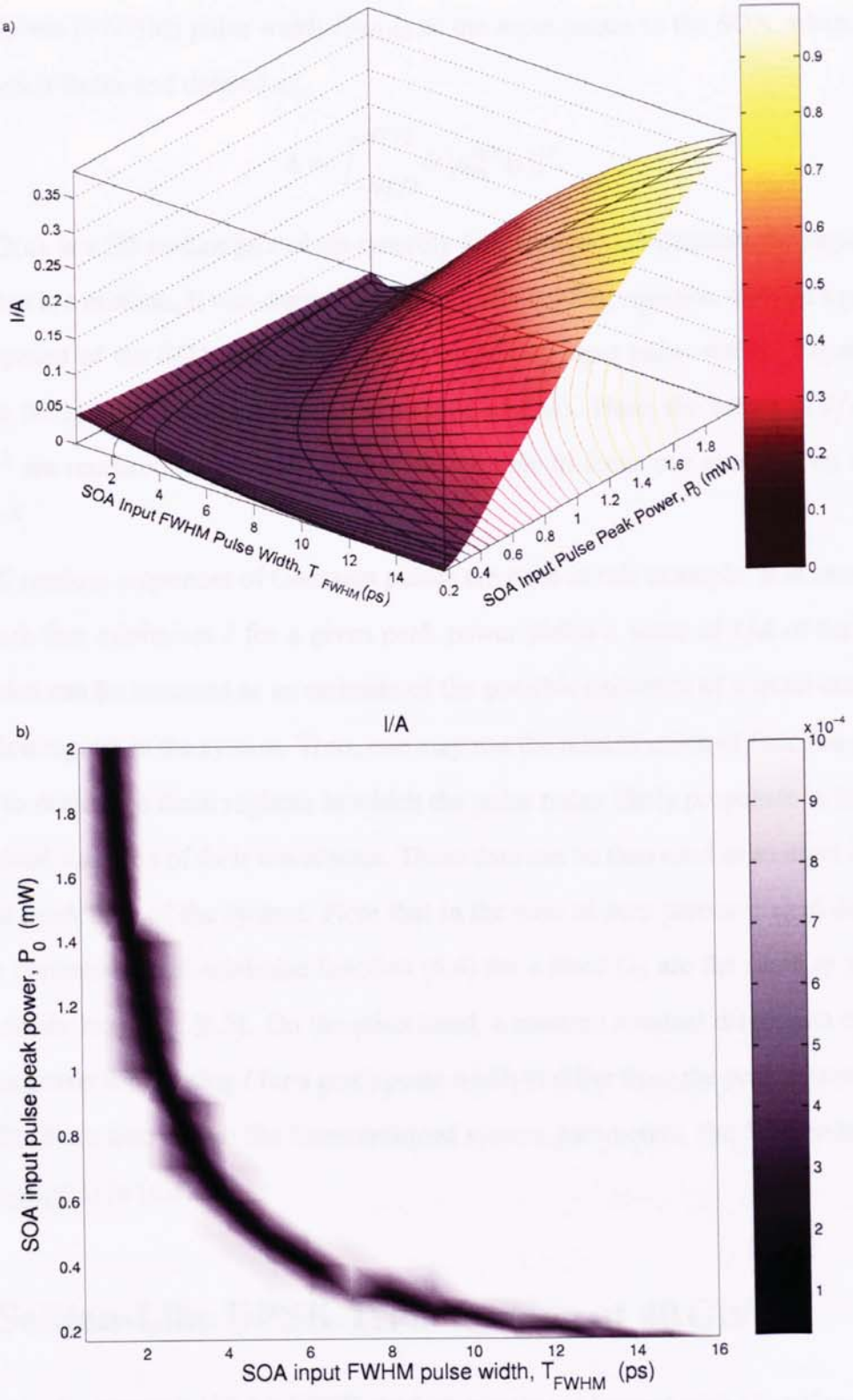

Figure 6.2: a) 3D surface plot of integral quantity I/A. b) Integral quantity I/A versus width and peak power of the input pulses to the SOA.

Figure 6.2 shows a plot of I/A as a function of the peak power P_0 and full-width at half-maximum (FWHM) pulse width T_{FWHM} of the input pulses to the SOA, where A is the normalisation factor and defined as,

$$A = \int_{-NT/2}^{NT/2} \mathrm{d}t \, |u_{\mathrm{in}}^{\mathrm{syst}}(t)|^4, \tag{6.5}$$

Figure 6.2(a), is a 3D surface plot of the quantity I/A, designed to illustrate the region where the function is a minima. It was created by numerically solving equation (6.4) on a parameter grid composed of the SOA input peak power and SOA input pulse width. Figure 6.2(b), highlights the region of interest (the minimisation of I/A). Here, the values of I/A greater than 10^{-3} are rendered transparent, so that we are able to focus our attention on values of order 10^{-4}.

DPSK random sequences of Gaussian pulses are used in this example. It is seen that the pulse width that minimises I for a given peak power yields a value of I/A of the order of 10^{-4}, which can be assumed as an estimate of the possible existence of a quasi-steady state propagation regime in the system. Thus, one may use the minimisation of function (6.4) as a criterion to determine those regimes in which the pulse trains likely propagate in the system with minimal variation of their waveforms. These data can be then used as an input in the full numerical modelling of the system. Note that in the case of zero path-averaged dispersion, the pulse parameters that minimise function (6.4) for a fixed G_0 are the same as those that one can obtain from Eq. (6.3). On the other hand, a nonzero residual dispersion causes the pulse peak power minimising I for a given pulse width to differ from the peak power obtained from (6.3). Note also that at the forementioned system parameters, the SOA-induced time shift is negligible in (6.4).

6.5 Soliton-Like DPSK Transmission at 40 Gb/s

We numerically transmit 128-bit DPSK random sequences formed with Gaussian pulses by use of the split-step Fourier method. The pulse parameters and the SOA small-signal gain are chosen in accordance with the minimisation of function (6.4) or, equivalently, with relation (6.3).

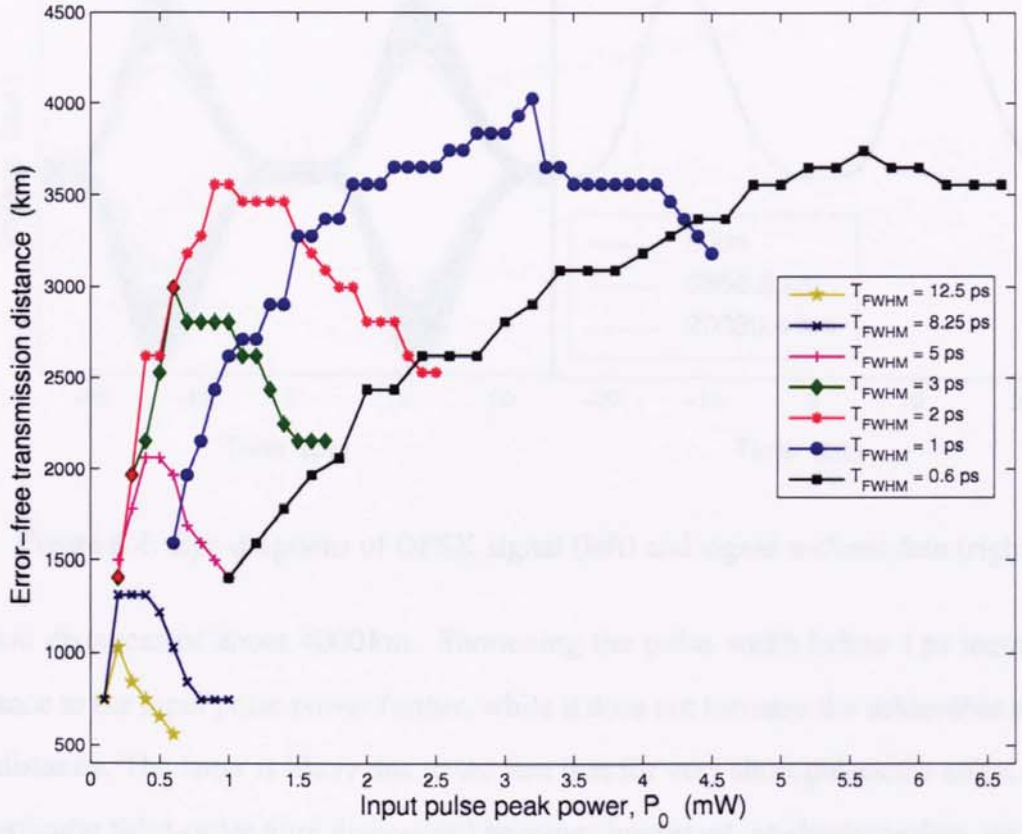

Figure 6.3: Maximum transmission distance versus input pulse peak power to the SOA.

The system performance is examined in terms of the maximum transmission distance corresponding to a linear Q-factor of more than 6. We use here the differential phase Q-factor as introduced in the previous chapter. The Q-factor is calculated at the input of the SOA, and is averaged over a number of pulse trains to account for more statistical realisations.

Figure 6.3 shows the maximum transmission distance as a function of the pulse peak power at the input of the SOA for different values of the pulse width. Note that the SOA operates in the saturation regime for the pulse parameters considered here. Pulsewidths $T_{\mathrm{FWHM}} = 12.5\,\mathrm{ps}$ and $T_{\mathrm{FWHM}} = 8.25\,\mathrm{ps}$ correspond to the standard $LiNbO_3$ Mach-Zehnder modulated RZ-DPSK pulse trains with the duty cycles of 50% and 33%, respectively. It is seen that the pulses with shorter duty cycles perform significantly better. It can also be seen that the signal power margins increase appreciably with decrease of the duty cycle. The best performance is achieved here with pulse widths of the order of 1 ps, which enable a trans-

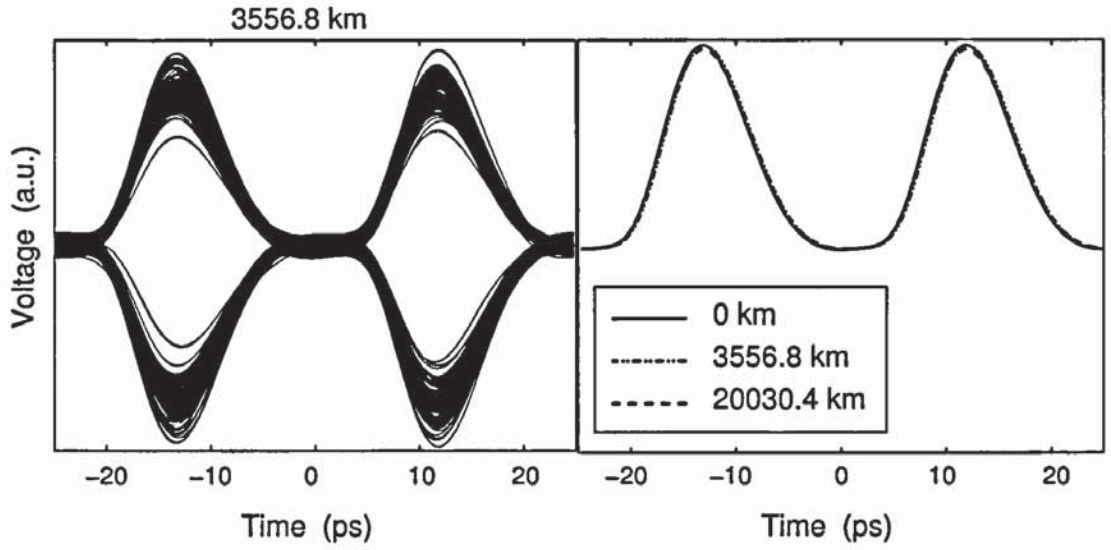

Figure 6.4: Eye-diagrams of DPSK signal (left) and signal without data (right).

mission distances of about 4000km. Shortening the pulse width below 1ps increases the tolerance to the input pulse power further, while it does not increase the achievable transmission distance. The latter is likely due to the fact that for very short pulses the effect of GVD (in particular third-order fibre dispersion) becomes important, as shorter pulses are effected by the dispersive effects more significantly than larger pulses, for an explanation see section 2.3.2 for details.

The left eye-diagram in Fig. 6.4 shows an example of the electrical signal eye-diagram taken at the maximum transmission distance. The electrical signal is filtered by a fifth-order Bessel filter with a (not optimised) cutoff frequency of 40GHz, and the eye is generated from a set of four simulations. The optical signal-to-noise ratio, calculated as the ratio of the average power of the "1" bits to the average power of the "0" bits of the demodulated OOK signal, is 10.6dB and 10.6dB at the input and output respectively (a minor difference between the input and output was observed, of the order ±0.05dB), of the last SOA travelled by the signal. The right eye-diagram in Fig. 6.4 shows the electrical eye-diagrams of the same signal when the DPSK data are not encoded at different transmission distances in the same system without ASE noise. One can see that there is no visible deviation of the waveform of the pulses over entire distance of at least 20Mm. This suggests that a robust quasi-periodic nonlinear propagation (soliton-like) regime does exist.

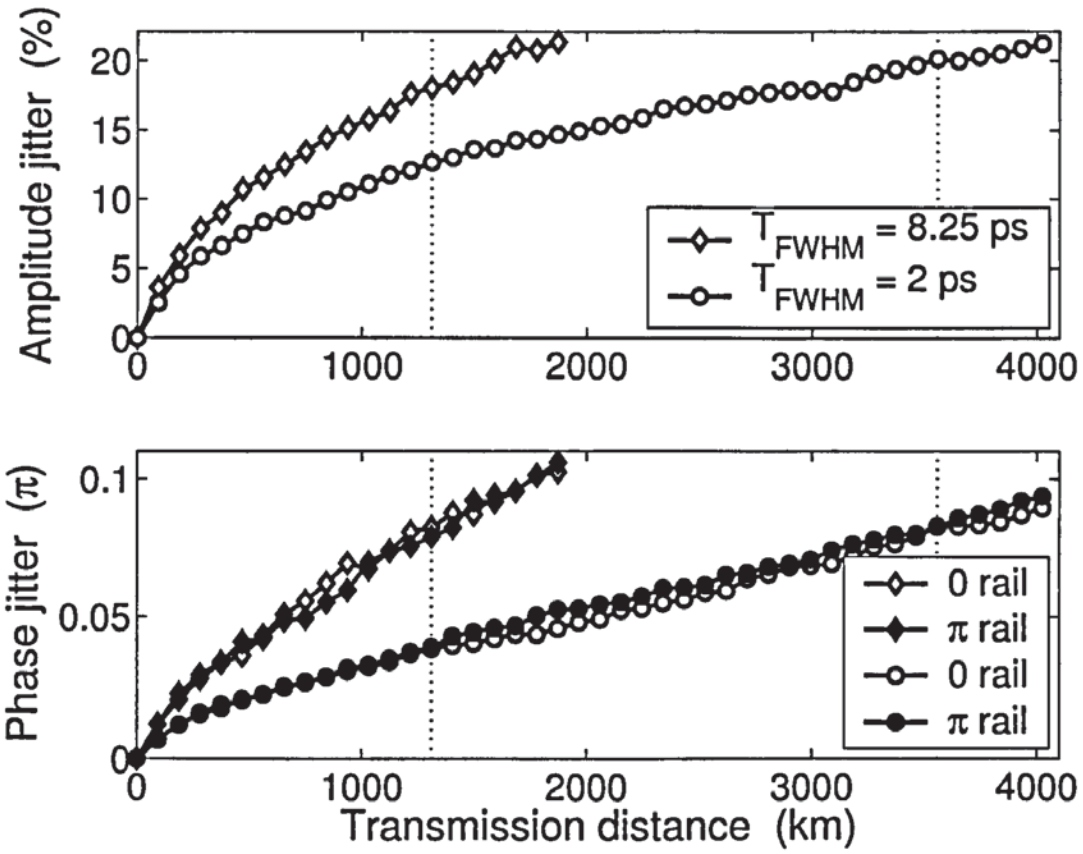

Figure 6.5: Amplitude jitter relative to the average pulse peak power of the signal and phase jitter versus transmission distance.

When the DPSK data are on and the ASE noise is taken into account, the system performance is primarily limited by the accumulation of phase noise. The nonlinear phase noise mainly results from conversion of amplitude noise from ASE, dispersion-induced pattern effects, and intra-channel nonlinearities to phase noise by SPM due to the fiber Kerr nonlinearity [108], whereas there is also a contribution from carrier density fluctuation in the saturated SOAs due to intensity noise [110].

The impact of the accumulation of amplitude and phase jitters on the system performance is evident from Fig. 6.5, where the root-mean-square (RMS) variations of the amplitude and phase are plotted versus the transmission distance. The pulse widths used in Fig. 6.5 are 2ps (circle) and 8.25ps (diamond).

This example corresponds to the optimum launch pulse peak powers for the used pulses. The amplitude jitter is calculated as the fluctuation of the pulse peak power of the optical data signal (i.e. the RMS variation of the peak power about the initial input peak power), and

the phase jitter is given by the fluctuations of the differential phase on the zero and π rails at the point of maximum opening of the differential phase eye-diagram (where the Q-factor is calculated). The jitters are averaged over a number of bit patterns and computed at the SOA input.

The evolution of the amplitude jitter indicates some saturation of the amplitude noise accumulation at long distances. After an initial transient of quicker growth, the accumulated phase noise stabilises on a linear growth with some constant slope. We notice that the existence of a soliton-like transmission regime in the system is responsible for the reduction of the growth of phase noise from a cubic increase with distance [108, 109] to the observed approximately linear growth.

An important question for the implementation of the proposed soliton-like DPSK 40 Gb/s transmission is the optimum dispersion-compensating scheme. We apply post-compensation of the dispersion at the maximum transmission distance for the case of zero residual dispersion. As an evaluation criterion, the Q-factor penalty is used. Figure 6.6 shows the Q-factor penalty versus the amount of the post-compensation for various pulse widths and the corresponding optimum launch peak powers. These results indicate that the full in-line dispersion compensation represents the optimum dispersion-compensating scheme for narrow pulses in the considered transmission system. Besides, as could be expected, for the shorter pulses the system performance is much more sensitive to the residual dispersion. Thus, the trade-off here is between a better performance in terms of transmission distance and more tighter requirements on the fine adjustment of the dispersion compensation. Quantitatively, the trade-off between these two factors is given by Figs. 6.3 and 6.6.

6.6 Soliton-Like DPSK Transmission at 80 Gb/s

In the previous section we demonstrated that the transmission performance of the DPSK systems is optimised by the use of short pulses. It is therefore natural to extend our analysis, to ultrahigh speed DPSK systems. Here, we perform simulation of 80 Gbit/s RZ-DPSK transmission.

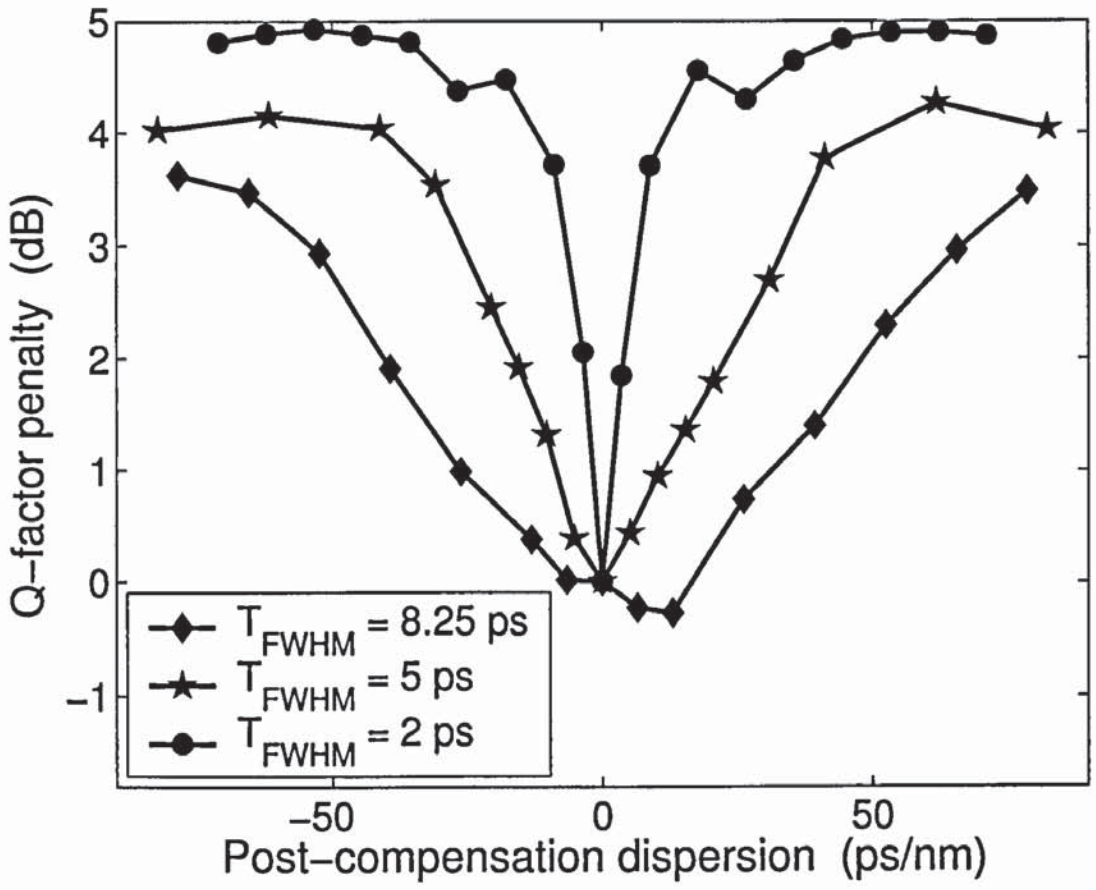

Figure 6.6: Q-factor penalty versus post-compensation dispersion.

We numerically transmit 128-bit DPSK random sequences formed with Gaussian pulses. As an example, we consider pulses with a FWHM duration of 2ps. The pulse width was chosen as a reasonable trade off between transmission performance and simulation speeds, as for shorter pulses require a higher resolution in the time domain (i.e. more number of points per bit slot, which results in larger memory requirements), and longer computational times.

The unsaturated gain of the SOA is chosen in accordance with the steady-state gain equation (6.3). A Gaussian filter is used as a receiver optical bandpass filter (OBPF) DEMUX, and a fifth-order Bessel filter with a (not optimised) cutoff frequency of 80GHz is used as a receiver electrical low-pass filter. The system performance is examined in terms of maximum transmission distance corresponding to a linear Q-factor of more than six. To take into account the contributions from both signal amplitude noise and phase noise as we vary the optical power levels in DPSK simulations, we choose here the smaller one from the am-

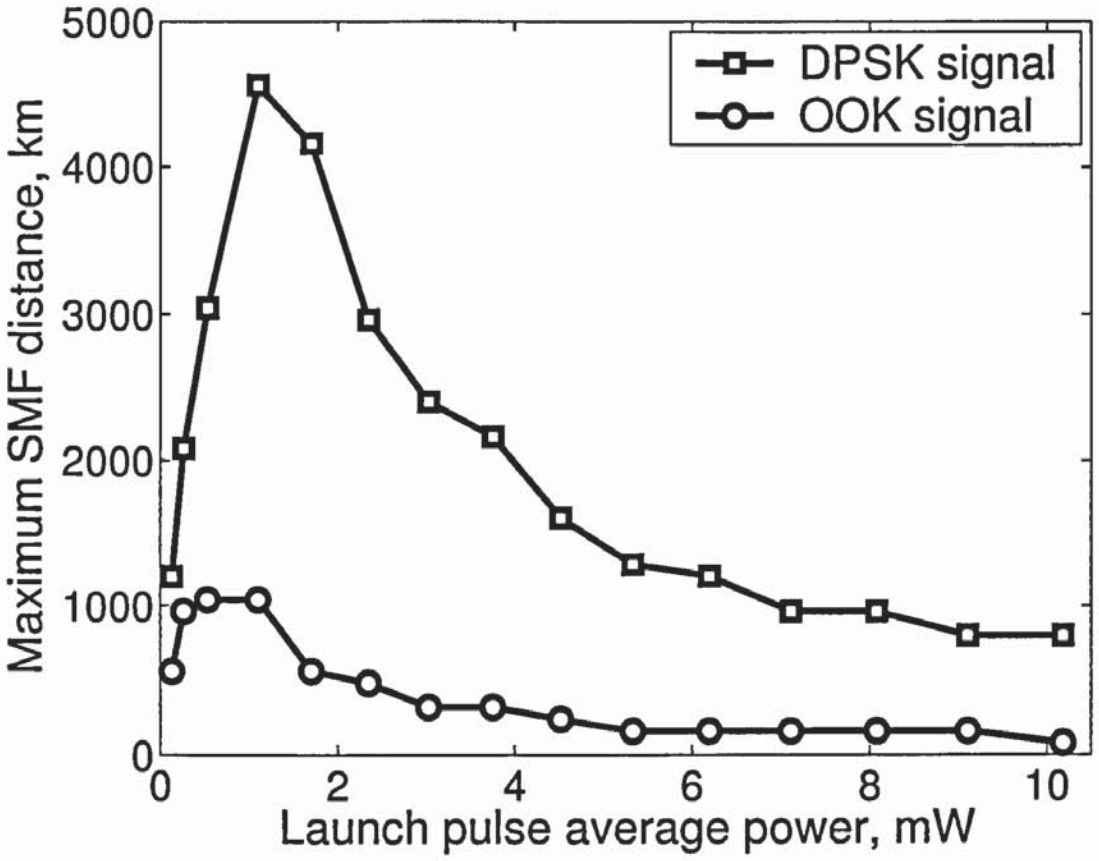

Figure 6.7: Maximum transmission distance versus launch pulse average power for 80 Gbit/s single-channel RZ-DPSK and RZ-OOK transmissions.

plitude Q-factor (Eq. (5.19)) and the differential phase Q-factor (Eq. (5.22)) as the overall Q for the performance estimation. The Q-factor is calculated at the input of the SOA, and averaged over a number of bit pattern realisations.

Figure 6.7 shows the maximum transmission distance as a function of the average power of the input signal pulses for single-channel transmission. In this example, a (not optimised) FWHM bandwidth of 220 GHz is used for the receiver OBPF. Note that the transmission performance of the 40 Gbit/s system described in the previous section, was evaluated without inclusion of signal optical filtering at the receiver. The performance results for an equivalent RZ-OOK signal transmission are also plotted in Fig. 6.7. The standard Q-factor of the received signal is used in OOK simulations. It is seen that for the considered system, the best OOK performance is achieved with launch pulse average powers in the range 0.5 mW to 1.1 mW, which enable a transmission distance of 1040 km of SMF (26 cascaded SOAs), whereas the attainable SMF distance is below 1000 km for all other launch powers. The

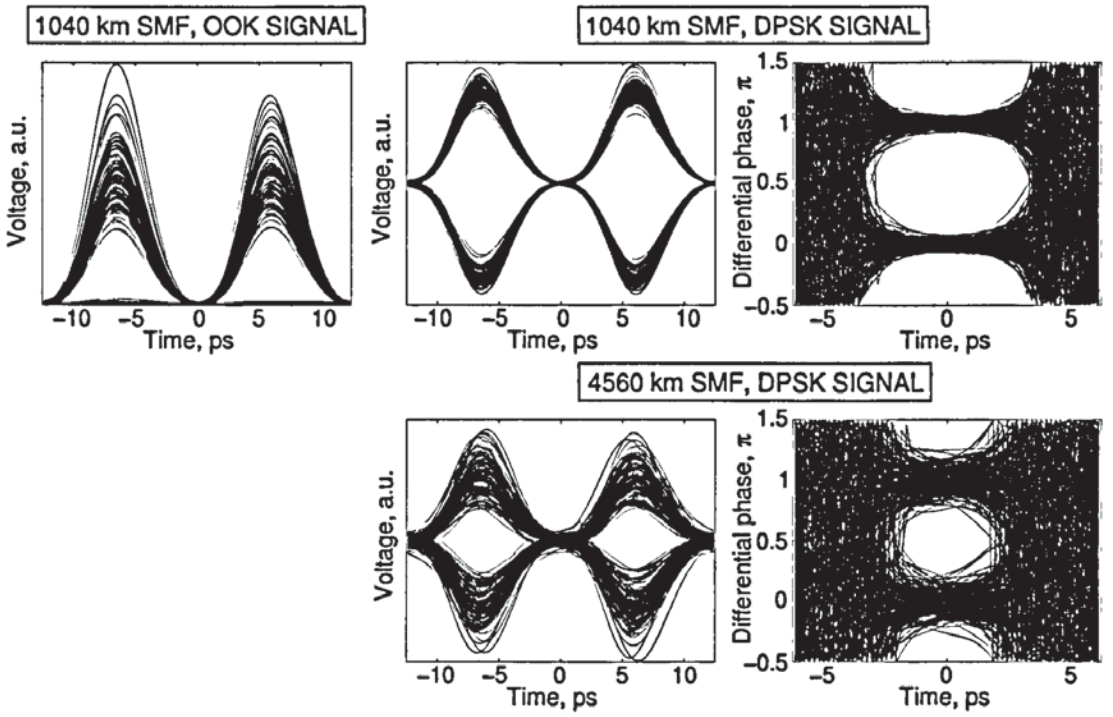

Figure 6.8: Eye-diagrams of the electrical OOK and DPSK signals and differential phase eye-diagrams of the DPSK signal for 80 Gbit/s single-channel transmission.

system performance is greatly enhanced by the DPSK format as a result of a significant reduction of the SOA-induced pattern effect. Here, the optimum launch pulse average power of 1.1 mW enables a transmission distance of 4560 km of SMF (114 cascaded SOAs), and SMF distances of 1000 km at least are possible for any average power between 0.1 mW and 10 mW. As expected, we observed in our simulations that the transmission performance is dominated by the amplitude Q-factor in the low power regime, whereas the effects of amplitude noise and phase noise are comparable at the intermediate power levels including the optimum power, and phase noise is the main limiting factor in the high power regime.

Figure 6.8 shows the eye-diagrams of the received OOK and DPSK signals and the differential phase eye-diagram of the DPSK signal at the maximum transmission distance for OOK, and the DPSK eye-diagrams at the maximum distance. This example corresponds to the optimum launch pulse average power of 1.1 mW. The eye-diagrams are calculated at the input of the SOA, and are generated from a set of five simulations. Severe pulse amplitude variation of the OOK signal is observed, which originates from the incomplete SOA gain recovery between succeeding pulses [114]. In contrast, DPSK shows only slight pulse-

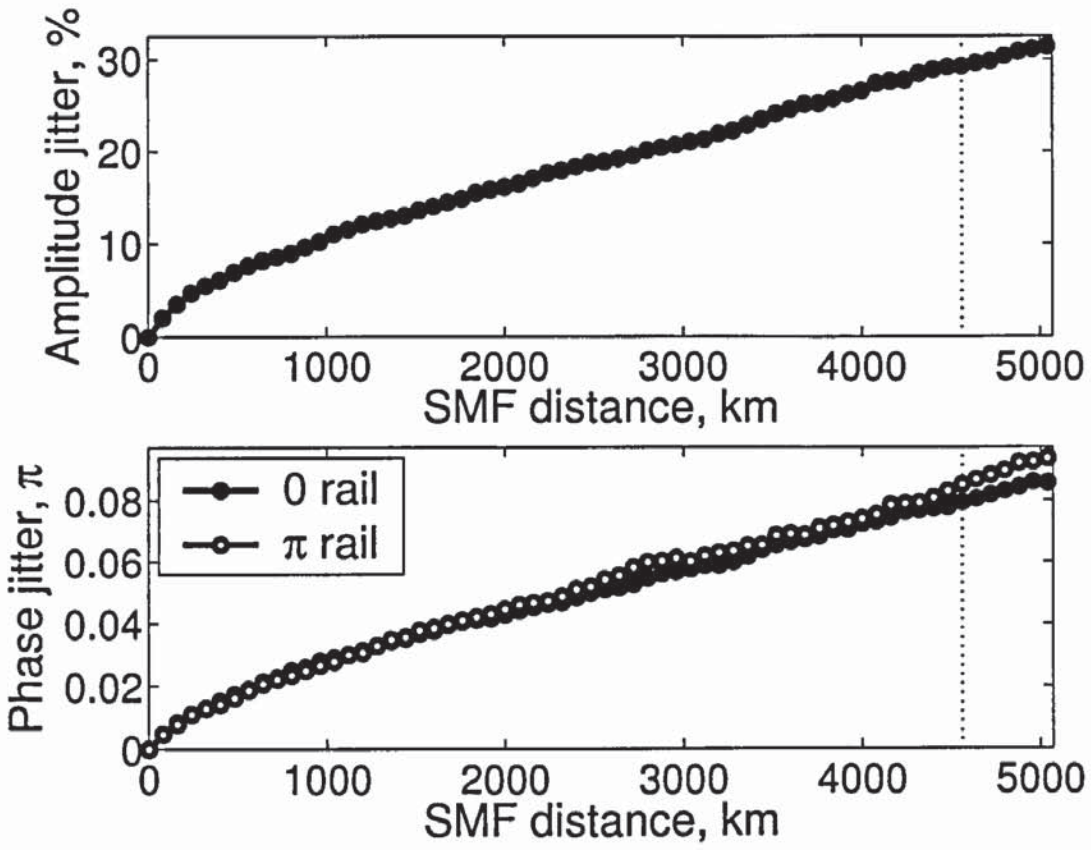

Figure 6.9: Amplitude jitter relative to the average pulse peak power of the signal and phase jitter versus transmission distance for 80 Gbit/s single-channel DPSK transmission.

patterning degradation in the received eye-diagram at the same distance. The differential phase eye shows a wide opening still at such a distance. The accumulated amplitude noise and phase noise through the system are responsible for the closure of the DPSK signal and phase eye-diagrams that is observed at the maximum transmission distance. It can be seen that at the considered power level, the two noise types contribute a roughly equal amount of degradation to the DPSK signal quality.

The impact of the accumulation of amplitude and phase jitters on the single-channel DPSK system performance is clear from Fig. 6.9, where the RMS variations of the amplitude and phase are plotted versus the travelled SMF distance. This example corresponds to the optimum launch pulse average power. The jitters are averaged over a number of bit patterns, and are computed at the SOA input. The evolutions of the two jitters show a similar pattern: after an initial transient of quicker growth, the accumulated amplitude and phase noises stabilise on a linear growth with some constant slope. The main feature that is again evident

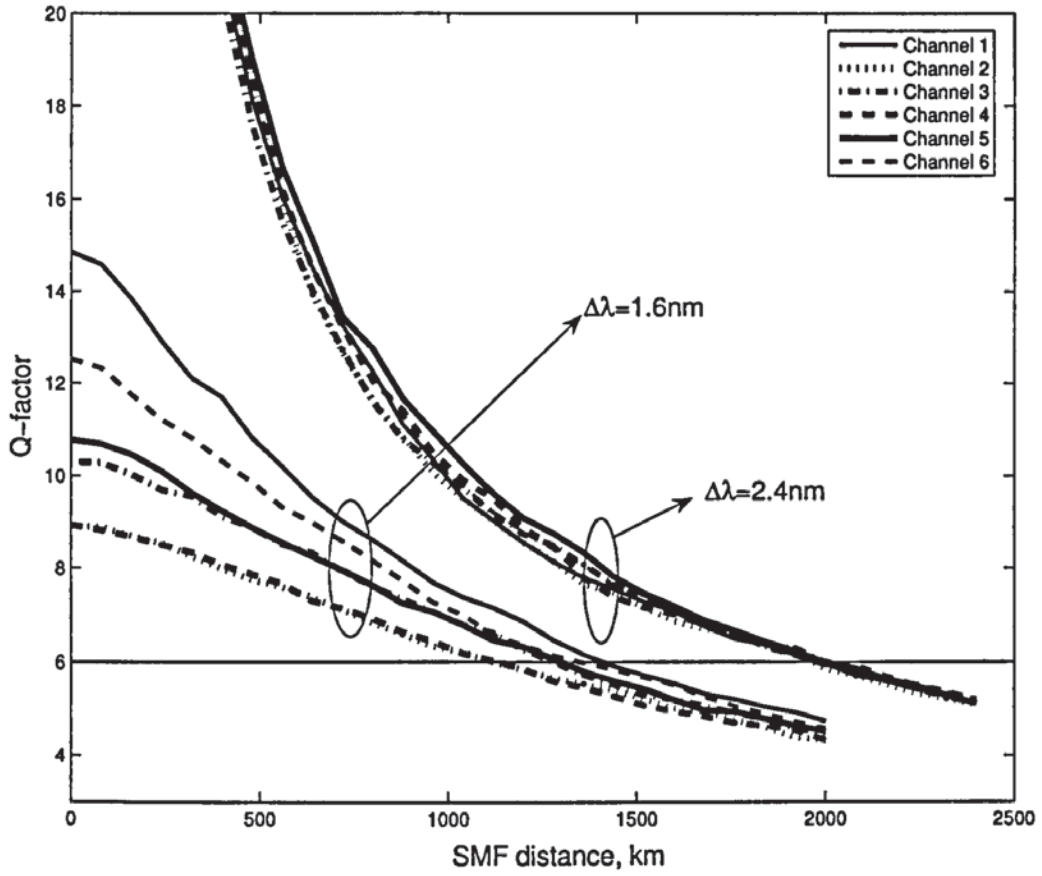

Figure 6.10: Q-factor versus transmission distance for 200 GHz- and 300 GHz-spaced 80 Gbit/s×6 WDM RZ-DPSK transmissions.

here is the growth reduction of the phase noise from a cubic increase with the distance [118] to the observed approximately linear growth, as a result of the existence of a "soliton-like" transmission regime in the system.

To illustrate the performance of the proposed RZ-DPSK transmission regime with WDM, we have performed numerical simulations of 480 Gbit/s (six channels at 80 Gbit/s) WDM transmission with channel separations of 200 GHz and 300 GHz. Figure 6.10 shows the evolution of the Q-factor of each wavelength channel over the transmission distance. In this example, the optimum launch pulse power for single-channel transmission is used, and the bandwidth of the DEMUX is set to 220 GHz in the case of a 300 GHz channel spacing, and is roughly optimised to 85 GHz in the case of a 200 GHz channel spacing. It can be seen that a transmission distance of more than 1000 km of SMF is possible for all channels

when 200 GHz-spaced channels are used, and the achievable SMF distance increases up to 2000 km for the larger channel separation. As expected, the WDM performance is worse than the single-channel performance, and this is due to inter-channel effects. However, comparing the WDM results with the results of single-channel OOK transmission in Fig. 6.7, it might be understood that the inter-channel crosstalk penalty resulting from the SOA cross-gain modulation is dramatically reduced for DPSK signals compared to OOK signals.

6.7 Conclusion

We first began our investigation of applying RZ-DPSK modulation format to a fibre optic transmission system based on SOA amplifiers by proposing a quasi-soliton regime could be found by minimising the quantity I/A, as quasi-solitons could be obtained through the iteration of fibre dispersion and nonlinear amplitude phase modulation produced by the action of lumped SOAs.

Using this information we simulated a fibre optic communication system at 40 Gbit/s. We demonstrated a proof of principle of the existence of a robust quasi-periodic nonlinear (soliton-like) transmission regime of RZ-DPSK signals using short pulses in high-speed systems with cascaded in-line SOAs. We again confirmed, as in Chapter 5, that RZ-DPSK produce optimum performance at shorter duty cycles. We achieved a transmission distance of approximately 4000km, using RZ-DPSK with a duty cycle of 0.04 and a transmission line consisted of lumped SOAs amplification.

We found the system performance to be limited by accumulation of phase noise. Which results from conversion of amplitude noise from ASE, dispersion-induced pattern effects, and intra-channel nonlinearities such as phase noise created by SPM, which is due to the fiber Kerr nonlinearity.

As we have found the RZ-DPSK modulation format tends to prefer short optical pulses, we naturally extended our analysis to ultra high speed optical transmission systems. We created simulations with lumped SOAs at the data rates of 80 Gbit/s, using both RZ-DPSK and RZ-OOK, so that we could compare the two formats.

We demonstrated that the RZ-DPSK system produced a near five fold increase in transmission performance when compared to RZ-OOK at 80 Gbit/s. We achieved transmission distance of approximately 4500km.

We futher extend our analysis of RZ-DPSK at 80 Gbit/s, with inline SOAs, to WDM application. We achieved a transmission distance of 1000km with a channel separation of 200GHz. This was increased to 2000km with a channel separation of 300Ghz.

Chapter 7

All-Optical 2R Regeneration of DSPK Transmission

In this chapter we present a concept for all-optical regeneration of signals modulated in phase-sensitive modulation formats (such as DPSK), which is based on a new design of RA-NOLM. We demonstrate simultaneous amplitude-shape regeneration and phase noise reduction in high-speed DPSK transmission systems by use of the RA-NOLM combined with spectral filtering.

7.1 Introduction

As previously emphasised the DPSK format, which carries the information in optical phase shifts of either zero or π between adjacent bits, offers a 3-dB improvement in receiver sensitivity compared to OOK, and an enhanced tolerance to dispersion and nonlinear effects. However, unlike the OOK signals, the DPSK signals are sensitive to phase noise, i.e. bit-to-bit phase fluctuation.

In DPSK transmission systems, linear phase noise is added by ASE from optical amplifiers. Moreover, intra- and inter-channel nonlinearities due to the Kerr effect in the fibre, such as SPM and cross-phase modulation, convert amplitude noise (variation of the signal amplitude) to phase noise. This is known as the Gordon-Mollenauer effect [127]. As a re-

sult, amplitude noise from ASE, dispersion-induced pattern effects, and nonlinearities such as the four-wave mixing, all introduce nonlinear phase noise that limits the system performance [128].

All-optical regeneration of DPSK transmission by low complexity and cost-efficient devices that can handle binary phase information would be an attractive technique to improve the performance of DPSK systems. Most of the regenerators studied so far have been designed to regenerate OOK signals without particular attention to preservation of the signal phase. An interesting technical solution for the phase regeneration has been recently proposed in [129]. Although ultimate regeneration of binary phase information may require phase-sensitive amplifiers [130–132], which are rather complex to be realised by the use of current technologies, regenerators that regulate the signal amplitudes with the phase information preserved (not regenerated) are expected to be useful [133–135].

The DPSK system performance can still be improved by in-line phase-preserving amplitude shape (2R) regenerators, because the employment of such devices suppresses the accumulation of amplitude noise and waveform distortion through the system and, correspondingly, limits the growth of phase noise.

All-optical 2R signal regeneration based on the fibre NOLM has shown excellent regenerative properties using OOK signals [136–139]. Furthermore, the NOLM regenerator uses a simple setup which, in its basic configuration, consists of an amplifier, a coupler, and a piece of fibre. The major problem when using traditional regeneration schemes based on the NOLM with signals using phase-encoding modulation formats is a strong conversion of the input signal amplitude jitter into phase jitter, since the conventional NOLM has a transfer function with a linear dependence of the output phase on the input signal power.

In [134], a modified NOLM was proposed, where directional attenuation enables maintaining the binary phase information, which is inherently degraded by the conventional NOLM.

In this chapter we will first review a simple NOLM configuration and then propose a phase-preserving all-optical 2R regeneration scheme for phase-encoded signals, which exploits a new design of NOLM based on distributed Raman amplification in a loop.

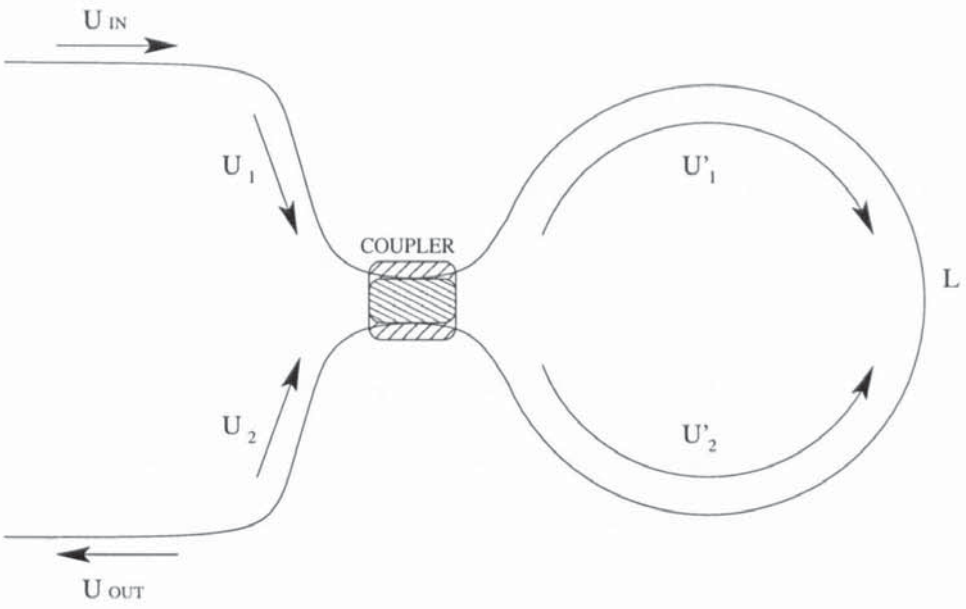

Figure 7.1: Scheme of the NOLM.

We furthermore demonstrate numerically that the combination of the RA-NOLM with narrow spectral filtering provides an additional phase limiting function in DPSK signal transmission, by suppressing the accumulated ASE-induced phase noise. As an example, but without loss of generality, we consider here a RZ-DPSK system operated at the 40Gb/s data transmission rate.

7.2 Basics of the NOLM

The principle operation of an NOLM is shown in figure 7.1. In this configuration we have a single input field U_{IN}, which is then incident on the coupler and is split into two counter propagating wave according to $\rho : (1-\rho)$, where ρ is the coupling constant. The two counter propagating waves U_1' and U_2' travel along the length of the fibre, L and recombine at the coupler to produce the final field U_{out}. In what follows is an analytical description of this process.

We begin by inserting an input field into a single port of the NOLM, U_{IN}. We then apply the following coupling equation [126], to obtain the two fields incident on the NOLM.

$$\begin{pmatrix} U_1 \\ U_2 \end{pmatrix} = \begin{pmatrix} \sqrt{\rho} & i\sqrt{1-\rho} \\ i\sqrt{1-\rho} & \sqrt{\rho} \end{pmatrix} \begin{pmatrix} U_{IN} \\ 0 \end{pmatrix} \tag{7.1}$$

The initial two initial fields U_1 and U_2 then propagate along the fiber, L. We however neglect any interaction between the two fields.

$$U_1 = U_{IN}\sqrt{\rho} \qquad U_2 = iU_{IN}\sqrt{1-\rho} \tag{7.2}$$

In order to obtain the two counter propagating waves, we need to solve equation 2.41, in the absence of linear dispersion effect. Thus equation 2.41 becomes,

$$i\frac{\partial U'_k}{\partial z} + i\frac{\alpha}{2}U'_K + \gamma|U'_k|^2U'_k = 0 \qquad k = 1,2. \tag{7.3}$$

where $k = 1,2$ donates the two fields. The solutions for equation 7.3 can be obtained [125] to give,

$$U'_1 = U_1 e^{i\gamma|U_1|^2 L_{eff}} \tag{7.4}$$

$$U'_2 = U_2 e^{i\gamma|U_2|^2 L_{eff}} \tag{7.5}$$

We now substitute the initial fields into the above solutions to arrive at,

$$U'_1 = \sqrt{\rho}U_{IN}e^{i\gamma\rho|U_{IN}|^2 L_{eff}} \tag{7.6}$$

$$U'_2 = i\sqrt{1-\rho}U_{IN}e^{i\gamma(1-\rho)|U_{IN}|^2 L_{eff}} \tag{7.7}$$

where the effective length, L_{eff} is defined as,

$$L_{eff} = \frac{1}{\alpha}\left(1 - e^{-\alpha L}\right) \tag{7.8}$$

After the two fields U'_1 and U'_2 propagate along the fibre, we need to recombined them at the coupler by using [126],

$$\begin{pmatrix} U_{OUT} \\ U_{REF} \end{pmatrix} = \begin{pmatrix} \sqrt{\rho} & i\sqrt{1-\rho} \\ i\sqrt{1-\rho} & \sqrt{\rho} \end{pmatrix} \begin{pmatrix} U'_1 \\ U'_2 \end{pmatrix} \tag{7.9}$$

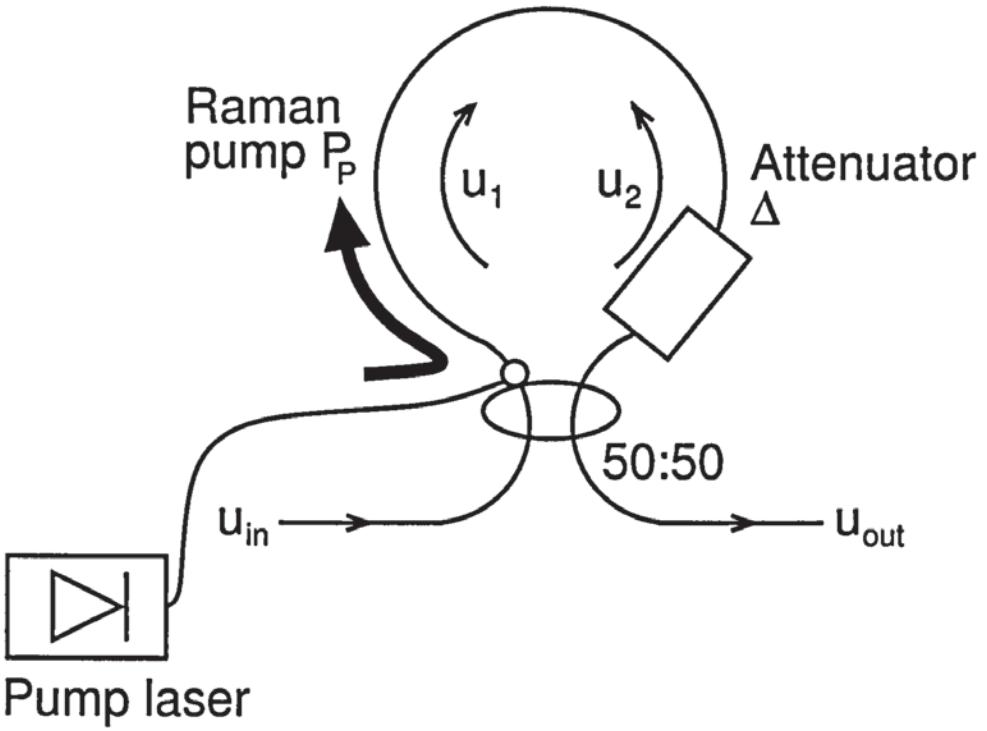

Figure 7.2: Scheme of the RA-NOLM.

In the above expression, we are not interested in the reflected field U_{REF} and hence the form of the outputted signal takes the form,

$$U_{out} = U_1'\sqrt{\rho} + iU_2'\sqrt{1-\rho} \tag{7.10}$$

We now substitute the solutions of U_1' and U_2', equations 7.6 and 7.7 into equation 7.10 to finally arrive at the final solution of the outputted field U_{out}.

$$|U_{out}|^2 = |U_{IN}|^2 \left\{ 1 - 2\rho(1-\rho)\left[1 + \cos\left(\gamma(1-2\rho)|U_{IN}|^2 L_{eff}\right)\right]\right\} \tag{7.11}$$

7.3 Operation Principle and Configuration of the RA-NOLM

The proposed design of RA-NOLM is depicted in figure 7.2. An incoming signal u_{in} is split into two partial signals, (by using a fibre coupler with a splitting ratio of 50:50) each with equal power levels,

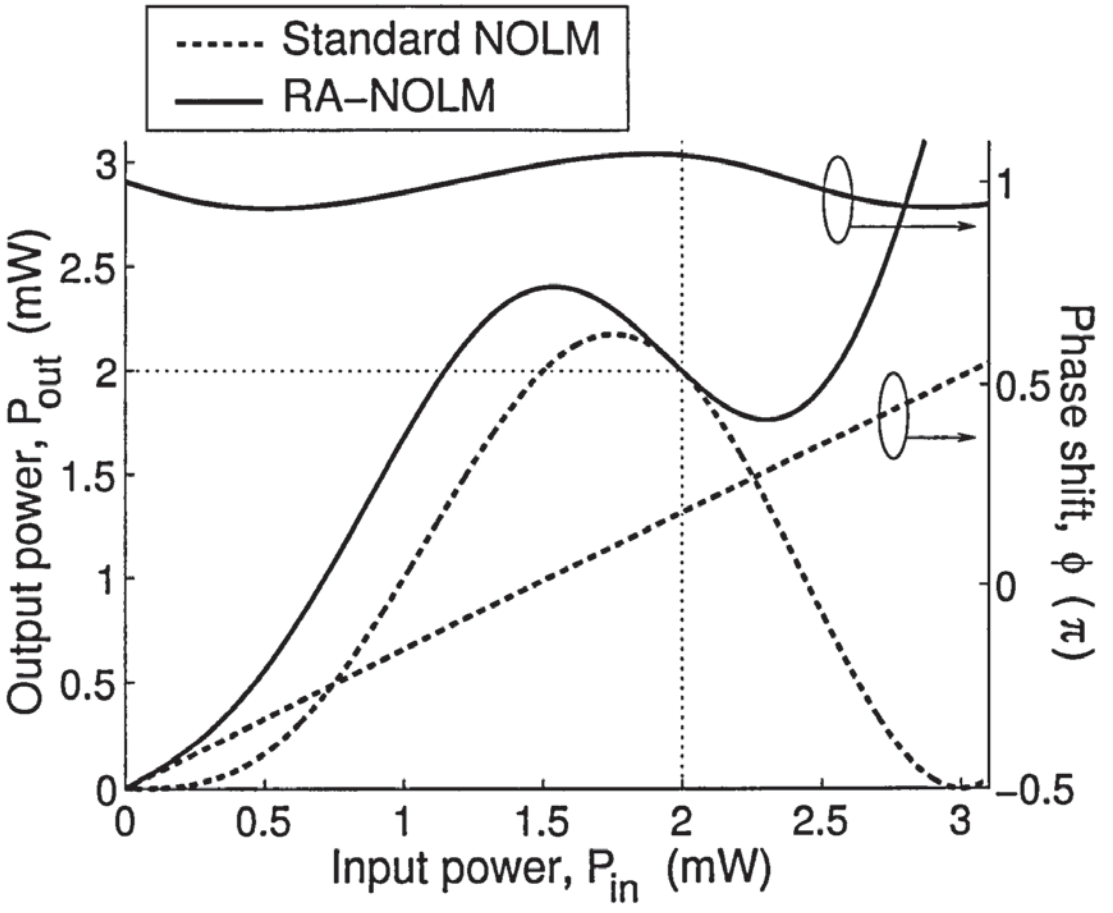

Figure 7.3: CW power and phase characteristics of the standard NOLM and the RA-NOLM.

$$u_1 = \frac{u_{\text{in}}}{\sqrt{2}}, \qquad u_2 = \frac{iu_{\text{in}}}{\sqrt{2}} \tag{7.12}$$

which counter propagate through a loop of fibre with distributed Raman amplification. Here and hereafter, indexes 1 and 2 refer to the respective clockwise and counterclockwise propagating signals.

The Raman pump is coupled into one end of the loop fibre immediately following the loop coupler. The clockwise-propagating signal is pumped co-directionally such that the gain decreases along the fibre, and attenuated by an attenuator after passing the fibre. The counterclockwise-propagating signal is attenuated before passing the fibre, and pumped counter-directionally with increasing gain along the fibre.

As a result of the different gains "seen" while propagating through the fibre in conjunction with the discrimination provided by the attenuator, the two signals gather different power levels and, thus, different phase shifts induced by the fibre Kerr nonlinearity through SPM

before they interfere at the coupler, according to

$$\begin{aligned} u_1 &= \sqrt{\frac{\Delta}{2}} u_{\text{in}} \exp\left(c_1 + \frac{i\gamma L_{\text{eff},1}|u_{\text{in}}|^2}{2}\right) \\ u_2 &= i\sqrt{\frac{\Delta}{2}} u_{\text{in}} \exp\left(c_2 + \frac{i\gamma \Delta L_{\text{eff},2}|u_{\text{in}}|^2}{2}\right) \end{aligned} \tag{7.13}$$

In (7.13), the effect of dispersion in the loop fibre is neglected, γ is the nonlinear coefficient of the loop fibre, Δ is the loss coefficient of the loop attenuator, and

$$\begin{aligned} c_{1,2} &= \int_0^L \mathrm{d}z\, g_{1,2}(z) \\ L_{\text{eff},1} &= \int_0^L \mathrm{d}z \exp\left[2\int_0^z \mathrm{d}z'\, g_1(z')\right] \\ L_{\text{eff},2} &= \int_0^L \mathrm{d}z \exp\left[2\int_z^L \mathrm{d}z'\, g_2(z')\right] \end{aligned} \tag{7.14}$$

with

$$\begin{aligned} g_1(z) &= -\alpha + g_0 e^{-2\alpha_{\text{P}} z} \\ g_2(z) &= -\alpha + g_0 e^{-2\alpha_{\text{P}}(z-L)} \end{aligned} \tag{7.15}$$

the loss-gain profiles along the propagation distance z. In (7.14) and (7.15), L is the length of the loop fibre, $\alpha = 0.05\ln(10)\rho$ and $\alpha_{\text{P}} = 0.05\ln(10)\rho_{\text{P}}$ are the fibre loss coefficients at the respective signal and pump wavelengths, with ρ and ρ_{P} in dB/km, and $g_0 = g_{\text{R}} P_{\text{P}}/(2A_{\text{eff}})$, where g_{R} is the Raman gain coefficient at the signal wavelength, A_{eff} is the fibre effective area, and P_{P} is the injected pump power.

The interference of the signals at the coupler

$$u_{\text{out}} = \frac{(u_1 + iu_2)}{\sqrt{2}} \tag{7.16}$$

yields the nonlinear power transfer function and phase characteristic

$$\begin{aligned} \frac{P_{\text{out}}}{P_{\text{in}}} \equiv \left|\frac{u_{\text{out}}}{u_{\text{in}}}\right|^2 &= \Delta \exp(c_1 + c_2) \\ &\times \{\sinh^2[(c_1 - c_2)/2] + \sin^2[\gamma(L_{\text{eff},1} - \Delta L_{\text{eff},2})P_{\text{in}}/4]\}, \\ \phi \equiv \arg\left(\frac{u_{\text{out}}}{u_{\text{in}}}\right) &= \gamma(L_{\text{eff},1} + \Delta L_{\text{eff},2})P_{\text{in}}/4 \\ &+ \arctan\{\coth[(c_1 - c_2)/2]\tan[\gamma(L_{\text{eff},1} - \Delta L_{\text{eff},2})P_{\text{in}}/4]\}. \end{aligned} \tag{7.17}$$

The combined action of differential Raman amplification and attenuation-unbalancing within the loop is responsible for an oscillatory behaviour of the induced phase shift ϕ around a mean value, whose variation with the input power decreases with decrease of Δ, for fixed loop length and fibre parameters. Here, we operate the NOLM such that the peak power $P_{0,\text{in}}$ of the input pulses is in the region past the first peak of the power characteristic. In this region, the NOLM provides negative feedback control of the pulse amplitude, which enables stabilisation of the pulse amplitude fluctuations [138].

We also require equalisation of the pulse peak power at the input and the output of the NOLM. We then obtain

$$\begin{aligned} \gamma(L_{\text{eff},1} - \Delta L_{\text{eff},2})P_{0,\text{in}} &= 2(1+\varepsilon)\pi, \qquad 0 < \varepsilon < 1, \\ e^{-(c_1+c_2)} &= \Delta\left\{\sinh^2\left[\frac{(c_1-c_2)}{2}\right] + \cos^2\left(\frac{\varepsilon\pi}{2}\right)\right\} \end{aligned} \tag{7.18}$$

from the first relation in (7.17). The solution of these equations for given $P_{0,\text{in}}$ and ε, and fixed fibre parameters and Raman pump, provides the values of the loop length L and loss coefficient Δ that minimise the variation of the induced phase shift with the input power. Note that further reduction of the phase shift variation could be achieved by incorporation of a post-amplifier into the NOLM setup. However, this would make the NOLM configuration more complex while yielding negligible performance improvement.

The power and phase characteristic curves according to (7.17) and (7.18) are plotted in figure 7.3. In this example, we considered a continuous-wave (CW) model, and assumed a dispersion-shifted fibre with $\gamma = 5.1\,(\text{W km})^{-1}$, $\rho = \rho_P = 0.3\,\text{dB/km}$, $P_P = 1\,\text{W}$, and $g_R/A_{\text{eff}} = 1.75\,(\text{W km})^{-1}$, a loop length of $L = 5.07\,\text{km}$, and an attenuation of $\Delta = 0.000164$ ($-37.8\,\text{dB}$). The CW power and phase characteristics of an equivalent conventional NOLM are also plotted for comparison. The standard NOLM is unbalanced with an asymmetrically placed in-loop attenuator, and pre-amplified by an optical amplifier to achieve input-output power equalisation (see [138] for details). Due to the fact that the NOLMs considered here both contain some form of optical amplification and/or attenuation, within the NOLM, we observe that the pulse is able to operate passed the switching curve (an imaginary 45° line that passes through zero). This creates a stable point in the NOLM's operation and is the point at which the power curve intersects the switching curve. If a pulse is injected into the

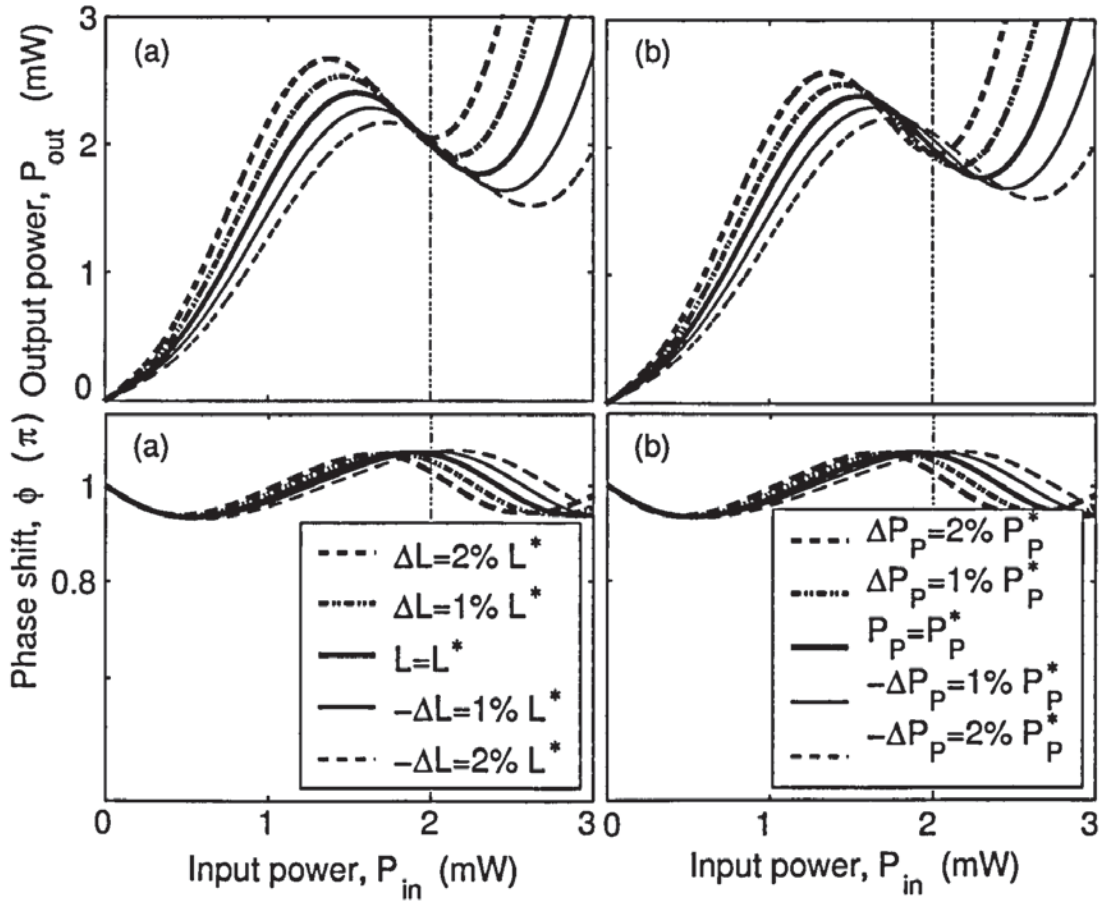

Figure 7.4: Power and phase characteristics of the RA-NOLM for variations in the loop length (left) and the Raman pump power (right).

NOLM, either side of this intersection, it will automatically be attracted to the stable point and ultimately preside there. For a more detailed description of this process consult [141].

From figure 7.3, we also note that the reduction of the phase shift variation with the input power in the RA-NOLM compared with the conventional NOLM is achieved at the expenses of a weaker discrimination of the low-power radiation against the higher-power signals.

Indeed, it can be easily shown by use of the demanded conditions on the NOLM operation (Eqs. (7.18) for the RA-NOLM) that both types of NOLM attenuate the low input powers P_{in} satisfying

$$\frac{P_{\text{in}}}{P_{0,\text{in}}} < 2\arcsin\left[\frac{\cos(\frac{\varepsilon\pi}{2})}{(1+\varepsilon)\pi}\right] \tag{7.19}$$

for fixed $P_{0,\text{in}}$ and ε.

However, while the conventional NOLM approximately cubes the low powers, the intensity of the filtering of the RA-NOLM is determined by the interplay between a linear term and a cubic term with P_{in} in the power mapping equation (see Eqs. (7.17)). Note also that,

due to the contribution of the linear term to the power mapping, an operational point on the power characteristic corresponding to the same ε as that for the conventional NOLM is, in general, less stable against fluctuations of the input power. This in general requires the use of bigger values of ε for the RA-NOLM, which in turn reduces the range of low powers that are attenuated by the regenerator.

In our calculations, the Raman gain of the loop fibre is varied by varying the loop length L to achieve the desired power and phase responses. Equivalently , one could vary the Raman pump power P_P at a fixed loop length. A rather fine tuning of the Raman gain is required for the operational conditions on the power (Eqs. (7.18)) to be met, whereas a variation in the Raman gain does not change the phase response significantly. Indeed, a deviation of ΔL or ΔP_P ($-\Delta L$ or $-\Delta P_P$) of the loop length or pump power from its nominal value L^* or P_P^* will only slightly affect the phase response in that it will cause a slight decrease (increase) of the amplitude of oscillations of the phase shift ϕ around its mean value. On the other hand , as it can be seen from Eqs. (7.17), the period of oscillations of both power and phase responses will shorten (lengthen).

As a consequence of the variation in the period of the power response, the operational point on the power characteristic will shift with respect to the first peak. Moreover, post-amplification (post-attenuation) of the NOLM will be required for input-output power equalisation. Note, however, that the sensitivity of the NOLM power response to the effective length of the NOLM loop is a common feature to any NOLM setup. An example of the tolerance of the RA-NOLM response to variations in the loop length and Raman pump power is given in Fig. 7.4, which shows the power and phase characteristics of the NOLM for a few deviations of L and P_P from their nominal values. The nominal loop length and pump power, as well as other parameters, are the same as those used in Fig. 7.3.

An illustrative example of the NOLM action on DPSK signals is given in Fig. 7.5, which shows the optical eye-diagram of a 40 Gb/s RZ-DPSK signal with a jitter of the amplitude at the NOLM input, and the eye-diagrams of the signal differential phase at the output of the standard NOLM and the RA-NOLM.

A signal eye-diagram is formed by superposing pulses corresponding to different time

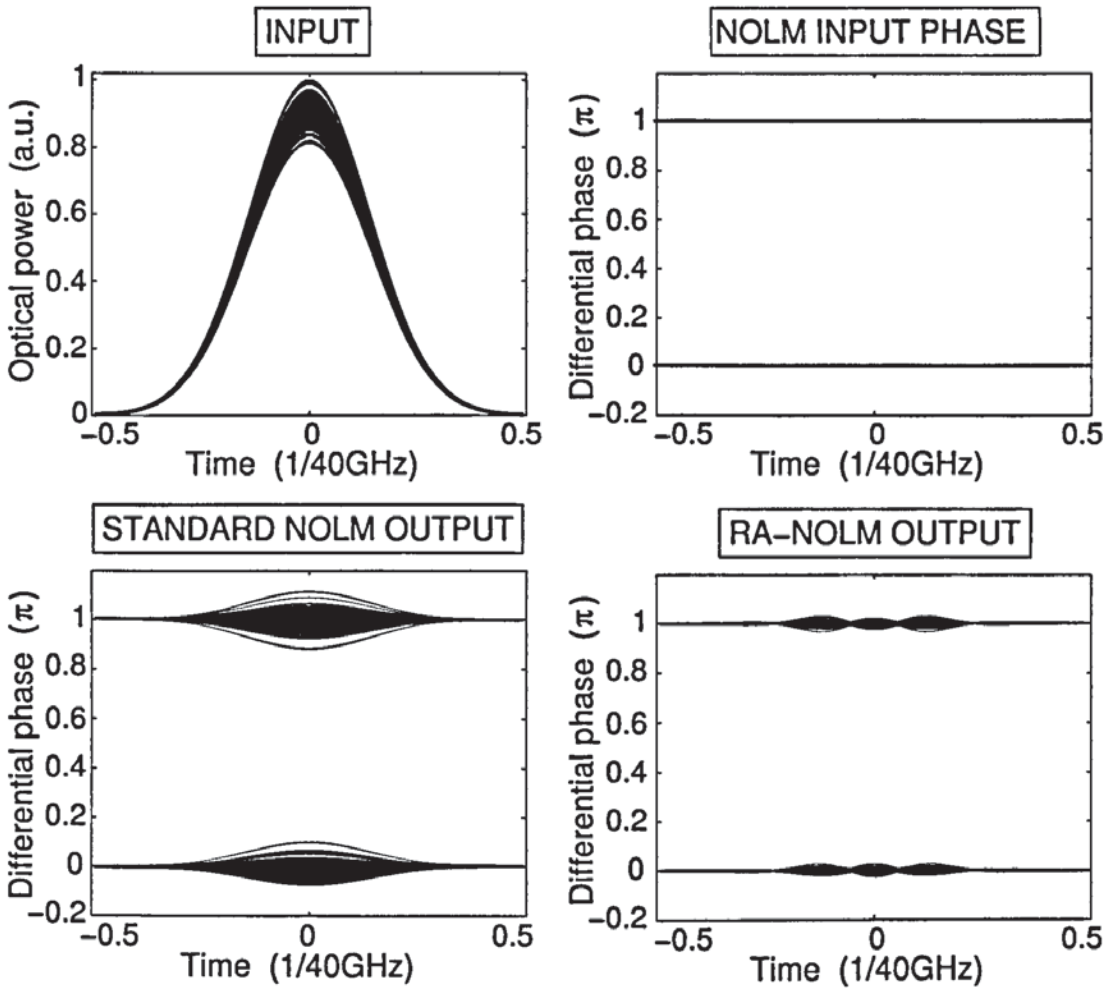

Figure 7.5: Eye-diagram of the optical input DPSK signal to the NOLM, and differential phase eye-diagrams of the output signal from the standard NOLM and the RA-NOLM.

slots on top of each other, and provides a visual indication of the power (amplitude variation) and timing (fluctuation of the pulse position in time) uncertainty associated with the signal. A differential phase eye-diagram overlays the phase difference between two succeeding pulses over the time slots covered by the signal and, thus, provides an indication of the phase uncertainty associated with a DPSK signal.

The amplitude jitter of the input signal to the NOLM in Fig. 7.5 is modelled by a superposed Gaussian-distributed random fluctuation of the pulse peak power. It is seen from Fig. 7.5 that the conventional NOLM converts the input power fluctuation into proportional fluctuations of the differential phase on the zero and π rails. This is due to the linear variation of the phase shift ϕ induced by the conventional NOLM with the input power (see Fig. 7.3). On the other hand, amplitude jitter causes only low excess phase jitter in the RA-NOLM.

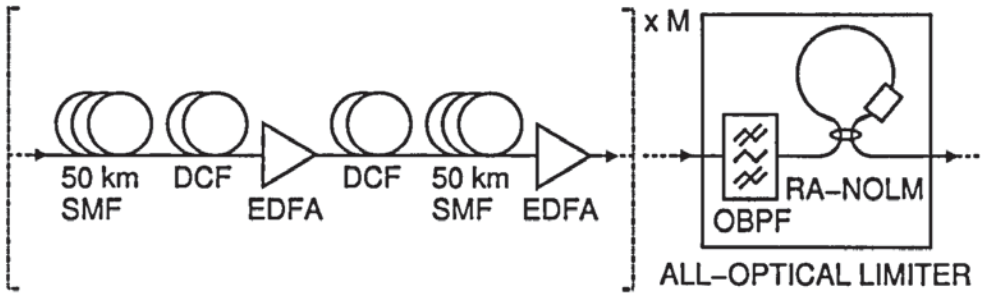

Figure 7.6: Setup of the transmission system.

Note that an existing phase jitter at the NOLM input is not reduced by the proposed NOLM setup.

7.4 Simulation of RZ-DPSK Transmission

Simultaneous amplitude regeneration and suppression of the phase noise growth is highly desirable for in-line DPSK signal processing. Combining the RA-NOLM with a narrow OBPF into an in-line limiter, it is possible to achieve 2R regeneration and substantial reduction of the accumulated phase noise simultaneously. Indeed, the RA-NOLM reshapes and stabilises the signal envelopes while inducing only a minor excess phase fluctuation. The stabilisation of amplitude fluctuations leads to reduction of the nonlinear accumulation of the phase noise caused by the amplitude-to-phase noise translation. The narrow filter provides a phase limiting function because it discriminates the ASE noise generated by in-line amplifiers from the signal and, thus, suppresses the ASE-induced phase noise (linear and nonlinear), which is proportional to the ASE noise power.

In this section, for illustration purpose, without loss of generality, simulation of a single-channel 40 Gb/s RZ-DPSK transmission is performed.

We model a transmission link composed of SMF spans of length 50 km and DCF spans as depicted in Fig. 7.6. The dispersion map consists of a SMF-DCF block and its mirror DCF-SMF block. The SMF has a dispersion of $D = 17\,\mathrm{ps/(nm\,km)}$, a dispersion slope of $D' = 0.07\,\mathrm{ps/(nm^2\,km)}$, a nonlinear coefficient of $\gamma = 1.4\,(\mathrm{W\,km})^{-1}$, and an attenuation of $\rho = 0.2\,\mathrm{dB/km}$. The parameters of the DCF are: $D = -100\,\mathrm{ps/(nm\,km)}$, $D' = -0.41\,\mathrm{ps/(nm^2\,km)}$,

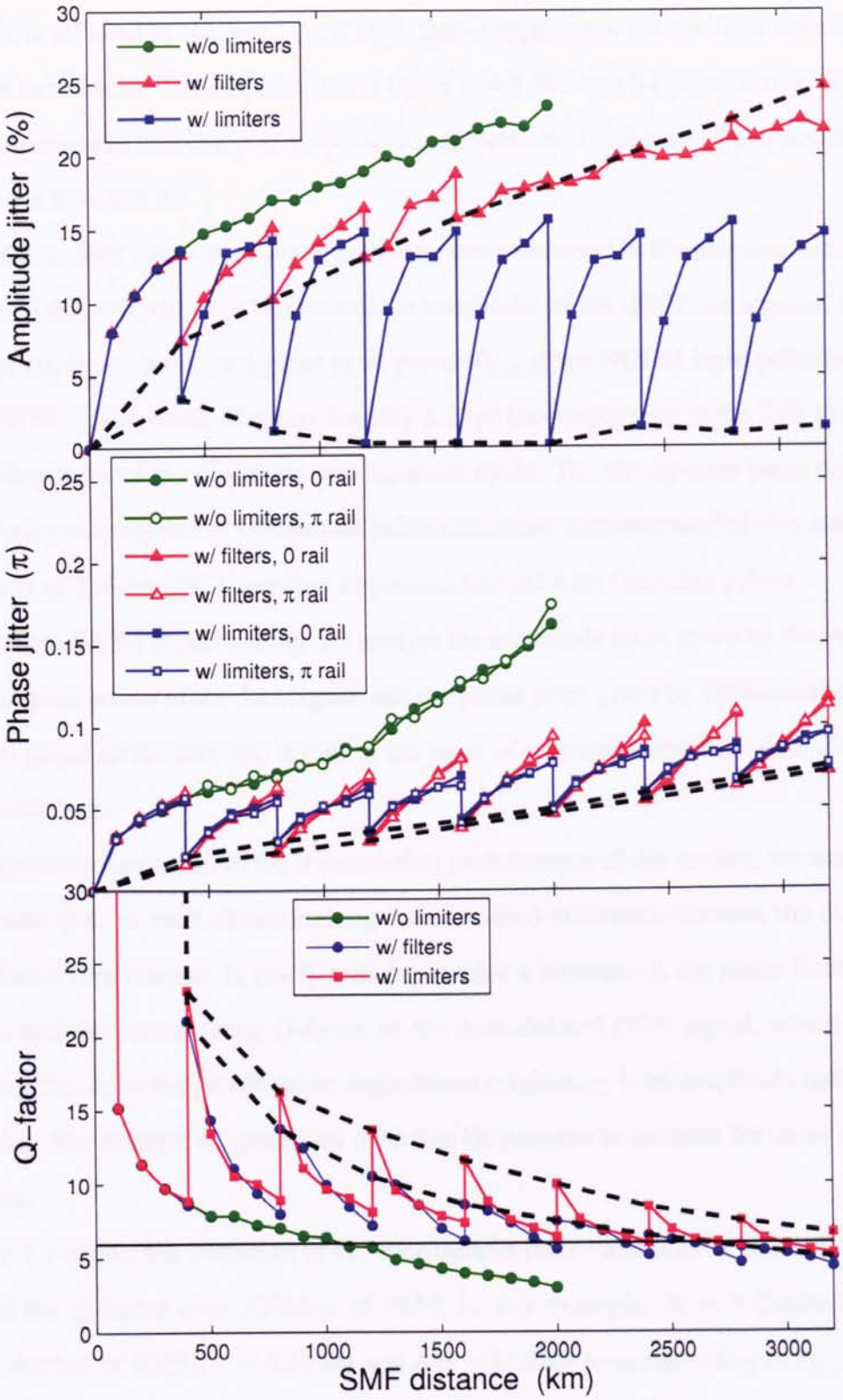

Figure 7.7: Amplitude and phase jitters, and Q-factor versus distance for 40 Gb/s RZ-DPSK transmission without use of limiters, with use of OBPFs, and with use of limiters (OBPF + RA-NOLM).

$\gamma = 5.8\,(\mathrm{W km})^{-1}$, and $\rho = 0.65\,\mathrm{dB/km}$. A residual (path-averaged) dispersion of 0.009 ps/(nm km) is allowed in the line. An EDFA that compensates for the fiber losses follows each of the two blocks. The amplifier noise figure is 4.5 dB. An all-optical limiter is inserted into the transmission line every M dispersion map periods. It consists of a Gaussian OBPF followed by a RA-NOLM.

The NOLM fiber parameters are the same as those assumed in the previous section. The gain of the EDFA preceding the limiter and the bandwidth of the OBPF are adjusted so that to provide the required operational pulse peak power $P_{0,\mathrm{in}}$ at the NOLM input point and a full-width at FWHM pulse width of approximately 8.25 ps (corresponding to the 33% duty cycle) at the starting point of the dispersion management cycle. The steady-state pulse parameters reached during propagation of continuous pulse sequences without encoded data are used for transmission of 256-bit DPSK random sequences formed with Gaussian pulses.

To characterise the signal quality, we analyse the amplitude jitter, given by the fluctuation of the pulse peak power of the data signal, and the phase jitter, given by the fluctuations of the differential phase on the zero and π rails at the point of maximum opening of the differential phase eye-diagram.

As a qualitative estimate of the transmission performance of the system, we use here the instantaneous (i.e., at each distance along transmission) minimum between the differential phase Q-factor (see chapter 5) [140], which provides a measure of the phase fluctuation in the signal, and the conventional Q-factor of the demodulated OOK signal, which accounts for the contribution to the performance degradation originating from amplitude noise and/or timing jitter. We average all quantities over five bit patterns to account for more statistical realisations.

Figure 7.7 shows the evolution of the root-mean-square variations of the amplitude and phase and the Q-factor over 3200 km of SMF. In this example, $M = 4$ (limiter insertion period of 400 km of SMF), $L = 5.15$ km and $\Delta = -37.9$ dB (corresponding to $P_{0,\mathrm{in}} = 2$ mW, $\varepsilon = 5/6$) for the NOLM, and the filter FWHM bandwidth is 139 GHz. The pulse average power is 0.93 mW (−0.32 dBm) at the launch point of transmission (input of the first SMF span within the dispersion map), corresponding to a peak power of 2.6 mW and a FWHM

pulse width of 8.4ps, and 0.092mW (−10.4dBm) at the input of the first DCF span within the dispersion map. Note that the launch pulse peak power i.e., the steady-state pulse peak power of a continuous, data-free pulse sequence propagating through the noiseless system at the limiter output) deviates from the peak power at the NOLM input, $P_{0,\text{in}}$. This is likely due to the pulse shaping that takes place within the arms of the NOLM loop. The evolutions of the RMS amplitude and phase variations and the Q-factor for RZ-DPSK signals transmitted through the system without limiters and the system with OBPFs only are also plotted in figure 7.7.

The same launch pulse parameters and filter bandwidth as those for the system with limiters are used. An extra gain is added to the amplifier prior to the OBPF to compensate for the energy loss introduced by the filter. It is seen that in the absence of limiters, there is an approximately linear increase in both the amplitude and phase jitters. As a result, the Q-factor decreases and drops below six, set as a limit, after 1000km of SMF.

For the system with OBPFs only, the filter action in discriminating the ASE noise from the signal results into a substantial suppression of the accumulated phase jitter at each filter location. However, although the effective rate of growth of the amplitude noise in the system keeps lower compared to the case without limiters because of some stabilisation of the pulse energy provided by the filter control, the system is eventually dominated by amplitude noise. This produces degradation of the Q-factor below six after approximately 2500km of SMF in the example of figure 7.7.

On the other hand, in the presence of limiters (OBPF + RA-NOLM), the accumulated amplitude jitter is almost completely suppressed at each limiter location by the amplitude regeneration action of the NOLM. Significant suppression of the accumulated phase jitter is also observed at each limiter location due to the filter action, although the strength of phase noise reduction is slightly lower compared to the case with filters only. The latter is due to the excess phase fluctuation introduced by the NOLM. Phase noise is the main limiting factor for such a system, but still at 3200km of SMF the accumulation of phase noise is not enough to produce degradation of the Q-factor below six. Thus we observe a significant improvement in transmission performance between the filtered and the limiter

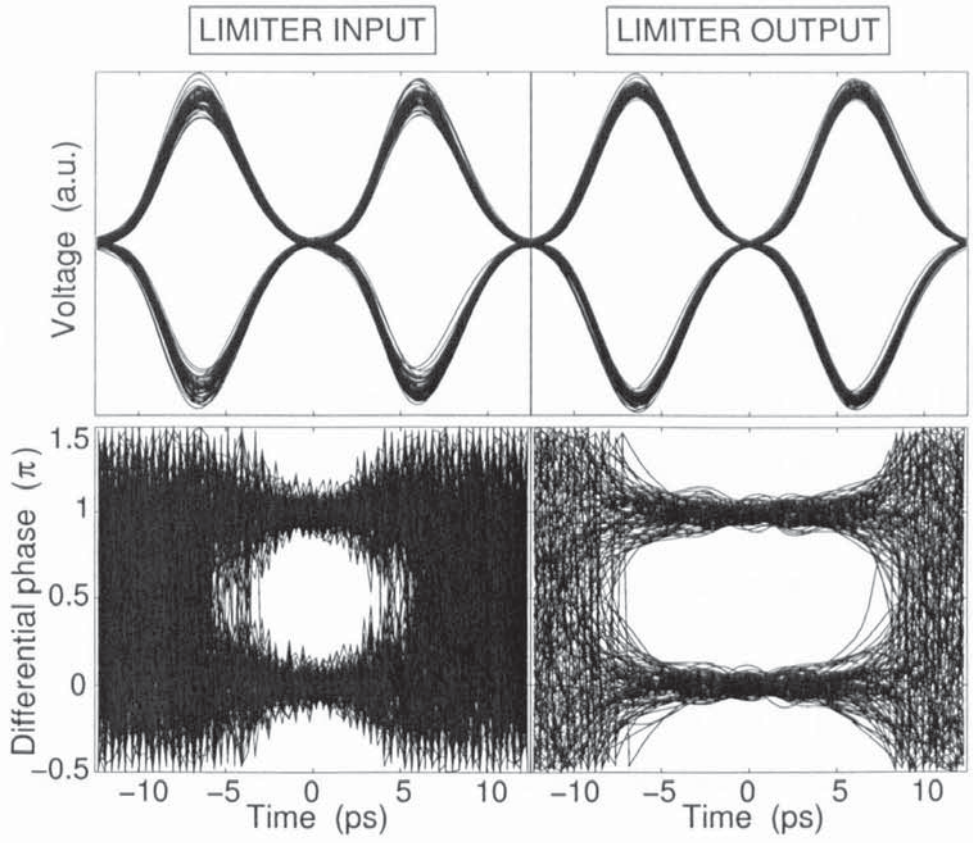

Figure 7.8: Electrical signal eye-diagrams and differential phase eye-diagrams before and after the limiter located at 1200km of SMF.

case, of approximately 700+km.

The regenerative capabilities of the limiter can be seen in figure 7.8, which shows the eye-diagrams of the electrical signal and the differential phase eye-diagrams at the input and the output of the limiter located at 1200km of SMF. The electrical signal is filtered by a fifth-order Bessel filter with a (not optimised) cutoff frequency of 40GHz.

7.5 Conclusion

In this chapter we investigated the regenerative properties of RZ-DPSK using a fibre based NOLM which could preform all optical 2R regeneration. A new design of a NOLM regenerator was present as traditional NOLM regeneration schemes display a strong conversion of the input signal's amplitude jitter into phase jitter, this is due to the fact that, they have a transfer function with linear dependence of the output phase on the input signal. The new NOLM configuration consisted of an attenuator and distributed Raman amplification, both

within the loop.

The new configuration displayed a reduction of the phase shift variation within the power of the RA-NOLM, as opposed to the conventional NOLM. Which allowed us to test its regenerative properties in a single channel 40 G/bit/s RZ-DPSK optic fibre transmission system.

The RA-NOLM presented phase-preserving DPSK signal regeneration properties and through numerical simulations, we demonstrated that the combined use of the RA-NOLM and optical filtering (as an in-line limiter), into a RZ-DPSK system provides simultaneous 2R regeneration and phase noise suppression. We showed a transmission distance of over 3200km. We were able to improve transmission distance by over 2000km for the case of no inline filtering and 700+km for a system with inline filtering.

The results indicate that regeneration of signals modulated in other phase-sensitive modulation formats such as duobinary coding or CS-RZ are possible as well.

Chapter 8

RZ-DPSK Dispersion Management

8.1 Introduction

In the later half of the 1990's, many 10Gbit/s OOK terrestrial WDM systems were deployed with fixed amplifier sites, to compensate for fibre loss, at distances non-uniformly spaced. Upgrades of these systems to 40 Gbit/s can be realised by switching modulation formats and carefully retuning the chromatic dispersion compensation. By making use of existing channel spacing, fixed SMF lengths and pre-set distances between amplifier sites, high performance and cost-efficient upgrades to 40 Gbit/s can still be achieved. An important practical issue then is how robust is transmission to inevitable variations in the dispersion mapping and how large is the margin when not-perfect dispersion management is applied. We would like to stress that this problem is quite different from optimisation of dispersion management for ultra-long haul or long-haul transmission link when periodic dispersion mapping can be done with a rather short period. The focus here is more on a reasonable trade-off between costs and performance rather than on achieving the optimal system performance.

In this chapter we numerically investigate various basic arrangements of dispersion management in an existing terrestrial link, with the aim of finding a cost effective solution with reasonably good performance. The system we consider is the 838 km terrestrial link as described in [142], which is typical of links between major European cities. RZ-DPSK modulation format is used throughout the chapter. Large-scale numerical simulations of several

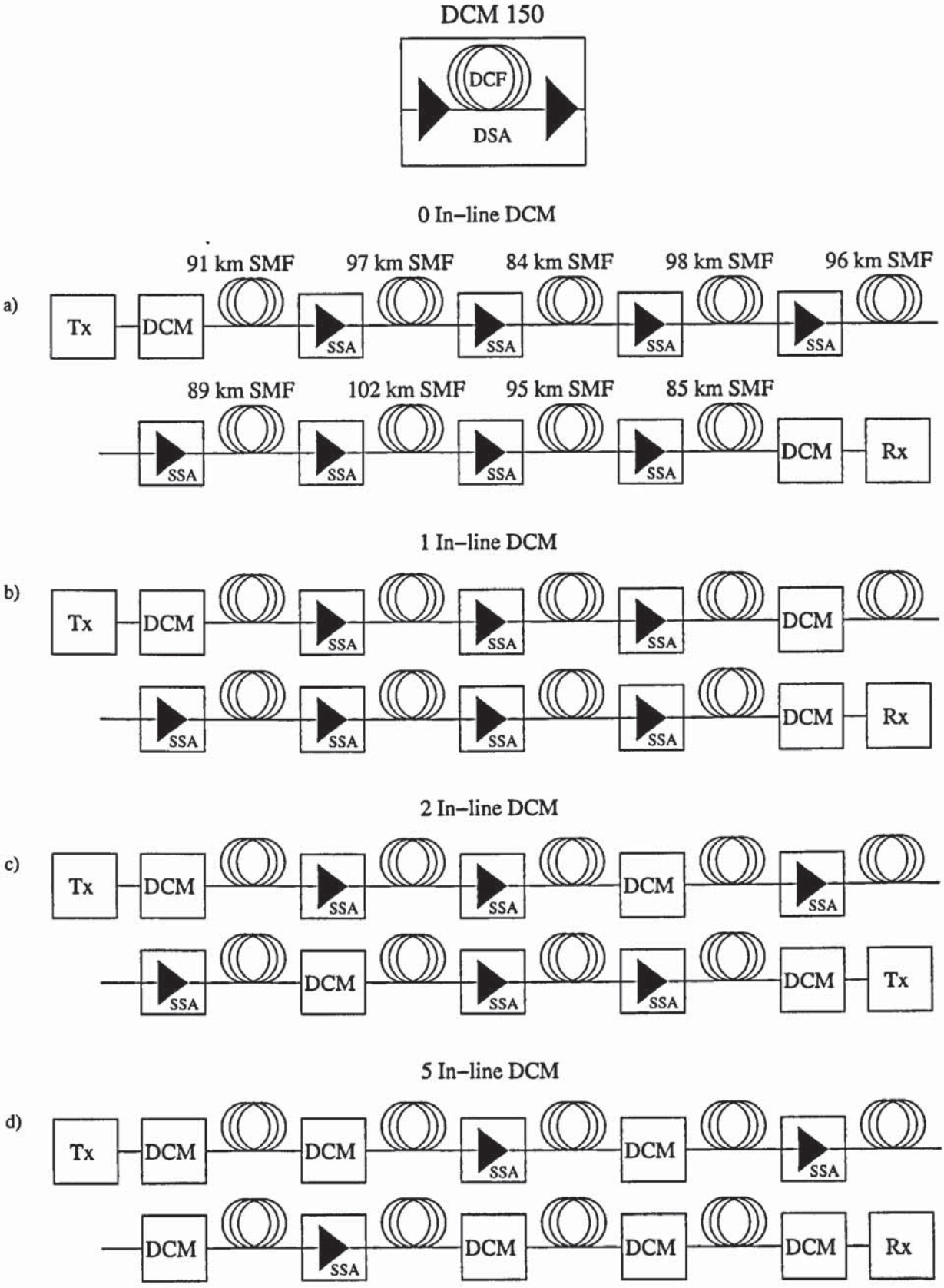

Figure 8.1: Schematic diagram of target terrestrial link, a) no DCM-150, b) 1 DCM-150 located at site 5, c) 2 DCM-150's located at sites 4 and 7, d) 5 DCM-150's are located at sites 2, 4, 6, 8 and 9.

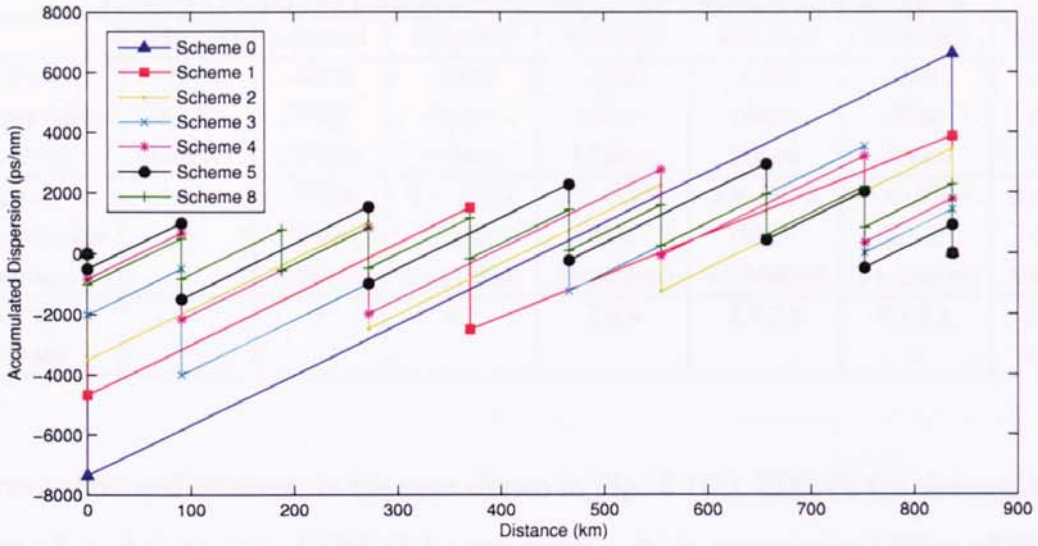

Figure 8.2: Dispersion maps corresponding to different numbers of DCM nodes.

basic dispersion mapping schemes have been performed in order to establish the margins when using not the most efficient dispersion compensating configurations for the target system. Our main objective is to study the effects of concentrating the Dispersion Compensation Modules (DCMs) at specific points along the dispersion map - lumped mapping (compare to [142, 145], as opposite to deploying a larger number of smaller (DCMs) placed periodically along the map.

Reduction of the number of in-line DCMs leads to a minimisation of the overall system cost. We consider here DCMs, which consist of erbium-doped dual-stage repeaters incorporating Dispersion Compensating Fibre (DCF) in the midstage. Since a Single Stage Amplifier (SSA) is 30% less expensive than a Dual Stage Amplifier (DSA) and decreasing the number of amplifiers reduces the risk of pump failures, we looked to employ the simplest dispersion management configuration with the minimal number of DCMs.

8.2 System Configuration

The 838km installed terrestrial system under investigation is schematically depicted in figure 8.1. The transmission line consisted of ten nodes, which are non-uniformly spaced between

Table 8.1: Optimal parameters of dispersion management schemes.

	Scheme0	Scheme1	Scheme2	Scheme3	Scheme4	Scheme5	Scheme8
Pre-compensation (ps/nm)	-7348 (SMF 440km)	-4676 (SMF 280km)	-3507 (SMF 210km)	-2004 (SMF 120km)	-1503 (SMF 90km)	-501 (SMF 30km)	-1169 (SMF 70km)
Inline compensation (ps/nm)	–	-4008 (SMF 240km)	2×-3507 (SMF 2×210km)	3×-3507 (SMF 3×210km)	4×-2672 (SMF 4×160km)	5×-2505 (SMF 5×150km)	8×-1336 (SMF 8×80km)
DCM Nodes	–	5	4,7	2,6,9	2,4,7,9	2,4,6,8, 9	2,3,4,5, 6,7,8,9

the transmitter and receiver. In the case shown in Fig. 8.1(d), EDFA's are situated at nodes 3, 5 and 7, and five in-line DCM-150 components (which compensate 150km of SMF) are situated at nodes 2, 4, 6, 8, and 9. The SMF G.652 fibre parameters at 1550 nm are: D = 16.7 ps/nm/km, Slope = 0.06 ps/nm2/km, Aeff = 80m2, Loss = 0.22dB/km. The DCMs consist of slope matched DCF fibre surrounded by dual stage EDFAs, with an insertion loss of 10dB. The EDFA's noise figure is 4.5dB.

Removing DCMs and replacing them with EDFAs, and vice versa, creates many combinatoric ways to implement the dispersion management. We will use the following notations. We consider different schemes with indices k where $k = \{0,1,2,3,4,5,8\}$ denotes the number of DCMs deployed in-line at sites 2 to 9. Nodes 1 and 10 are the pre-compensation (DCM-pre) and post-compensation (DCM-post) modules, respectively. Figure 8.2 shows a regular map of the dispersion management (scheme 8), and the other six configurations where the DCMs are lumped together at specific nodes.

8.3 Results and Discussion

We numerically transmit either a single channel or 8 WDM channels (100 GHz channel separation) of 40Gbit/s RZ-DPSK signal consisting of 1024 random bits formed with 50% duty cycle Gaussian pulses. The input peak power, DCM-pre, and DCM in-line parameters were simultaneously optimised. The DCM-post was calculated such that the residual dispersion would be close to zero. Then DCM-post was tuned to the maximise Q-factor. The Q-factor

Table 8.2: Normalised cost of system components DCM-150, DSA and SSA.

Number of DSAs	10	9	8	7	6	5	4	3	2
Number of SSAs	0	1	2	3	4	5	6	7	8
Total Cost	35.5	34.5	33.5	32.5	31.5	30.5	29.5	28.5	27.5
Relative	1.00	0.97	0.94	0.92	0.89	0.86	0.83	0.80	0.77

was measured by using the differential phase technique as introduced in Chapter 5.

To account for statistical variations we have averaged the results over 10 runs following the procedure used in [144]. As a result of massive multi-parametric optimisation we have determined the optimal parameters for each of the considered lumped mapping schemes as presented in Table 8.1.

For each scheme the optimal input signal peak power turns out to be approximately 5dBm, while the optimal pre-compensating dispersion, in-line dispersion corresponding to the chosen scheme and the location of the DCMs for each configuration are listed in Table 8.1. Figures 8.3(a)-8.3(b) illustrate the tolerance of the system performance to variations in the peak power 8.3(a) and pre-compensation 8.3(b). Not surprisingly the worst performing scheme has no in-line DCMs where all the dispersion compensation is split between the DCM-pre and DCM-post modules only. Most important, for $<$ 1dB Q-penalty compared to the optimal dispersion mapping, scheme 1 is an attractive solution due to low inventory costs. Figures 8.4(a)-(g) show the Q-factor (dB) topology of DCMpre (ps/nm) versus peak power (dBm) for each dispersion map.

We extend our results through numerical simulations of 8 $\times$ 40 Gbit/s WDM channels spaced 100 GHz apart and centred around 1550 nm with the best dispersion maps identified from the single channel simulations. We concentrated our efforts to the cases of 0, 1 and 5 in-line DCMs. We have found only 0.5 dB Q-penalty is imposed in WDM system compared to single channel transmission.

It is interesting to estimate the possible effect of lumped dispersion mapping in terms of cost reduction. Table 8.2 shows the normalised relative cost of dispersion management components. Here, we estimated the cost of the SSAs and DSAs to be approximately 2x and 3x the cost of a DCM-150, respectively. It can be seen from the Table 8.2 that implementing

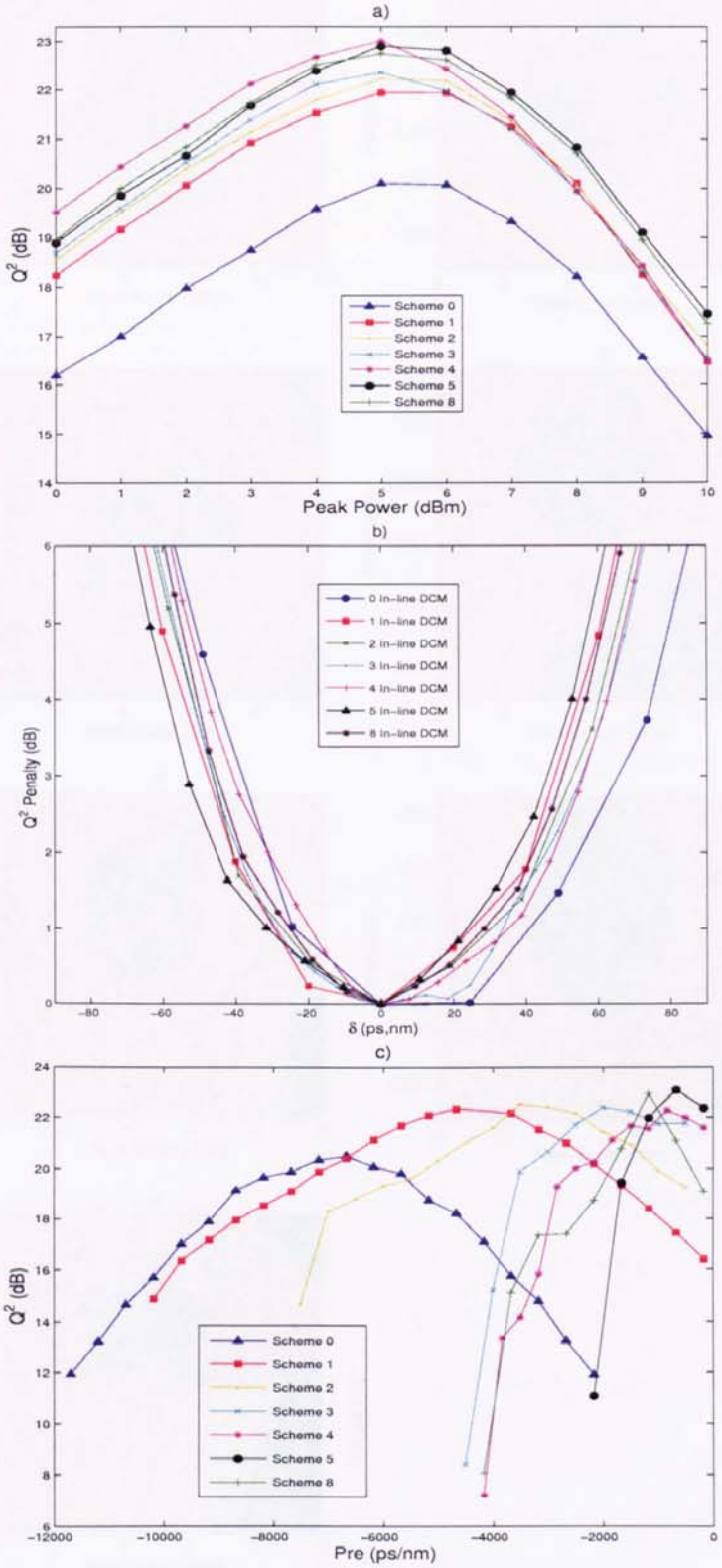

Figure 8.3: (a) Q-factor versus peak power for optimal dispersion management schemes, (b) Q-factor penalty versus pre-receiver detuning, (c) Q-factor versus DCM-pre with optimum peak power and in-line DCMs.

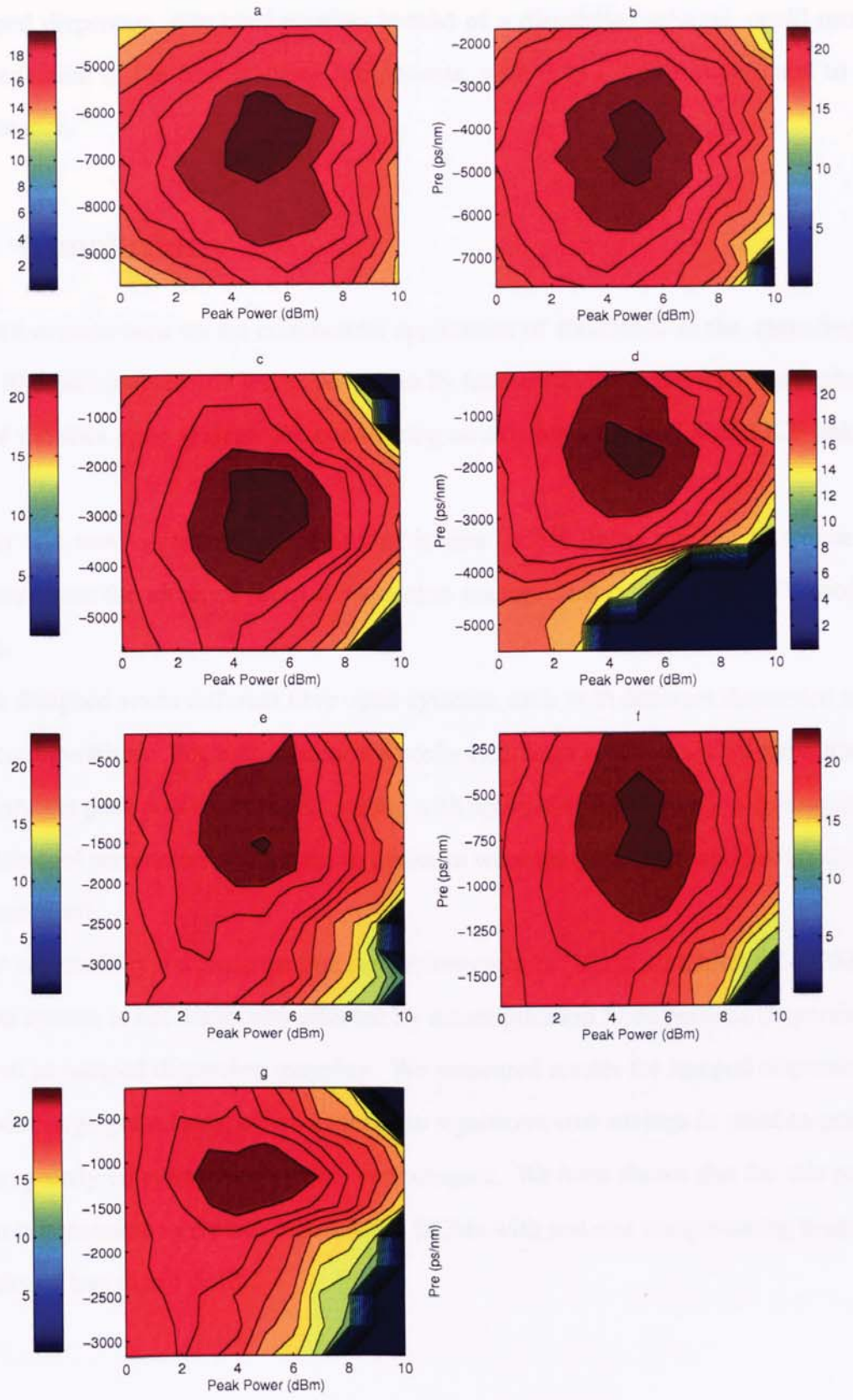

Figure 8.4: Optimisation results displaying the correlation between input peak power and dispersion compensation placed at DCM-Pre, for the following system configurations: a) Scheme 0, b) Scheme 1, c) Scheme 2, d) Scheme 3, e) Scheme 4, f) Scheme 5, g) Scheme 8.

a lumped dispersion map configuration instead of a distributed scheme, could result in a 20% reduction in the cost of these components, with only a small impairment to system performance.

8.4 Conclusions

Here we concentrated on the commercial application of RZ-DPSK in the upgrading of existing 10 Gbit/s links to 40 Gbit/s. We primarily focused on the relative cost to performance ratio of the fibre optic system. We considering an existing terrestrial SMF/DCF link of 838 km.

Our aim was to reduce the number of in-line DCMs (in an attempt to reduce costs), and investigate the effect of lumped dispersion management on the RZ-DPSK modulation format.

We designed seven different fibre optic systems, each with different dispersion management configurations. For each system we preformed large scale numerical simulations and optimised the peak power of the pulse along with optimising the dispersion management (i.e. the additional parameters we needed to optimise were the pre-, post- and in-line dispersion compensation).

We successfully demonstrate that the performance of WDM 40 Gbit/s RZ-DPSK transmission system is not drastically affected by reconfiguration from periodic dispersion management to lumped dispersion mapping. We presented results for lumped dispersion mapping with large granularity, offers a means to significant cost savings in point-to-point links without greatly compromising system performance. We have shown that for this particular system it is possible to replace 5-8 existing DCMs with just one compensating module with a penalty of less than 1.5 dB.

Chapter 9

Conclusion

This thesis has presented the results of large scale numerical investigations into various modulation formats, including RZ-OOK, CS-RZ, RZ-DPSK and applied them to 40Gbit/s DWDM fibre optic communication systems. We then primarily focussed on RZ-DPSK, and considered it in conjunction with photonic devices. Finally we considered the effects of dispersion management on RZ-DPSK in order to provide a cost effective upgrade form 10Gbit/s to 40Gbit/s fibre optic systems.

Chapter 1 provided a brief overview of the historical development of optical fibre communications systems and introduced the three modulation formats, RZ-OOK, CS-RZ and RZ-DPSK.

In Chapter 2 the theory of optical pulses propagating along the fibre is reviewed. We derived the NLSE, which governs the propagation of optical pulses. We give an overview of linear (optical attenuation and group velocity dispersion) and nonlinear effects (the Kerry effect, SPM and XPM) which influence the propagation of optical pulses along the optical fibre and the terms associated with the NLSE. We then presented the fundamental solition solution of the NLSE. We then proceeded to incorporate, analytically, the effect of periodic optical amplification to the NLSE by introducing optical noise. Three of the final four sections of this chapter are associated with the practical generation and detection of the modulation formats investigated within this thesis, namely RZ-OOK, CS-RZ-OOK and RZ-DPSK. Finally the last section unaccounted for, deals with the principles behind VSB and SSB signaling.

In Chapter 3, we designed and preformed large scale parameter optimisation of a DWDM RZ-OOK fibre optic communication system with VSB filtering. By using VSB filtering and the frequency allocation scheme (described within this chapter), we were able to spectrally compress $N \times 40$ Gbit/s channels and achieve a spectral efficiency of 0.64 bit/s/Hz. We simultaneously investigated both temporal and spectral domain optimisations. We demonstrated that, duty cycle optimisation leads to 1dB (GF)/3dB (SGF) improvement of system performance at 40Gbit/s with 0.64bit/s/Hz spectral efficiency. We found optimum performance of the system at a duty cycle of 0.64. We have found that signal reshaping by using a Gaussian filter at the MUX/DEMUX, performs better at VSB operations, when compared to a super Gaussian filter. We achieved a total transmission distance of 300km with $N \times 40$ Gbit/s with a spectral efficiency of 0.64 bit/s/Hz.

In Chapter 4, we introduced the CS-RZ format. We then applied it to the DWDM fibre optic communication system designed and first presented in Chapter 3, again the same frequency allocation scheme was adopted. We investigated the impact of a duty cycle on the optimisation of VSB filtering at 40 Gbit/s. We increased our optimisation parameter space by also including the effect of the ratio α/β (as well as optimising the filter bandwidth, filter detuning, duty cycle and peak power of the optical pulse) and preformed large scale numerical simulations. A feasibility of $N \times 40$ Gbit/s DWDM transmission of CS-RZ signal well over 500 km with 0.64 bit/s/Hz spectral efficiency has been confirmed by numerical modelling. We again verify that a duty cycle optimisation can further improve performance in a wavelength allocated transmission and found the optimum preform of the system to have a duty cycle of 0.64.

In Chapter 5, our final format is studied, the RZ-DPSK modulation format. We extend our investigation into highly spectral effect fibre optic transmission systems. We numerically implement the RZ-DPSK format by using the information first presented in section 2.10. Our aim is to study the performance characteristics of the format in a $N \times 40$ Gbit/s DWDM transmission system. We begin by presenting a detailed analytical analysis on measuring the performance of a RZ-DPSK signal by reconsidering the way in which the Q-factor is calculated for RZ-OOK and CS-RZ. We conclude that a new implementation for numerical

estimation of BER is required. An approach based upon the differential phase of the optical signal is adopted and its numerical implementation is presented. We apply RZ-DPSK to a DWDM system. We conduct, large scale numerical simulations and preform a multi-dimension optimisation. We demonstrate the optimum performance of RZ-DPSK at $N \times$ 40 Gbit/s DWDM (with a spectral efficiency of 0.8 bit/s/Hz), by achieving a transmission distance of over 3700km, without the use of advance optical techniques, such as PDM and FEC. It was found that ultra high density system gain performance by using super Gaussian carriers with relatively short duty cycle of 0.24 and steep super Gaussian filters to reduce inter-channel crosstalk.

Chapter 6, we move away from our investigations into DWDM fibre optic communication systems, but still concentrate on the application of RZ-DPSK modulated format and applied it to a lightwave system based upon SOA amplification. We began by speculated on the possibility of finding a quasi-soliton regime, by realising the nonlinear amplitude phase modulation produced by the action of the SOA and the dispersive nature of the optical fibre could be balanced to produce soliton-like pulses.

The region was identified by minimising the quantity I/A. Using this information we preformed numerical simulations at 40 G/bit/s with inline SOAs and demonstrated a proof of principle by achieving a transmission distance of approximately 4000km, using RZ-DPSK with a duty cycle of 0.04. We observed the system performance to be limited by the accumulation of phase noise, which resulted form the conversion of amplitude noise from ASE, dispersion induce pattern effects and nonlinear effects such as nonlinear phase noise created by SPM.

We then utilised the fact that, optimum system performance was being achieved with short pulses and decided to investigate the performance of RZ-DPSK at 80 Gbit/s with inline SOAs. We observed a near five fold increase in transmission performance by adopting RZ-DPSK in a fibre optic communication system containing SOA amplification, as opposed to RZ-OOK, by demonstrating a transmission distance of approximately 4500km.

We further extended our analysis and considered WDM transmission at 80 Gbit/s with RZ-DPSK. We found we could achieve a transmission distance of 1000km with a channel

separation of 200Ghz and 2000km with an increased separation of 300Ghz.

In Chapter 7, we persuade our interest with RZ-DPSK by investigating the regenerative properties of this format with the application of NOLMs. We first presented the basic operational principle of a NOLM. We found standard NOLM configurations were unable to successfully display 2R optical regeneration with RZ-DPSK. This is due to the fact that standard NOLM regeneration schemes display a strong conversion of the input signal's amplitude jitter into phase jitter, thus destroying the phase information encoded into the RZ-DPSK signal.

We then presented a new phase-preserving all optical 2R regeneration scheme, which utilised a novel design of NOLM based on Raman amplification in a loop and an optical attenuator. This new regenerator displayed a reduction of the phase shift variation within the power of the RA-NOLM, as opposed to the conventional NOLM. Which allowed us to investigated the regeneration properties of a single 40 Gbit/s RZ-DPSK optic fibre transmission system.

We numerically demonstrated an improvement in transmission performance, by combining the RA-NOLM and optical filtering as an in-line limiter into a RZ-DPSK system. This configuration provides simultaneous 2R regeneration and phase noise suppression. We presented results which showed that we were able to achieve a transmission distance of well over 3200km. An improvement of over 2000km was seen when compared to case of no in-line optical filtering and 700+km improvement for the system with in-line filtering.

These results indicate that regeneration of signals modulated in other phase-sensitive modulation formats such as duobinary coding or carrier-suppressed RZ are possible.

In Chapter 8, we moved onto the commercial applications of RZ-DPSK in upgrading existing 10 Gbit/s links to 40 Gbit/s. Our primary aim is to concentrate on the relative costs of the system and to exploit the inherent performance characteristics of RZ-DPSK.

We investigated the dispersion map characteristics of a RZ-DPSK transmission and preformed large scale numerical simulations. The system considered was an existing terrestrial SMF/DCF link of 838 km. We investigated the price/performance cost in associated in moving from distributed dispersion map to lumped dispersion map. We successfully demon-

strated that the performance of a $N \times 40$ Gbit/s WDM RZ-DPSK transmission system is not drastically affected by this reconfiguration. We presented results for lumped dispersion mapping with large granularity, which offers a means to a significant cost savings in point-to-point links without greatly compromising system performance. We have shown that for this particular system, it is possible to replace 5-8 existing DCMs with just one compensating module while only incurring a penalty less than 1.5 dB, thus achieving significant decrease in costs.

Appendix A

Split-Step Fourier Method

In this section we describe the numerical technique used, in studding the effects of pulse propagation in nonlinear dispersive media.

A number of numerical methods exists that are able to solve the NLSE and can be classified into two categories, (1) finite-difference methods and (2) pseudospectral methods.

Throughout the simulations in this thesis we have employed the use of the split-step Fourier method, which falls into the category as a pseudospectral method and has been proven [146] to be the most effective means of numerically solving the NLS equation (2.41). Its speed and lower memory requirements, over most finite-difference methods, are partly related to the use of the finite-Fourier-transform (FFT), which approximately, amounts up to two orders of magnitude increase in performance.

We begin from a more generalised form of the NLSE, which also includes the effect of third order dispersion [147].

$$\frac{\partial U}{\partial z} + i\frac{\beta_2}{2}\frac{\partial^2 U}{\partial t^2} - \frac{\beta_3}{6}\frac{\partial^3 U}{\partial t^3} + \frac{\alpha}{2}U = i\gamma|U|^2 U \tag{A.1}$$

In essence, the split-step Fourier method consists of treating the evolution of the optical field, over a small distance Δz along the fibre, such that the effects of dispersion and nonlinearity can be seen to act independently of each other.

We begin by rewriting (A.1) in the form of differential operators, in order to separate the linear and nonlinear parts of the equation.

$$\frac{\partial U}{\partial z} = (\hat{D}+\hat{N})U \tag{A.2}$$

Here $\hat{D}$ is the differential operator that is responsible for the dispersive effects and optical attenuation. It has the form,

$$\hat{D} = -i\frac{\beta_2}{2}\frac{\partial^2}{\partial t^2} + \frac{\beta_3}{6}\frac{\partial^3 U}{\partial t^3} - \frac{\alpha}{2} \tag{A.3}$$

$\hat{N}$ is the nonlinear operator that accounts for nonlinearities that act upon the optical pulses propagating along the fibre and consists of,

$$\hat{N} = i\gamma|U|^2 \tag{A.4}$$

Solving equation (A.2) gives the exact solution to be,

$$U(z+\Delta z,t) = \exp\left[\Delta z(\hat{D}+\hat{N})\right]U(z,t) \tag{A.5}$$

By applying the split-step Fourier method, hence, assuming the linear and nonlinear parts of the equation to act independently of each other, we can approximate the solution (A.5) to be,

$$U(z+\Delta z,t) \approx \exp(\Delta z\hat{D})\exp(\Delta z\hat{N})U(z,t) \tag{A.6}$$

This mathematically represent the action of dispersion acting in the first step and nonlinearity in the second step. Numerically the computation of the nonlinear step is relatively straight forward in the temporal domain. However, transforming to the spectral domain (by applying a Fourier transform to equation (A.3) and noting that the differential operator $\partial/\partial t$ is replaced by $i\omega$) we can drastically simplify the calculation of the linear step. The resulting equation is found to be,

$$\hat{D} = i\frac{\beta_2}{2}\omega^2 - i\frac{\beta_3}{6}\omega^3 - \frac{\alpha}{2} \tag{A.7}$$

Numerically we preform the Fourier transform by employing the use of the software library FFTW [148–150], which stands for the *"Fastest Fourier Transform in the West"*.

We can calculate the accuracy of this numerical approach by expanding the noncommuting operators $\hat{D}$ and $\hat{N}$ in equation (A.5) by using the Baker-Hausdorff formula,

$$\exp(\hat{a})\exp(\hat{b}) = \exp\left(\hat{a}+\hat{b}+\frac{1}{2}[\hat{a},\hat{b}]+\frac{1}{12}[\hat{a}-\hat{b},[\hat{a},\hat{b}]]+\ldots\right) \tag{A.8}$$

By defining $\hat{a} = \Delta z\hat{D}$ and $\hat{b} = \Delta z\hat{N}$ in the above equation we are able to expand the term $\exp[\Delta z(\hat{D}+\hat{N})]$, to give

$$\exp(\Delta z\hat{D})\exp(\Delta z\hat{N}) = \exp\left(\Delta z\hat{D}+\Delta z\hat{N}+\frac{\Delta z^2}{2}[\hat{D},\hat{N}]+\frac{\Delta z^3}{12}[\hat{D}-\hat{N},[\hat{D},\hat{N}]]+\ldots\right) \tag{A.9}$$

Here we can see that the dominate error term results from the leading commutator $\frac{\Delta z^2}{2}[\hat{D},\hat{N}]$. Hence, this implementation of the split-step Fourier method is accurate to the second order in Δz.

The accuracy of the split-step Fourier method can be improved by adopting a symmetric form of the operators in equation (A.6). By including the effect of nonlinearity in the middle of the linear step, we are able to rewrite equation (A.6),

$$U(z+\Delta z,t) \approx \exp\left(\frac{\Delta z}{2}\hat{D}\right)\exp\left(\int_z^{z+\Delta z}\hat{N}(z')dz'\right)\exp\left(\frac{\Delta z}{2}\hat{D}\right)U(z,t) \tag{A.10}$$

This form of the approximate solution is known as the symmetrised split-step Fourier method. The accuracy of this implementation can be found by applying equation (A.8) twice to equation (A.10). By doing so we find that the leading error term of the commutator in equation (A.8) is of order three.

Thus the procedure of the symmetrised split-step Fourier method is as follows, first the optical field is propagated a distance of $\Delta z/2$ with dispersion and attenuation only, in the spectral domain by using the FFTW library. At the point $z+\Delta z$, the field multiplied by the nonlinear term for the period Δz. The field then propagates the final $\Delta z/2$ with dispersion and attenuation only. This in essence lumps the nonlinearity in the midpoint of each linear step. This method results in more accurate simulations and is used extensively throughout optical communications.

Appendix B

Bit-Error Rate

In what follows is an estimation of the bit-error-rate (BER) based on Gaussian statistics.

At the receiver the sample value of the signal I is detected as a series of fluctuations about the "1" and "0" bits, I_1 and I_0 respectively. A decision level, I_D is used as to decode the relative levels into either 1 or 0. If the $I > I_D$ a one is decoded and if $I < I_D$ a zero is taken. An error in the bitpattern is defined as the cases when $I_1 < I_D$ and $I_0 > I_D$. Both types of error can be included into the BER by the following equation

$$\text{BER} - p(1)P(0/1) + p(0)P(1/0) \tag{B.1}$$

where $p(1)$ and $p(0)$ are the probability of receiving either a 1 or 0 bit. $P(0/1)$ and $P(1/0)$ are the probabilities of detecting a 0 when it should be a 1 and 1 instead of 0 respectively.

Since the probability of either 1 or 0 is equally likely, $P(1) = P(2) = \frac{1}{2}$, thus the above equation becomes,

$$BER = \frac{1}{2}[P(0/1) + P(1/0)] \tag{B.2}$$

We incorporate the noise source into the model by using Gaussian statistics. The conditional probabilities takes the following for,

$$P(0/1) = \frac{1}{\sigma\sqrt{2\pi}} \int_{-\infty}^{I_D} \exp\left(-\frac{(I-I_1)^2}{2\sigma_1^2}\right) dI = \frac{1}{2}\text{erfc}\left(\frac{I_1 - I_D}{\sigma_1\sqrt{2}}\right) \tag{B.3}$$

$$P(1/0) = \frac{1}{\sigma\sqrt{2\pi}} \int_{I_D}^{-\infty} \exp\left(-\frac{(I-I_0)^2}{2\sigma_0^2}\right) dI = \frac{1}{2}\text{erfc}\left(\frac{I_D - I_0}{\sigma_0\sqrt{2}}\right) \tag{B.4}$$

where σ_0 and σ_1 are the corresponding variances and erfc is the error function, defined as [151],

$$\text{erfc}(x) = \frac{2}{\sqrt{\pi}} \int_x^{\infty} \exp(-y^2) dy \tag{B.5}$$

We now substitute equations B.3 and B.4 into equation B.2. Thus the BER is found to be,

$$\text{BER} = \frac{1}{4}\left[\text{erfc}\left(\frac{I_1 - I_D}{\sigma_1\sqrt{2}}\right)\right] + \left[\text{erfc}\left(\frac{I_D - I_0}{\sigma_0\sqrt{2}}\right)\right] \tag{B.6}$$

From the above equation we can see the BER is dependent on the decision threshold I_D. In practise, I_D is optimised to obtain the best performance, the lowest BER. We minimise BER when I_D is chosen as

$$\frac{(I_D - I_0)^2}{2\sigma_0^2} = \frac{(I_1 - I_D)^2}{2\sigma_1^2} + \ln\left(\frac{\sigma_1}{\sigma_0}\right) \tag{B.7}$$

For most practice cases the last term in the above equation can be neglected, thus I_D takes the form,

$$\frac{(I_D - I_0)}{\sigma_0} = \frac{(I_1 - I_D)}{\sigma_1} \equiv Q \tag{B.8}$$

I_D is expressed as

$$I_D = \frac{\sigma_0 I_1 + \sigma_1 I_0}{\sigma_0 + \sigma_1} \tag{B.9}$$

Using equations B.6 and B.8 we can obtain the BER with an optimum decision setting [152],

$$\text{BER}\frac{1}{2}\left(\frac{\text{Q}}{\sqrt{2}}\right) \approx \frac{\exp(-Q^2/2)}{Q\sqrt{2}} \tag{B.10}$$

With Q factor

$$Q = \frac{I_1 - I_0}{\sigma_1 + \sigma_0} \tag{B.11}$$

Through out this thesis, we use equation B.11 to numerically calculate the Q factor for both RZ-OOK and CS-RZ modulation formats.

Publications

1. R. Bhamber, S. K. Turitsyn, V. Mezentsev, "Carrier reshaping and MUX-DEMUX filtering in 0.8 bit/s/Hz WDM RZ-DPSK transmission", in *Photon06, University of Manchester*, p1.18.

2. S. Boscolo, R. Bhamber, S. K. Turitsyn, V. K. Mezentsev and V S Grigoryan, "RZ-DPSK transmission at 80 Gbit/s channel rate using in-line semiconductor optical amplifiers", *Optics Communications* 266 (2), pp. 656-659 (Oct 2006).

3. R. Bhamber, C. French, S. K. Turitsyn, V. Mezentsev, W. Forysiak2 and J. H. B. Nijhof, "Migration from Periodic to Lumped Dispersion Mapping in Existing SMF/DCF Links", *CLEO/Europe-IQEC Conference*, pp. CI1-2-TUE, (June 2007)

4. S. Boscolo, R. Bhamber and S. K. Turitsyn, "Design of Raman-based nonlinear loop mirror for all-optical 2R regeneration of differential phase-shift-keying transmission", *IEEE Journal of Quantum Electronics* 42 (7), pp. 619-624 (Jul 2006).

5. S. Boscolo, R. Bhamber, V. K. Mezentsev, S. K. Turitsyn and V. S. Grigoryan, "RZ-DPSK transmission at 80 Gbit/s channel rate using in-line semiconductor optical amplifiers", *in Proceeding . of 8th International Conference on Transparent Optical Networks (ICTON 2006)*, Nottingham, United Kingdom, pp. Mo.P.14 (Jun 2006).

6. S. Boscolo, R. Bhamber and S. K. Turitsyn, "Design of Raman-based NOLM for optical 2R regeneration of RZ-DPSK transmission", *Tech. Dig. of Optical Fiber Communication Conference (OFC 2006)*, Anaheim, California, USA, pp. OWJ5 (Mar 2006).

7. S. Boscolo, S. K. Turitsyn, R. Bhamber, V. K. Mezentsev and V. S. Grigoryan, "Feasibility of soliton-like DPSK transmission at 40 Gb/s with in-line semiconductor optical amplifiers", *IEEE Photonics Technology Letters*, 18 (3), pp. 490-492 (Feb 2006).

8. R. S. Bhamber, S. K. Turitsyn, V. Mezentsev, "Effect of Carrier Reshaping and Narrow MUX-DEMUX Filtering in 0.8 bit/s/Hz WDM RZ-DPSK Transmission", submitted to *Optical and Quantum Electronics*.

9. S. Boscolo, S. K. Turitsyn, R. Bhamber, V. K. Mezentsev and V. S. Grigoryan,"Soliton-like differential phase-shift keying transmission guided by in-line semiconductor optical amplifiers in 40 Gb/s systems", *Postdeadline Papers of Nonlinear Guided Waves and Their Applications (NLGW 2005)*, Dresden, Germany, pp. PDP5 (Sep 2005).

10. E. G. Turitsyna, R. Bhamber, V. K. Mezentsev, A. Gillooly, J. Mitchell and S. K. Turitsyn, "Design of FBG-based ultra-narrow asymmetric filter for transmission with 0.8 bit/s/Hz spectral efficiency without polarization multiplexing", *Optical Fiber Technology*, 11 (2), pp. 202-208 (Apr 2005).

11. E. G. Turitsyna, R. Bhamber, V. K. Mezentsev, A. Gillooly, J. Mitchell and S. K. Turitsyn, "Ultra-Narrow asymmetric filter for transmission with 0.8 bit/s/Hz spectral efficiency", *CLEO/QELS & PhAST Conference*, pp. JThE54 (2005).

12. R. S. Bhamber, S. K. Turitsyn, V. Mezentsev, "Carrier reshaping and MUX/DEMUX filtering in 0.8 bit/s/Hz WDM RZ-DPSK transmission", *Optical Networks and Technologies, OpNeTec 2004: Pisa, Italy*, in *Proceeding of Optical Networks and Technologies 2004*, pp.371.

13. R. Bhamber, V. Mezentsev, S. Turitsyn, "Correlations between optimal temporal width and spectral characteristics of an optical signal in a wavelength-paired CS-RZ transmission with high spectral efficiency", *Optics Express*, Volume. 12, Issue 17, pp. 4007-4012.

14. R. S. Bhamber and S. K. Turitsyn, "Duty cycle optimization in a wavelength allocated

WDM transmission with narrow asymmetric VSB filtering", *Optical Fiber Technology*, 10 (3), pp. 260-265 (Jul 2004).

15. R. S. Bhamber, S. K. Turitsyn and V. Mezentsev, "Optimal duty cycle and asymmetric VSB filtering in a wavelength allocated DWDM CS-RZ transmission", *Nonlinear Guided Waves and Their Applications, Toronto, Canada*, pp. MC40 (Mar 2004).

Bibliography

[1] F.P. Kapron, D.B. Keck, R.D. Maurer, "Radiation losses in glass optical waveguides", *Applied Physics Letters*, vol. 17(10), pp. 423-425, 1970.

[2] W. G. French, J. B. MacChesney, P. B. O'Connor, and G. W. Tasker, Bell Syst. Tech. J. 53, 951 (1974).

[3] L. F. Mollenauer, R. H. Stolen, and J. P. Gordon, "Experimental Observation of Picosecond Pulse Narrowing and Solitons in Optical Fibers", *Physics Review Letters*, vol. 45, pp. 1095 - 1098 (1980)

[4] A. Hasegawa and F. Tappert, "Transmission of Stationary Nonlinear Optical Physics in Dispersive Dielectric Fibers I: Anomalous Dispersion", *Applied Physics Letters*, vol. 23(3), pp. 142–144, 1973.

[5] L. F. Mollenauer, R. H. Stolen, "Soliton laser", *Optics letters*, Vol. 9, Issue 1, pp. 13 (1984).

[6] Mollenauer, L. Gordon, J. Islam, M, "Soliton propagation in long fibers with periodically compensated loss", *IEEE Journal of Quantum Electronics*, Volume: 22, Issue: 1, pp. 157- 173 1986.

[7] J. D. Kafka, T. Baer, "Fiber Raman soliton laser pumped by Nd:YAG laser", *Optics Letters*, Vol. 12, Issue 3, pp. 181 1987.

[8] M. N. Islam, L. F. Mollenauer, R. H. Stolen, J. R. Simpson, H. T. Shang, "Amplifier/compressor fiber Raman lasers", *Optics Letters*, Vol. 12, Issue 10, pp. 814, 1987.

[9] A. S. Gouveia-Neto, A. S. L. Gomes and J. R. Taylor, "Femtosecond soliton Raman generation", *IEEE J. Quantum Electron* QE-24, 332 (1988).

[10] J. R. Taylor, *Optical Solitons - Theory and Experiment*, Cambridge University Press, Cambridge, UK, 1992.

[11] E. Desurvire, *Erbium-Doped Fiber Amplifiers*, Wiley, New York, 1994.

[12] G. Keiser, *Optical Fiber Communications*, Third edition, McGraw-Hill New York 2000.

[13] R. Ramaswami and K. Sivarajan, *Optical Networks*, Morgan Kaufmann, Burlington, MA, 1998.

[14] D. Taverner, N. G. R. Broderick, D. J. Richardson, R. I. Laming, M. Ibsen, "Nonlinear self-switching and multiple gap-soliton formation in a fiber Bragg grating", *Optics Letters*, Vol. 23, Issue 5, pp. 328-330, 1998.

[15] W.J. Wadsworth, J.C. Knight, A. Ortigosa-Blanch, J. Arriaga, E. Silvestre, and P.St.J. Russell, "Soliton effects in photonic crystal fibres at 850 nm", *Electronics Letters*, Volume 36, Issue 1, p. 53-55, 2000.

[16] Bigo, S, "Multiterabit/s DWDM terrestrial transmission with bandwidth-limiting optical filtering", *IEEE Journal of Selected Topics in Quantum Electronics* Volume 10, Issue, 2, pages, 329-340 2004.

[17] P. J. Winzer, "Optical transmitters, receivers and noise", in *Wiley Encylopedia of Telecommunications*, J. G. Proakis, Ed. New York, Wiley, pp. 1824-1840.

[18] A. Hirano and Y. Miyamoto, "Novel modulation formats in ultra-highspeed optical transmission systems and thier applications", in *Proceedings Optical Fibre Communication Conference*, OFC 2004.

[19] J. Conradi, "Bandwidth efficient modulation formats for digital fibre transmission systems", in *Optical Fiber Telecommunications IV B, I. Kaminow and T. Li, Eds.*, New York: Academic, 2002, pp. 862-901.

[20] A. H. Gnauck, "Advanced amplitude and phase coded formats for 40-Gb/s fibre transmission", in *Proceedings of IEEE/LEOS Annual Meeting, 2004*, paper WR1.

[21] S. Bigo, G. Charlet and e. Corbel, "What has hybrid Phase/Intensity encoding brough to 40 Gbit/s ultralong-haul systems", in *Proceedings of European Conference Optical Communication (ECOC 2004)*, Paper Th2.5.1.

[22] P. J. Winzer and R. J. Essiambre, "Advanced optical modulation formats", in *Proceedings European Conference Optical Communication (ECOC 2003)*, Paper Th2.6.1.

[23] S. Tsukamoto, D. S. Ly-Gagnon, K. Katoh and K. Kikuchi, "Coherent demodulation of 40-Gbit/s polarization-multiplexed QPSK signals with 16 GHz spacing after 200-km transmission", in *Optical Fiber Communication Conference (Optical Society of America, USA, (OFC 2005)*, Paper PDP29.

[24] P. J. Winzer, R. J. Essiambre and S. Chandrasekhar, "Dispersion-tolerant optical communication systems", in *Proceedings of European Conference Optical Communication (ECOC 2004)*, Paper We2.4.1.

[25] M. Ohm, J. Speidel, "Quaternary optical ASK-DPSK and receivers with direct detection", *IEEE Photonic Technology Letters*, volume 15, number 1, Pages 159-161, 2003.

[26] R. A. Griffin, R. I. Johnstone, R. G. Walkre, J. Hall, S. D. Wadsworth, K. Berry, A. C. Carter, M. J. Wale, J. Hughes, P. A. Jerram and N. J. Parsons, "10 Gb/s optical differential quadrature phase shift key (DQPSPK) transmission using GaAs/AlGaAs integration", in *Proceedings of Optical Fiber Communication Conference (Optical Society of America, USA, (OFC 2002)*, Paper FD6.

[27] Y. Miyamoto, A. Hirano, K. Yonenaga, A. Sano, H Toba, K. Murata and O. Mitomi, "320 Gbit/s (8 40 Gbit/s) WDM transmission over 367 km with 120 km repeater spacing using carrier-suppressed return-to-zero format", *Electronics Letters*, Volume 35, Issue 23, p. 2041-2042, 1999.

[28] A. Hirano, Y. Miyamoto, K. Yonenaga, A. Sano, and H. Toba, "40 Gbit/s L-band transmission experiment using SPM-tolerant carrier-suppressed RZ format", *Electronics Letters*, Volume 35, Issue 25, p. 2213-2215, 1999.

[29] I. S. Grant and W. R. Phillips, *Electromagnetism*. Wiley 2^{nd} edition 1998, Chapter 2.

[30] I. S. Grant and W. R. Phillips, *Electromagnetism*. Wiley 2^{nd} edition 1998, Chapter 5.

[31] R. W. Boyd, *Nonlinear Optics*. Academic Press 2^{nd} edition 2003, Chapter 1.

[32] A. Yariv, *Quantum Electronics*. John Wily and Sons 3^{nd} edition.

[33] Y. R. Shen, *The Principles of Nonlinear Optics*. John Wily and Sons 1984, Chapter 2.

[34] R. W. Boyd, *Nonlinear Optics*. Academic Press 2^{nd} edition 2003, Chapter 3.

[35] C. A. Burrus and R. W. Dawson, "Small-Area High-Current-Density GaAs Electroluminescent Diodes aND a method of Operation for Improved Degradation Characteristics", *Applied Physics Letters*, Volume 17, Issue 3, pp. 97-99, 1970.

[36] H. Ishikawa, H. Soda, K. Wakao, K. Kihara, K. Kamite, Y. Kotaki, M. Matsuda, H. Sudo, S. Yamakoshi, S. Isozumi and H. Imai, "Distributed feedback laser emitting at 1.3 μm for gigabit communication systems", *Journal of lightwave technology*, , volume 5, issue 6, pp. 848-855, 1987

[37] P.A. Morton, T. Tanbun-Ek, R.A. Logan, N. Chand, K.W. Wecht, A.M. Sergent, and P.F. Sciortino, Jr, "Packaged 1.55 m DFB laser with 25 GHz modulation bandwidth", *Electronics Letters*, Volume 30, Issue 24, p. 2044-2046, 1994.

[38] E. Goutain, J.C. Renaud, M. Krakowski, D. Rondi, R. Blondeau, and D. Decoster,, "30 GHz bandwidth, 1.55 m MQW-DFB laser diode based on a new modulation scheme", *Electronics Letters*, Volume 32, Issue 10, p. 896-897, year 1996.

[39] S. Lindgren, H. Ahlfeldt, L Backlin, L. Forssen, C. Vieider, H. Elderstig, M. Svensson, L. Granlund et. al "24-GHz Modulation Bandwidth and Passive Alignment of Flip-

Chip Mounted DFB Laser Diodes", *IEEE Photonics Technology Letters*, volume 9, pp. 306-308, 1997.

[40] R.A. Linke, "Transient chirping in single-frequency lasers: lightwave systems consequences", *Electronics Letters*, Volume 20, Issue 11, p. 472-474, 1984.

[41] Govind P. Agrawal, M. J. Potasek, "Effect of frequency chirping on the performance of optical communication systems", *Optics Letters*, Vol. 11, Issue 5, pp. 318, May 1986.

[42] Linke, R., "Modulation induced transient chirping in single frequency lasers", *IEEE Journal of Quantum Electronics*, Volume: 21, Issue: 6, pp. 593-597, 1985.

[43] G. P. Agrawal *Nonlinear Fiber optics*, Third Edition, Academic Press, chapter 3.

[44] E. Iannone, F. Matera, A. Mecozzi, M. Settembre, *Nonlinear Optical Communication Networks*, Wiley Series in Microwave and Optical Engineering. Chapter 2, 1998.

[45] G. P. Agrawal, *Nonlinear Fiber Optics*. Academic Press 3^{nd} edition 2001, San Diego.

[46] E. Iannone, F. Matera, A. Mecozzi, M. Settembre, *Nonlinear Optical Communication Networks*, Wiley Series in Microwave and Optical Engineering. Chapter 2, 1998.

[47] Akira Hasegawa and Yuji Kodama, *Solitons in Optical Communications*

[48] E. Innone, F. Matera, A. Mecozzi and M. Settembre, *Nonlinear Optical Communication Networks*

[49] H P. Yuen, V. W. S. Chan, "Noise in homodyne and heterodyne detection", *Optics Letters*, volume 8, number 3, March 1983.

[50] Hans-A. Bachor, T. C. Ralph, *A Guide to Experiments in Quantum Optics*, Wiley-VCH; Second. Revised and Enlarged Edition, Chapter 8, (April 9, 2004).

[51] M. O. Scully, M. S. Zubairy, *Quantum Optics*, Cambridge University Press, Chapter 4, (September 28, 1997).

[52] Keang-Po Ho, *Phase-Modulated Optical Communication Systems*, Springer; First edition, Chapter 2 (July 1, 2005).

[53] S. Bigo and Y. Frignac, "Multi-terabit/s WDM transmissions at 40GGbit/s channel rate" in *Proceedings of European Conference on Optical Communication*, paper PD-1.2. (ECOC2000)

[54] S. Bigo: "Improving spectral efficiency by ultra-narrow optical filtering to achieve multi-terabit/s capacities",in *Optical Fiber Communication Conference (Optical Society of America, Washington, D.C., USA, 2002)* paper WX3 (OFC 2002).

[55] W. Idler, S. Bigo, Y. Frignac, B. Franz, G. Veith: "Vestigial Side Band Demultiplexing for Ultra High Capacity (0.64 bits/s/Hz) Transmission of 128x40 Gb/s Channels",in *Optical Fiber Communication Conference (Optical Society of America, Washington, D.C., USA, 2001)*, paper MM3, (OFC 2001).

[56] S. Bigo, Y. Fringnac, G. Charlet. W. Idler et al: "10.2Tbit/s (256x42.7Gbit/s PDM/WDM) transmission over 100km TeralightTM fiber with 1.28bit/s/Hz spectral efficiency", in *Optical Fiber Communication Conference (Optical Society of America, Washington, D.C., 2001)*, paper PD-25, (OFC 2001).

[57] A. Hirano and Y. Miyamoto, "A novel dispersion compensation scheme based on phase comparison between two SSB signals generated from a spectrally filtered CS-RZ signal" in *Optical Fiber Communication Conference (Optical Society of America, Washington, D.C., USA, 2002)* paper WE2 (OFC 2002)

[58] I. Morita and N. Edagawa, "Study on optimum OTDM signals for long-distance 40 Gbit/s transmission" in *Optical Fiber Communication Conference, (Optical Society of America, Washington, D.C., 2002)* paper TuA4 (OFC 2002).

[59] T. Tsuritani, Morita, A. Agata, N. Edagawa, "Study on Optimum Optical Pre-Filtering Condition for Highly Spectral-Efficient Ultralong-Haul Transmission Using 40Gbit/s CS-RZ Signal and All-Raman Repeaters" in *Optical Fiber Communication Conference (Optical Society of America, Washington, D.C., 2003)* paper FE4, (OFC2003).

[60] I. Morita, K. Imai, N. Edagawa, T. Tsuritani, N. Yoshikane, A. Agata, "100% spectral-efficient 25 x 42.7 Gbit/s transmission using asymmetrically filtered CS-RZ signal and a novel crosstalk suppressor" in *Proceedings of European Conference on Optical Communication (ECOC 2002, Copenhagen, Denmark)*, paper PD4-7.

[61] A. Agata et al, I. Morita, T. Tsuritani, N. Edagawa, "Characteristics of Asymmetrically Filtered 40Gbit/s CS-RZ Signals", in *Optical Fiber Communication Conference (Optical Society of America, Washington, D.C., 2003)* paper MF78 (OFC 2003).

[62] A. Agata, T. Tsuritani, I. Morita, and N. Edagawa, "'Over 1000 km DWDM transmission with supercontinuum multi-carrier source", *Electronics Letters*, Volume 39, Issue 14, p. 1078-1079

[63] P. S. Henry, "Error-rate performance of optical amplifiers", in *Proceedings of Optical Fiber Communication Conference (Optical Society of America), 1989*, Paper THK3, (1989).

[64] P. A. Humblet and M. Azizoglu, "On the bit error rate of lightwave systems with optical amplifiers", *IEEE Journal of Lightwave Technology*, Vol. 9, pp 1576-1582 1991.

[65] S.R. Chinn, D.M. Boroson, J.C. Livas, "Sensitivity of optically preamplified DPSK receivers withFabry-Perot filters", *IEEE Journal of Lightwave Technology*, Vol. 14, Issue 3, pp 370-376, 1996.

[66] W. A. Atia and R. S. Bondurant,*Proceedings of LEOS* 12^{th} *Annual Meeting*, Vol. 1, pp.226-227,1999

[67] A. H. Gnauck, et al., accepted to IEEE Photonic Tech. Letters

[68] T. Miyano, M. Fukutoku, K. Hattori and H. One, "Suppression of degradation induced by SPM/XPM + GVD in WDM transmission using a bit-synchronous intensity modulated DPSK signal" in *OECC 2000*, pp. 14D3-14D3 (2000).

[69] M. Hanna, H. Porte, J. P. Goedgebuer and W. T. Rhodes, "Experimental investigation of soliton optical phase jitter", *IEEE Quantum Electronics*, vol. 36, pp. 1333-1338, 2000.

[70] A. h. Gnauck, "40-Gb/s RZ-differential phase shift keyed transmission", in *Optical Fiber Communication Conference (Optical Society of America), Atlanta* paper GA (2003)

[71] M. Rohde, C. Caspar, N. Heimes, M. Konitzer, E. J. Bachus and N. Hanik, "Robustness of DPSK direct detection transmission format in standard fiber WDM systems", *Electronic Letters*, vol. 36, pp. 1483-1484 2000.

[72] J. K. Rhee, D. Chowdhury, K. S. Cheng and U Gliese, "DPSK 32 × 10 Gb/s transmission modeling on 5×90 km terrestrial system", *IEEE Photonic Technology Letters*, vol. 12, pp. 1627-1629, 2000.

[73] J. Leibrich, C. Wree and W. Rosenkranz, "CF-RZ-DPSK for suppression of XPM on dispersion-managed long-haul optical WDM transmission on standard single-mode fiber", *IEEE Photonic Technology Letters*, vol. 14, pp. 155-157 2002.

[74] A. H. Gnauck, G. Raybon, S. Chandrasekhar, J. Leuthold, C. Doerr, L. Stul, A. Agarwal, S. Banerjee, D. Grosz, S. Hunsche, A. Kung, A. Marhelyuk, D. Maywar, M. Movassaghi, X. Liu, C. Xu, X. Wei and D. M. Gill, "2.5 Tb/s (64×42.7 Gb/s) transmission over 40×100km NZDSF using RZ-DPSK format all-Raman-amplified spans" in *Optical Fiber Communication Conference (Optical Society of America) 2002*, postdeadline paper FC-2.

[75] C. Rasnussen, T. Fjelde, J. Bennike, F. Liu, B. Dey, P. Mikkelsen, P. Mamyshev and P. Serbe, "DWDM 40G transmission overtrans-Pacific distance (10000km) using CSRZ-DPSK, enhanced FEC and all Raman amplified 100 km ultrawave fibre spans" in *Optical Fiber Communication Conference (Optical Society of America) 2003*, 2003.

[76] B. Zhu, L. Nelson, L. Stulz, A. Gnauck, C. Doerr, J. Leuthold, L. Gruner Nielsen, M. Pedersen, J. Kim and R. Lingle, "6.4 Tb/s (160 × 42.7 Gb/s) transmission with 0.8

bits/s/Hz spectral effciency over 32 × 100km of fiber using CSRZ-DPSK format", in *Optical Fiber Communication Conference (Optical Society of America), Atlanta GA* 2003.

[77] C. Wree, N. Hecker-Denschlag, E. Gottwald, p. Krummrich, j. leibrich, E. D. Schmidt, B. Lankl and W. Rosenkranz, "High spectral efficiency 1.6 b/s/Hz transmission (8 × 40Gb/s with 25GHz grid) over 200km SSMF using RZ-DQPSK and polarization multiplexing", *IEEE Photonic Technology Letters*, vol. 15, pp. 1303-1305, 2003.

[78] T. Chikama, S. Watanabe, T. Naito, H. Onaka, T. Kiyonaga, Y. Onoda, H. Mityata, M. Suyama, M. Seino and H. Kuwahara, "Modulation and demodulation techneques in optical heterodyne PSK transmission systems", *Journal of Lightwave Technology*, vol. 8, pp.309-322, March 1990.

[79] R. A. Linke and A. H. Gnauck, "High-capacity coherent lightwave systems", *Journal of Lightwave Technology*, vol. 6, pp. 1750-1769, November 1988.

[80] E. A. Swanson, J. C. Livas and R. S. Bondurant, "High sensitivity optically preamplified direct detection DPSK receiver with active delayline stabilization", *IEEE Photonic Technology Letter*, vol. 6, pp. 263-265, February 1994.

[81] R. S. Vodhanel, A. F. Elrefaie, M. Z. Iqbal, R. E. Wagner, J. L. Gimlett and S. Tsuji, "Preformance of directly modulated DFB lasers in 10-Gb/s ASk, FSK and DPSK lightwave systems", *Journal of Lightwave Technology*, vol. 8, pp. 1379-1385, September 1990.

[82] G. Jacobsen, "Performance of DPSK and CPFSK systems with significant post-detection filtering", *Journal of Lightwave Technology*, vol. 11, pp. 1622-1631. October 1993.

[83] P. A. Humblet and M. Azizoglu, "On the bit error rate of lightwave systems with optical amplifiers", *Journal of Lightwave Technology*, vol. 9, pp. 1576-1582, November 1991.

[84] W. A. Atia and R. S. Bondurant, "Demonstration of return-to-zero signaling in both OOK and DPSK formats to improve receiver sensitivity in an optically preamplified receiver", in *Proceedings of LEOS 1999*, paper TuM3 (1999).

[85] S. R. Chinn, D. M. Boroson and J. C. Livas, "Sensitivity of optically preamplified DPSK receivers with Fabry-Perot filters", *Journal of Lightwave Technology*, vol. 14, pp. 370-376, March 1996.

[86] X. Wei, X. Liu and C. Xu, "*Q* factor in numerical simulations of DPSK with optical delay demodulation", [Online Publication]. *http://arXiv.org/abs/physics/0304002*.

[87] N.S. Bergano, F.W. Kerfoot, C.R. Davidsion, "Margin measurements in optical amplifier system", *IEEE Photonics Technology Letters*, Volume: 5, Issue: 3, page(s): 304-306, Mar 1993

[88] C. Xu, Xiang Liu, Xing Wei, "Differential phase-shift keying for high spectral efficiency optical transmissions", *IEEE Journal of Selected Topics in Quantum Electronics*, Volume: 10, Issue: 2, page(s): 281- 293, March-April 2004.

[89] C.C. Hiew, F.M. Abbou, H.T. Chuah, S.P. Majumder, A.A.R. Hairul, "BER estimation of optical WDM RZ-DPSK systems through the differential phase Q", *IEEE Photonics Technology Letters*, Volume: 16, Issue: 12, page(s): 2619- 2621, Dec. 2004.

[90] J.-X. Cai et al., "RZ-DPSK Field Trial over 13,100 km of Installed Non Slope-Matched Submarine Fibers"*Optical Fiber Communication Conference (Optical Society of America) 2004*, paper PD34 (2004).

[91] A. H. Gnauck et al., "6 x 42.7-Gb/s transmission over ten 200-km EDFA-amplified SSMF spans using polarization-alternating RZ-DPSK", *Optical Fiber Communication Conference (Optical Society of America) 2004*, paper PD35 (2004).

[92] B. Zhu, "Ultra high density and long haul transmissions", *Optical Fiber Communication Conference (Optical Society of America) 2004*, paper ThE1 (2004).

[93] A. H. Gnauck, G. Raybon, S. Chandrasekhar, J. Leuthold, C. Doerr, L. Stulz and E. Burrows, "25 × 40-Gb/s copolarized DPSK transmission over 12 × 100 km NZDF with 50 GHz" *IEEE Photonic Technology Letters*, vol. 15, pp. 467-469.

[94] L. Becouarn, G. Vareille, P. Pecci and J. F. Marcercou, "3 Tbit/s transmission (301 DPSK channels at 10.709 Gb/s) over 10270km with a record efficiency of 0.65 (Bit/s)/Hz", in *ECOC2003 Rimini, Italy 2003.*

[95] I. Morita and N. Edagawa, "50 GHz-spaced 64 × 42.7 Gbit/s transmission over 8200km using pre-filtered CS-RZ DPSK signal and EDFA repeaters", *presented in ECOC2003 Rimini, Italy 2003.*

[96] B. Zhu, L. Nelson, L. Stulz, A. Gnauck, C. Doerr, J. Leuthold, L. Gruner Nielsen, M. Pedersen, J. Kim and R. Lingle, "6.4 Tb/s (160 × 42.7 Gb/s) transmission with 0.8 bits/s/Hz spectral effciency over 32 × 100km of fiber using CSRZ-DPSK format", in *Optical Fiber Communication Conference (Optical Society of America), Atlanta GA* 2003.

[97] C. Wree, N. Hecker-Denschlag, E. Gottwald, p. Krummrich, j. leibrich, E. D. Schmidt, B. Lankl and W. Rosenkranz, "High spectral efficiency 1.6 b/s/Hz transmission (8 × 40Gb/s with 25GHz grid) over 200km SSMF using RZ-DQPSK and polarization multiplexing", *IEEE Photonic Technology Letters*, vol. 15, pp. 1303-1305, 2003.

[98] A. Agata et al., "Characteristics of Asymmetrically Filtered 40Gbit/s CS-RZ Signals", *Optical Fiber Communication Conference (Optical Society of America) 2003*, paper MF78 (2003).

[99] K. Tanaka, I.Morita, and N.Edagawa, "Study on Optimum Pre-Filtering Condition for 42.7 Gbit/s CS-RZ DPSK Signal", *Optical Fiber Communication Conference (Optical Society of America) 2004*, paper TuF2 (2004)

[100] I. Morita and N. Edagawa, "50GHz-spaced 64 x 42.7Gbit/s Transmission Over 8200km Using Pre-filtered CS-RZ DPSK Signal and EDFA Repeaters", *ECOC2003*, PD (2003)

[101] G. P. Agrawal and N. A. Olsson, "Self-phase modulation and spectral broadening of optical pulses in semiconductor laser amplifiers",*IEEE Journal of Quantum Electron*, 25, pp. 2297 (1989)

[102] G. Onishchukov, V. Lokhnygin, A. Shipulin, and M. Gölles, "Differential binary phase-shift keying transmission using cascaded semiconductor optical amplifiers," in *Proc. CLEO/Pacific Rim. Conf.*, vol. 2, Seoul, South Corea, 1999, pp. 513–514.

[103] P. S. Cho and J. B. Khurgin, "Suppression of cross-gain modulation in SOA using RZ-DPSK modulation format," *IEEE Photon. Technol. Lett.*, vol. 15, pp. 162–164, 2003.

[104] X. Wei, Y. Su, J. Leuthold, and S. Chandrasekhar, "10-Gb/s RZ-DPSK transmitter using a saturated SOA as a power booster and limitng amplifier," *IEEE Photon. Technol. Lett.*, vol. 16, pp. 1582–1584, 2004.

[105] V. S. Grigoryan, "Autosoliton in a fiber with distributed saturable amplifiers," *Opt. Lett.*, vol. 21, pp. 1882–1884, 1996.

[106] G. P. Agrawal and N. A. Olsson, "Self-phase modulation and spectral broadening of optical pulses in semiconductor laser amplifiers," *IEEE J. Quantum Electron.*, vol. 25, pp. 2297–2306, 1989.

[107] C. Xu, X. Liu, and X. Wei, "Differential phase-shift keying for high spectral efficiency optical transmissions," *IEEE J. Selected Topics Quantum Electron.*, vol. 10, pp. 281–293, 2004.

[108] J. P. Gordon and L. F. Mollenauer, "Phase noise in photonic communication systems using linear amplifiers," *Opt. Lett.*, vol. 15, pp. 1351–1353, 1990.

[109] K. P. Ho, "Impact of nonlinear phase noise to DPSK signals: A comparison of different models," *IEEE Photon. Technol. Lett.*, vol. 16, pp. 1403–1405, 2004.

[110] X. Wei and L. Zhang, "Analysis of the phase noise in saturated SOAs for DPSK applications," *IEEE J. Quantum Electron.*, vol. 41, pp. 554–561, 2005.

[111] S. Xu, J. B. Khurgin, I. Vurgaftman, J. R. Meyer, "Reducing crosstalk and signal distortion in wavelength-division multiplexing by increasing carrier lifetimes in semiconductor optical amplifiers", *Journal of Lightwave Technology*,Volume 21, Issue 6, Pages 1474-1485, 2003.

[112] A. Bhardwaj, C. R. Doerr, S. Chandrasekhar and L. W. Stulz, "Reduction of nonlinear distortion from a semiconductor optical amplifier using an optical equalizer", *IEEE Photonics Technology Letters*, Volume 16, Issue 3, pages 921-9232004.

[113] S. Xu, J. B. Khurgin, "A dispersion management scheme for reducing SOA-induced crosstalk in WDM links", *Journal of Lightwave Technology*, Volume 22, Issue 2, On pages 417-422, 2004.

[114] G. Onishchukov, V. Lokhnygin, A. Shipulin, M. Gölles, in *Proceedings CLEO/Pacific Rim. Conf.*, Seoul, South Corea, 2 (1999) 513.

[115] P. S. Cho, J. B. Khurgin, "Suppression of cross-gain modulation in SOA using RZ-DPSK modulation format" *IEEE Photonics Technology Letters*, Volume 15, Issue 1, pages 162-164, 2003.

[116] X. Wei, Y. Su, X. Liu, J. Leuthold, S. Chandrasekhar, "10-Gb/s RZ-DPSK transmitter using a saturated SOA as a power booster and limiting amplifier", *IEEE Photonics Technology Letters*, Volume 16, Issue 6, Pages 1582-1584, 2004.

[117] V. S. Grigoryan, "Autosoliton in a fiber with distributed saturable amplifiers", *Optics Letters*, Vol. 21, Issue 23, pp. 1882, 1996.

[118] J .P. Gordon, L.F. Mollenauer, "Phase noise in photonic communications systems using linear amplifiers", *Optics Letters*, Vol. 15, Issue 23, pp. 1351, 1990.

[119] K.-P. Ho, "Impact of nonlinear phase noise to DPSK signals: a comparison of different models", *IEEE Photonics Technology Letters*, Volume 16, Issue 5, pages 1403-1405, 2004.

[120] S. Boscolo, S. K. Turitsyn, R. Bhamber, V. K. Mezentsev, V. S. Grigoryan, "", *IEEE Photonics Technology Letters*, Volume 18, Issue 3, Pages 490-492, 2006.

[121] G. P. Agrawal, N. A. Olsson, "Self-phase modulation and spectral broadening of optical pulses in semiconductor laser amplifiers", *IEEE Journal of Quantum Electronics*, Volume 25, Issue 11, pages 2297-2306, 1989.

[122] C. Xu, X. Liu, X. Wei, "Differential phase-shift keying for high spectral efficiency optical transmissions", *IEEE Journal of Selected Topics in Quantum Electronics*, Volume 10, Issue 2, pages 281-293, 2004.

[123] P. J. Winzer and R. -J. Essiambre, "Advanced optical modulation formats," in *Proc. ECOC 2003*, Rimini, Italy, 2003, Paper Th2.6.1, pp. 1002–1003.

[124] A. H. Gnauck and P. J. Winzer, "Optical phase-shift-keyed transmission," *IEEE J. Lightwave Technol.*, vol. 23, no. 1, pp. 115–130, 2005.

[125] G. P. Agrawal *Nonlinear Fiber optics*, Third Edition, Academic Press, chapter 2.

[126] G. P. Agrawal *Lightwave Technology: Components and Devices*, Wiley-Interscience, chapter 2.

[127] J. P. Gordon and L. F. Mollenauer, "Phase noise in photonic communication systems using linear amplifiers," *Opt. Lett.*, vol. 15, no. 23, pp. 1351–1354, 1990.

[128] H. Kim and A. H. Gnauck, "Experimental investigation of the performance limitation of DPSK systems due to nonlinear phase noise," *IEEE Photon. Technol. Lett.*, vol. 15, no. 2, pp. 320–322, 2003.

[129] P. S. Devgan, M. Shin, V. S. Grigoryan, J. Lasri, and P. Kumar, "SOA-based regenerative amplification of phase noise degraded DPSK signals," in *Postdeadline Papers OFC 2005*, Anaheim, California, 2005, Paper PDP34.

[130] M. E. Marhic, C. H. Hsia, and J. M. Jeong, "Optical amplification in a nonlinear fiber interferometer," *Electron. Lett.*, vol. 27, pp. 210–211, 1991.

[131] A. Takada and W. Imajuku, "Amplitude noise suppression using a high gain phase sensitive amplifier as a limiting amplifier," *Electron. Lett.*, vol. 32, pp. 677–679, 1996.

[132] K. Croussore, C. Kim, and G. Li, "All-optical regeneration of differential phase-shift keying signals based on phase-sensitive amplification," *Opt. Lett.*, vol. 29, no. 20, pp. 2357–2359, 2004.

[133] A. G. Striegler and B. Schmauss, "All-optical DPSK signal regeneration based on cross-phase modulation," *IEEE Photon. Technol. Lett.*, vol. 16, no. 4, pp. 1083–1085, 2004.

[134] A. G. Striegler, M. Meissner, K. Cveček, K. Sponsel, G. Leuchs, and B. Schmauss, "NOLM-based RZ-DPSK signal regeneration," *IEEE Photon. Technol. Lett.*, vol. 17, no. 3, pp. 639–641, 2005.

[135] M. Matsumoto, "Regeneration of RZ-DPSK signals by fiber-based all-optical regenerators," *IEEE Photon. Technol. Lett.*, vol. 17, no. 5, pp. 1055–1057, 2005.

[136] N. J. Doran and D. Wood, "Picosecond soliton transmission using concatenated nonlinear optical loop-mirror intensity filters," *J. Opt. Soc. Amer. B*, vol. 12, no. 6, pp. 1117–1125, 1995.

[137] S. Boscolo, J. H. B. Nijhof, and S. K. Turitsyn, "Autosoliton transmission in dispersion-managed systems guided by in-line nonlinear optical loop mirrors," *Opt. Lett.*, vol. 25, no. 17, pp. 1240–1242, 2000.

[138] S. Boscolo, S. K. Turitsyn, and K. J. Blow, "Study of the operating regime for all-optical passive 2R regeneration of dispersion-managed RZ data at 40 Gb/s using in-line NOLMs," *IEEE Photon. Technol. Lett.*, vol. 14, no. 1, pp. 30–32, 2002.

[139] F. Seguineau, B. Lavigne, D. Rouvillain, P. Brindel, L. Pierre, and O. Leclerc, "Experimental demonstration of simple NOLM-based 2R regenerator for 42.66 Gbit/s WDM long-haul transmissions," in *Proc. OFC 2004*, Los Angeles, CA, 2004, Paper WN4.

[140] C. Xu, X. Liu, and X. Wei, "Differential phase-shift keying for high spectral efficiency optical transmissions," *IEEE J. Selected Topics Quantum Electron.*, vol. 10, no. 2, pp. 281–293, 2004.

[141] N. J. Smith and N. J. Doran, "Picosecond soliton transmission using concatenated nonlinear optical loop-mirror intensity filters", *Journal of the Optical Society of America B*, volume 12, number 6, June 1995.

[142] J. H. B. Nijhof and W. Forysiak, "Investigation of optimal dispersion management for terrestrial 40Gbit/s RZ-DQPSK transmission systems", in *CLEO Proceedings paper CThE* (2006).

[143] C. Xu, X. Liu, X. Wei,"Differential phase-shift keying for high spectral efficiency optical transmissions", *IEEE J. Selected Topics Quantum Electron.* 10 (2004) 281.

[144] E. G. Shapiro, M.P. Fedoruk, S.K. Turitsyn, "Direct modelling of error statistics at 40 Gbit/s rate in SMF/DCF link with strong bit overlapping", *Electron. Letters,* 40(22), 1436 - 1437, 2004.

[145] D. van den Borne, S. L. Jansen, et al. "Lumped Dispersion Management in Long-Haul 42.8-Gbit/s RZ-DQPSK Transmission", in *ECOC Proceedings paper Mo3.2.2* (2006).

[146] T. R. Taha and M. J. Ablowitz, "Analytical and numerical aspects of certain nonlinear evolution equations, II. Numerical, nonlinear Schrdinger equation", *Journal of Computonal Physics*, 55, 203, (1984).

[147] G. P. Agrawal, *Nonlinear Fiber Optics*. Academic Press 3^{nd} edition 2001, San Diego, chapter 2.

[148] Matteo Frigo and Steven G. Johnson, "The Design and Implementation of FFTW3", *Proceedings of the IEEE*, **93** (2), 216-231 (2005).

[149] Matteo Frigo, "A Fast Fourier Transform Compiler", *in the Proceedings of the 1999 ACM SIGPLAN Conference on Programming Language Design and Implementation*, Atlanta, Georgia, May 1999, (PLDI '99).

[150] M. Frigo and S. G. Johnson, *The Fastest Fourier Transform in the West*, MIT-LCS-TR-728 (September 1997).

[151] E. Kreyszig *"Advanced Engineering Mathematics"*, John Wiley and Sons, INC. 8^th edition, chaper 11.

[152] G. P. Agrawal *"Fiber-Optic Communication System"*, Wiley Series in Microwave and Optical Engineering, third edition, chapter 11.